Double Shrouded Horizontal Axis Wind Turbine

By

Abhishek Johri

A Dissertation submitted in fulfilment of Master of Science in Mechanical Engineering

School of Engineering, University of KwaZulu-Natal

Durban

2013

Supervisor

Dr Freddie L. Inambao

EXAMINER'S COPY

As the candidate's Supervisor I agree/do not agree to the submission of this dissertation.

Signed: Dr Freddie L. Inambao

COLLEGE OF AGRICULTURE, ENGINEERING AND SCIENCE

DECLARATION 1 – PLAGIARISM

I, Abhishek Johri, declare that:

1. The research reported in this dissertation, except where otherwise indicated, is my original research.

2. This dissertation has not been submitted for any degree or examination at any other university.

3. This dissertation does not contain other persons' data, pictures, graphs or other information, unless specifically acknowledged as being sourced from other persons.

4. This dissertation does not contain other persons' writing, unless specifically acknowledged as being sourced from other researchers. Where other written sources have been quoted, then:
   a. Their words have been re-written but the general information attributed to them has been referenced; and
   b. Where their exact words have been used, then their writing has been placed in italics and inside quotation marks, and referenced.

5. This dissertation does not contain text, graphics or tables copied and pasted from the Internet, unless specifically acknowledged, and the source being detailed in the dissertation and in the References sections.

Signed

……

COLLEGE OF AGRICULTURE, ENGINEERING AND SCIENCE

DECLARATION 2 – PUBLICATIONS

DETAILS OF CONTRIBUTION TO PUBLICATIONS

Publication 1: Abhishek Johri and Freddie L. Inambao, "CFD Simulation for Double Shroud with Flanged End" (submitted).

Publication 2: Abhishek Johri and Freddie L. Inambao, "FEA Simulation for Double Shroud with Flanged End" (to be submitted).

In these publications, I, Abhishek Johri was the main and corresponding author, whilst Dr Freddie L. Inambao was the co-author and my research supervisor.

Signed

……..

ACKNOWLEDGEMENTS

I acknowledge my supervisor, Dr Freddie L. Inambao for all of his guidance with regards to the degree and the inspiration received from his high expectations of me. I also acknowledge my Mother and Father for their support and patience with me in regard to my absence due to the dedication required for this degree.

Special thanks to my brother-in-law Mr Narainsamy Govender and my sister Mrs Shubhra Govender for showing deep faith and support. I acknowledge the assistance of the staff of the Discipline of Mechanical Engineering Mrs Omma Chety, Mr Shaun Savy, Mrs Kogie Naicker and Mr Mike Pillay. I acknowledge the help of my fellow postgraduate students Seffat Chowdhary, Riyal Sandeep Oudhram, Vincnet Van Erk and Calvin Cunniffe.

Finally, but not least, I acknowledge and thank the Creator of the world, to whom this dissertation is dedicated, for empowering, strengthening and moulding my way to its successful completion.

Abhishek Johri

ABSTRACT

This research study deals with the design and optimization of a Shrouded Horizontal Axis Wind Turbine which is an emerging system in the field of renewable energy resources. The literature review shows that several authors have studied single shrouded horizontal axis wind turbines and many applications are in existence, but no development has been done in the field of double shrouded horizontal axis wind turbines.

South Africa's surging growth in electricity consumption requires development of this kind of wind turbine which can be implemented at both domestic and commercial levels. This research emphasis is on the development of a second shroud overlaying the existing shroud of a wind turbine. The research focuses on the development of a double shrouded horizontal axis wind turbine using a different type of NACA airfoil for the shroud and the blade in order to optimize the results.

The objective of this research was to design and develop a shroud design with flanged ends which could operate a horizontal axis wind turbine at very low wind speeds. The effect of the double shroud on the wind speed is analyzed and optimized by simulation using different airfoil designs and profiles. The maximum wind speed increased 2.004 times at low wind speeds ranging from 2m/s to 7m/s and increased by 2.162 times for the high wind speeds ranging from 8m/s to 13m/s with the selection of an appropriate airfoil for the outer and inner shrouds. This shroud design is suitable for those areas where the wind speed is not very high due to urbanization and mega structures obstructing the wind flow hence reducing the wind speed. Also it is suitable for use in farm lands, rural areas, remote telecommunication stations etc. where it can stand alone in fulfilling energy requirements. In this study, Computational Fluid Analysis and optimization of the design were carried out using highly efficient CFD software, namely, Star CCm+. From the study we concluded that replacement of a single shroud with a double shroud provides a surge in energy efficiency of wind turbines of the same class

Contents

LIST OF FIGURES

LIST OF TABLES

NOMENCLATURE

Latin Symbols

m	Mass	[m]
A, S	Area	[m^2]
v_∞	Ambient wind velocity	[m/s]
P_∞	Ambient wind pressure	[N/m^2]
$\overset{+}{P}$	Positive pressure	[N/m^2]
F	Force quantity	[kg m/s^2]
v_2	Velocity of air after leaving the pipe	[m/s]
v_1	Velocity of air inside the pipe	[m/s]
v_{avg}	Average velocity of air	[m/s]
F_L	Lift force	[kg m/s^2]
W	Relative wind speed	[m/s]
F_D	Drag force	[kg m/s^2]
I	Angel of attack	[θ]
r	Radius	[m]

n	Rotations per second	[r/s]
Q_{out}	Volume of air out	[m^3]
Q_{in}	Volume of air in	[m^3]

Dimensionless numbers

C_L	Coefficient of lift
C_D	Coefficient of drag
C_p	Coefficient of performance

Greek Symbols

ρ	Density of air	[kg/m^3]
α	Angle of attack	[θ]
Δp	Pressure difference	[$kg/m\ s^2$]

Abbreviation and acronyms

AGL	Above Ground Level
AOA	Angle of Attack
BEM	Blade Element Momentum
CFD	Computational Fluid Dynamics
DAWT	Diffuser Augmented Wind Turbine
EMA	eThekwini Municipal Area

FEA	Finite Element Analysis
FEM	Finite Element Method
GEF	Global Environment Facility
GEF	Global Environment Fund
HAWT	Horizontal Axis Wind Turbine
IGES	Initial Graphics Exchange Specification
NACA	National Advisory Committee for Aeronautics
RANS	Reynolds Average Navier Strokes
RDE	Royal Danish Embassy
SAWEP	South Africa Wind Energy Project
TSR	Tip Speed Ratio
WASA	Wind Atlas for South Africa
VAWT	Vertical Axis Wind Turbine

1. INTRODUCTION

Energy is the basic necessity of life just like water and food. Energy exists in many different forms such as heat, kinetic, electrical, chemical etc. Energy cannot be created nor can it be destroyed but it can be changed from one form to another. A form of energy may not be useful but it can be converted and transferred into a different form where it can be useful. To convert energy from one form to another a machine or tool is needed. Since every moving particle has kinetic energy, moving or flowing wind has kinetic energy which can be transformed for use with help of wind turbines as a tool. Wind energy can be derived in the form of mechanical energy and electrical energy as required. The most efficient way of using wind energy is as electrical energy.

Due to rising pollution levels and concerns regarding changes in climate – arising mainly from energy-producing processes – there is increased demand for the reduction of environmentally damaging emissions. The generation of electricity by means of renewable resources offers considerable scope for reduction of such emissions [**1**]. Wind energy is one of the most exploitable forms of renewable energy. Compared to conventional energy sources like coal, oil, hydro and nuclear, wind energy is the most efficient form of energy among all renewable energy resources.

Wind is atmospheric air in motion. Solar radiation differentially absorbed by earth's surface creates a pressure difference due to temperature differences as a result of convection leading to motion of the atmosphere air. However scientists estimate that only 2 percent of sunlight energy is converted into wind kinetic energy [**2**].

1.1 Historical background

Wind and water have long been two main sources of energy for humanity. Water mills and the windmills have been used for applications such as wheat grinding and irrigation [**3**], where animals would otherwise be used as the power sources. Before the invention of steam engines and the conversion of energy from burning coal and later oil, energy from wind was the only way long distance sea transport could be made possible. Probably a windmill was the first turbine to produce useful work without consuming any fossil fuels unlike gas turbines and steam turbines [**4**].

There is no evidence to prove when and where windmills were used for the first time. Some say that the remains of stone windmills have been discovered in Egypt at an estimated age of 3000 years [**5**]. Windmills were used around 3000 years ago in China and Japan [**6**]. According to historians, the first machine utilizing wind energy was operated during 1700BC. Hammurabi used windmills for irrigation in the plains of Mesopotamia [**7**]. The world's oldest windmills had a vertical axis of rotation. Braided mats were attached to the axis. The mats caused drag forces and, therefore, were "taken along with wind" [**8**]. In Persian windmills (Figure 1-1) an asymmetry was created by screening half the rotor with a wall thereby maximizing drag forces to drive the rotor [**8**].

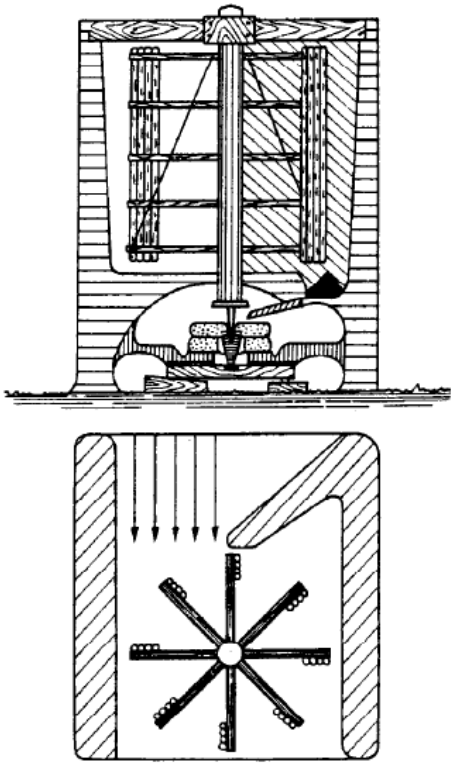

Figure 1-1 Persian windmills for grinding grain [8]

The Chinese used windmills also known as wind wheels. They used these wind wheels to drain rice fields. However it is unknown whether their wind wheel existed before the Persians windmills. The Chinese wind wheel was simple in construction being made of bamboo sticks and fabric sails. They also used the vertical axis rotation concept (Figure 1-2). Chinese horizontal windmills are still in use along the eastern cost of China, north of Yangtez and Tientsin and are used for chain pumps for irrigation purposes and for the salt pan raising [**9**].

Figure 1-2 Ancient Chinese wind wheel [5]

Since the end of the 19th century wind power has been used to generate electricity. The pioneer in this field was Charles F. Brush (1849-1929). He designed the first automatically operated wind turbine as shown in Figure 1-3. He was one of the founders of the American electrical industry, holding several patents in the field of electricity generation [**10**].

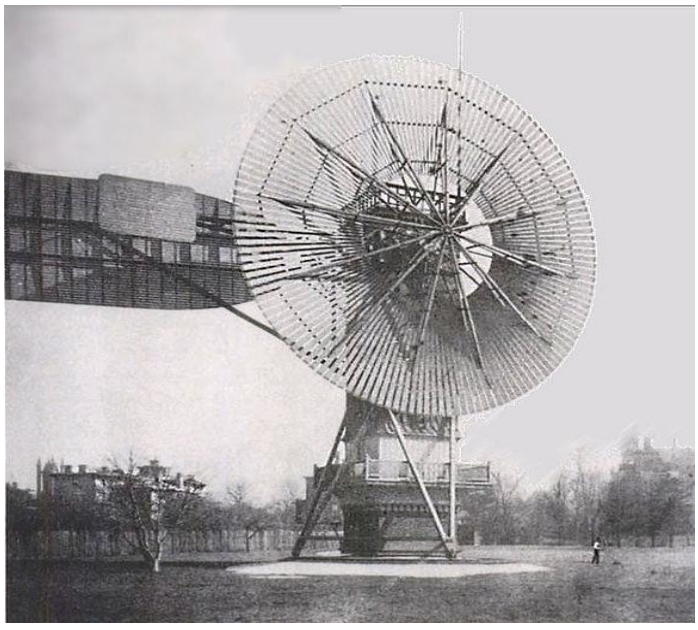

Figure 1-3 First automatically operated wind turbine for electricity [10]

1.2 Modern wind turbines

The modern term for windmills is wind turbines. A turbine is a machine in which vanes or blades are fitted around the wheel to continuously convert fluid energy into mechanical and electrical energy. A wind turbine is used to convert wind energy into electrical energy. After the First World War (1914-1918) the scientific understanding of wind turbine design made a great leap forward, partially based on the experience of propeller design for military and civil airplanes [**8**]. In 1920 Betz applied the actuator disc theory to the wind turbine and found that a maximum of 59% of the kinetic wind energy could be converted into mechanical energy by a free-stream turbine. This was previously discovered by Lanchester in England but Betz took it further, linking the theory of linear momentum and the energy conservation law with airfoil theory. This led to the development by Betz of Blade Element Momentum (BEM) theory which resulted in simple design rules for the blade geometry of optimized wind turbine rotors. With small modifications these basic rules developed by Betz are still used in wind turbine design today [**8**]. These turbines are classified according to two functions – their aerodynamics and their construction design. This leads to basically two types of wind turbine, the Horizontal Axis Wind Turbine and the Vertical Axis Wind Turbine.

1.2.1 Horizontal Axis Wind Turbine

Wind turbines which are based on the aerodynamics principle and use the concept of Betz BEM theory have a horizontal shaft and are known as Horizontal-Axis Wind Turbines (HAWT). The engineer Palmer C. Putnam designed together with the water turbine firm "Smith" the first grid-connected Megawatt wind turbine (Figure1-4) (D = 53m; 1,250kW). Well-known scientists participated in the development of this concept [**8**].

Figure 1-4 Smith-Putman wind turbine [8]

In Germany, Hütter followed with the "Research Association Wind Power" a very innovative turbine concept, leading in 1958 to the prototype W34 (D = 34m, 100kW). It had fiber glass blades, an electro-hydraulic pitch control and produced 50Hz AC power with a synchronous generator [**8**].

Figure 1-5 Hütter wind turbine [8]

1.2.1.1 HAWT basic construction

The most common topology is the HAWT which is a lift based wind turbine with very good performance. Accordingly, it is a popular commercial application and much research has been applied to this turbine.

Wind turbines convert wind energy to electricity for distribution and end-use. A conventional horizontal axis turbine is shown in Figure1-6 and consists of the following components [**11**]:

- ***The Rotor***: The rotor includes the blades for converting wind energy to low speed rotational energy. The rotor is approximately 20% of the wind turbine cost.

- ***The Generator***: The generator includes the electrical generator, the control electronics, and most likely a gearbox (e.g. planetary gear box adjustable-speed drive or continuously variable transmission) component for converting the low speed incoming rotation to high speed rotation suitable for generating electricity. The generator is approximately 34% of the wind turbine cost.
- ***The Structural Support***: The structural support includes the tower and rotor yaw mechanism. The structural support is approximately 15% of the wind turbine cost.

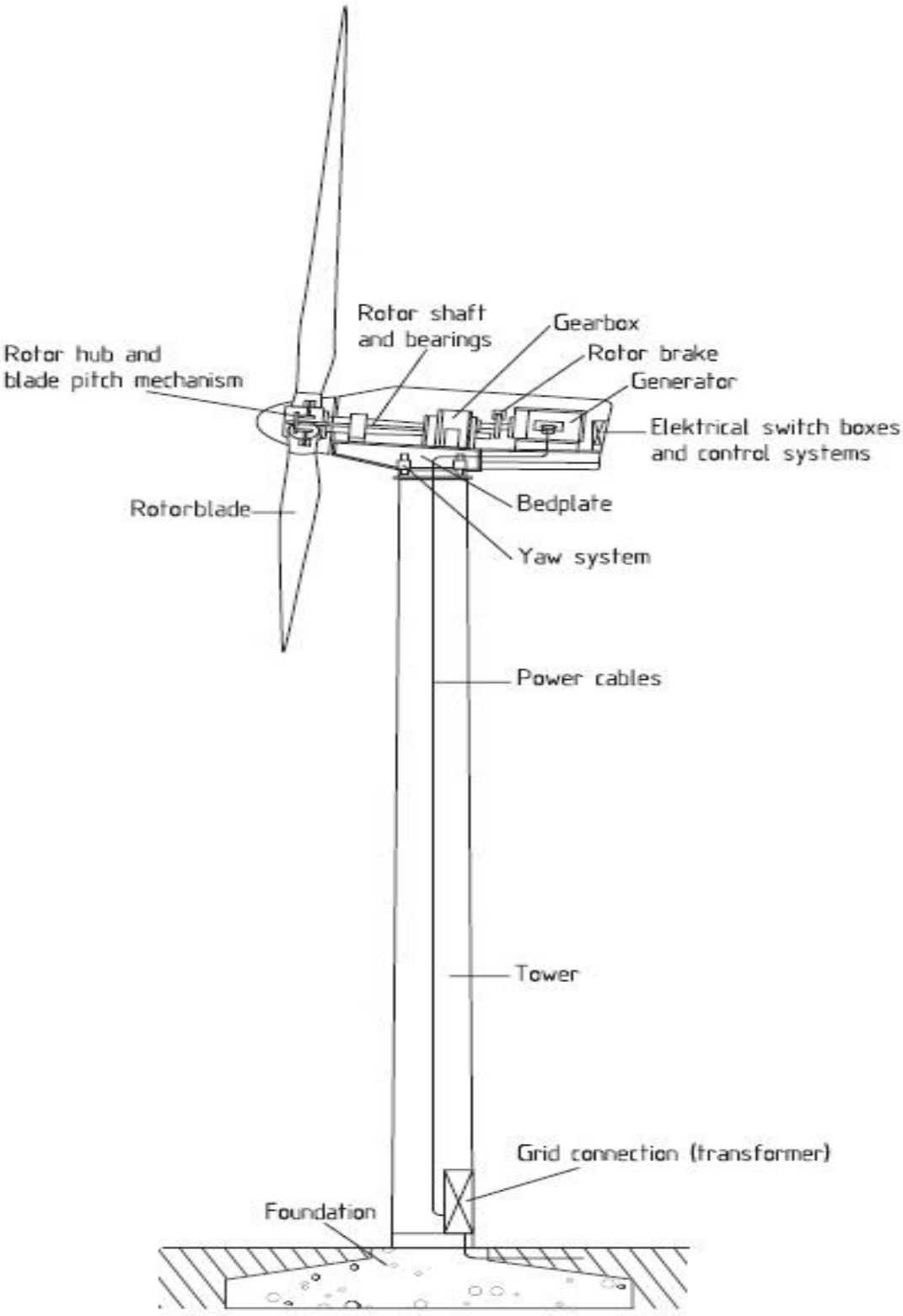

Figure 1-6 Components of HAWT

1.3 Vertical Axis Wind Turbine

The wind turbines which are based on aerodynamics principles and have a vertical axis are known as Vertical Axis Wind Turbines (VAWT). The Darrieus wind turbine (Figure1-7) is a type of VAWT used to generate electricity from the energy carried by the wind. The turbine consists of a number of airfoils, sometimes vertically mounted on a rotating shaft or framework. This design of wind turbine was patented by Georges, a French aeronautical engineer in 1931 [**12**].

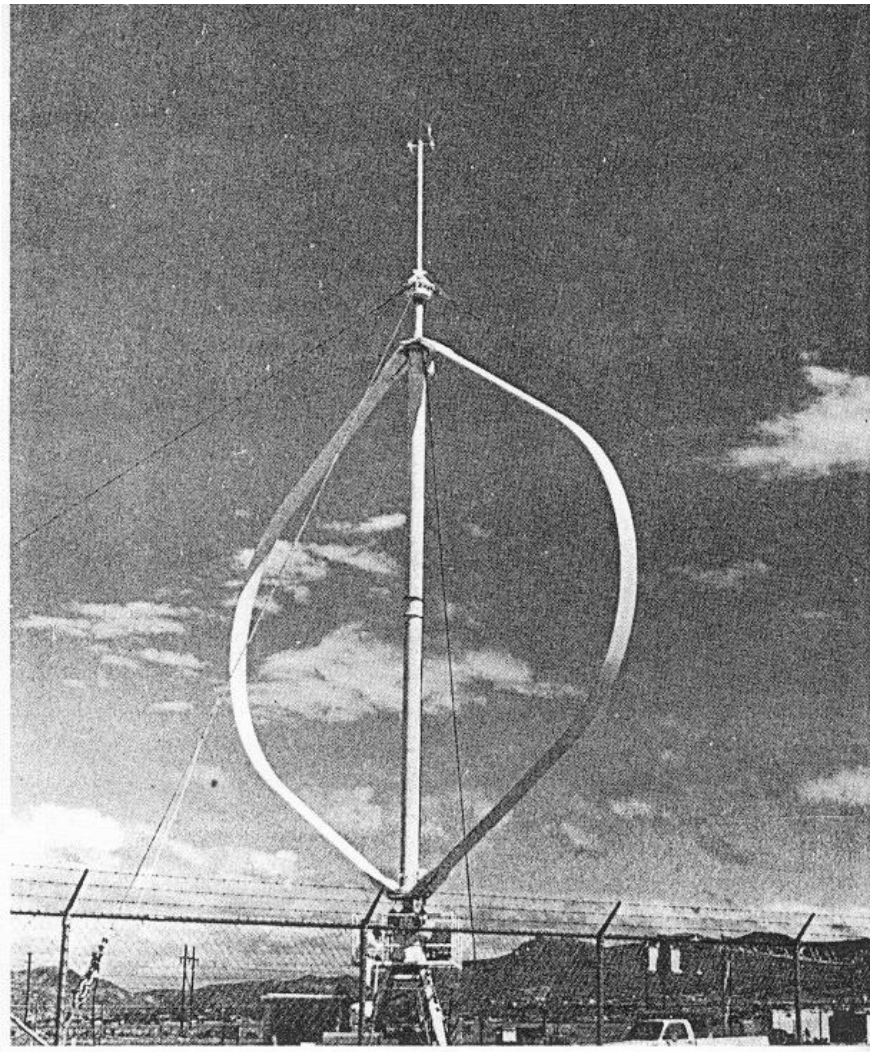

Figure 1-7 Sandia Laboratories 17-m Darrieus, rated at 60kW in a 12.5m/s wind [13].

A different approach to the vertical axis wind turbine was developed by Savonius during the same era of Darries in Finland. This vertical axis wind turbine as shown in Figure 1-8 does not require orientation into

the wind direction. Technological enthusiasts developed a Savonius rotor at Kansas State University, Manhattan, Kansas [**13**].

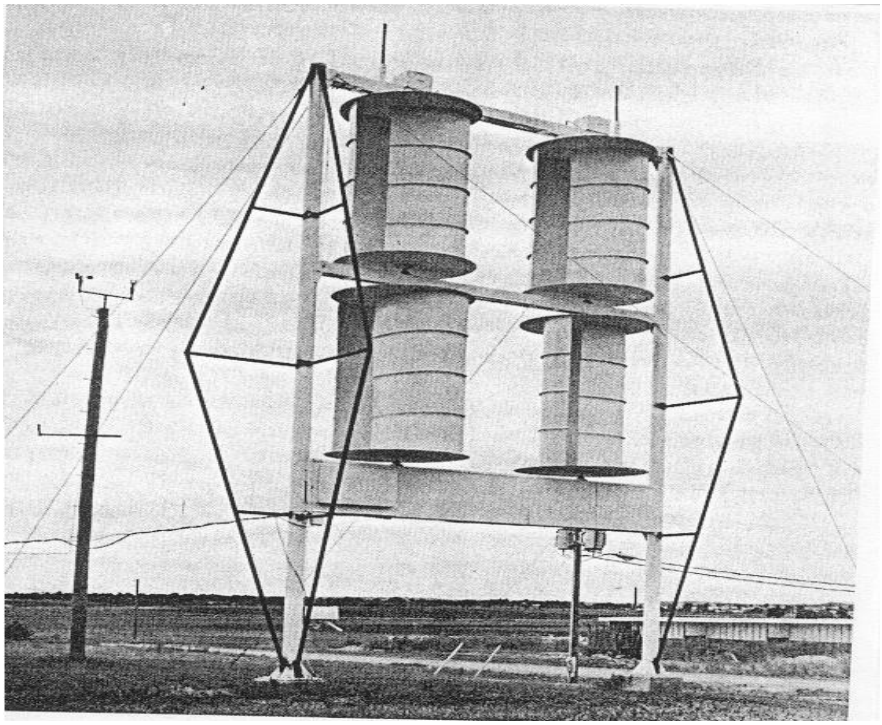

Figure 1-8 Kansas State University Savonius, rated at 5kW in a 12-m/s wind [13]

1.4 Objectives

The surging demand of energy in South Africa requires development of new technologies that are more efficient and less hazardous to our environment. Most countries throughout the world are moving towards cleaner and green technology. Construction of wind farms is one of the most suitable technologies for energy production but developing a wind turbine which can provide stand-alone energy production in urban areas where it is not possible to install big turbines is most beneficial.

1. Homes in the urban area are mostly surrounded by mega structures which obstruct the flow of the wind. In addition, it is not possible to install big turbines in urban areas because there is usually not enough high speed wind to provide enough kinetic energy to move the massive turbine blades. Therefore, avoiding big and massive structures and being able to gather more and more wind energy in the urban area where the wind speed is circumstantially lower than in open rural areas, is desirable. Introducing a double shroud around the turbine to gradually increase the wind

speed and hence increase efficiency is the key to improving wind turbine efficiency to the same capacity as those in rural areas.

2. These Double Shrouded Horizontal Axis Wind Turbines (DSHAWT) can be implemented anywhere to produce clean energy with low wind speed. They can be installed on roof tops of homes, on top of buildings and under bridges to capture unused wind energy in the urban areas.

1.5 Wind energy potential in South Africa

South Africa seeks capacity and skills development for methods and data that would enable the authorities, investors, power sector and industry to investigate and plan for large-scale exploitation of wind power for electricity generation. This requires a methodology for mapping the wind resources on national and regional scales, as well as tools for estimating reliably the annual energy production (AEP) of proposed wind farms all over South Africa. The project in question is to be implemented as a so-called twinning arrangement between the South African project partners and Risø DTU. The main aim of the winning program is to develop and employ numerical wind atlas methods and develop capacity to enable planning of large-scale exploitation of wind power in South Africa, including dedicated wind resource assessment and siting tools for planning purposes, i.e. a Numerical Wind Atlas and database for South Africa. The Wind Atlas of South Africa (WASA) can find applications in at least two areas, namely to assist in the development of large grid connected wind farms and to provide more accurate wind resource data to identify potential off-grid electrification opportunities. The WASA is financially supported by the Royal Danish Embassy (RDE) and the Global Environment Fund (GEF) through the South African Wind Energy Project (SAWEP). SAWEP is a DOE anchored project which originated from the declaration by the then Minister of Minerals and Energy in June 2000 of the Darling Wind Farm as a National Demonstration Project and her request for international assistance in particular from the Global Environment Facility (GEF) and Danida (Danish International Development Agency). The 2-year UNDP/GEF SAWEP initiative sought to make available ‘Technical Assistance’ to the South African Government in terms of policy making and the development of the most appropriate financial instruments for policy implementation [**14**].

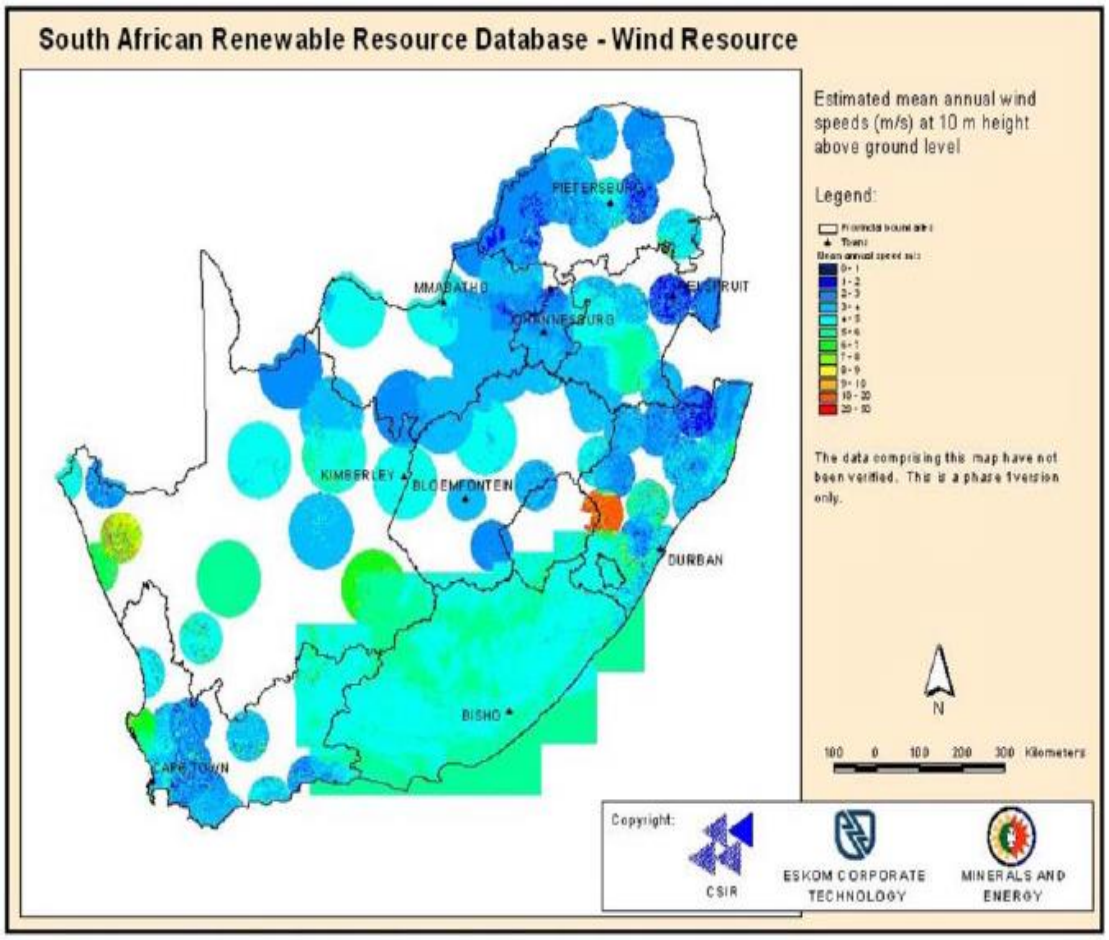

Figure 1-9 Estimated mean annual speed (m/s) at 10m height above ground [14]

The wind resource map that was generated by 3E presents the estimated mean annual wind speed at 100m above ground level (AGL) as shown in Figure 1-10 for the entire eThekwini region and identifies a number of areas in the eThekwini region with wind speeds in excess of 6.5m/s as well as a larger number of areas having a wind speed between 6.0m/s and 6.5m/s. Moreover, there are a number of areas across the study area that retained wind speeds between 5.0m/s and 6.0m/s, albeit large tracts of these areas are urban/suburban areas. In particular, the entire coastal region returned a wind speed of between 5.53m/s and 6.0m/s with some coastal areas retaining wind speeds of between 6.0 and 6.5m/s [**15**].

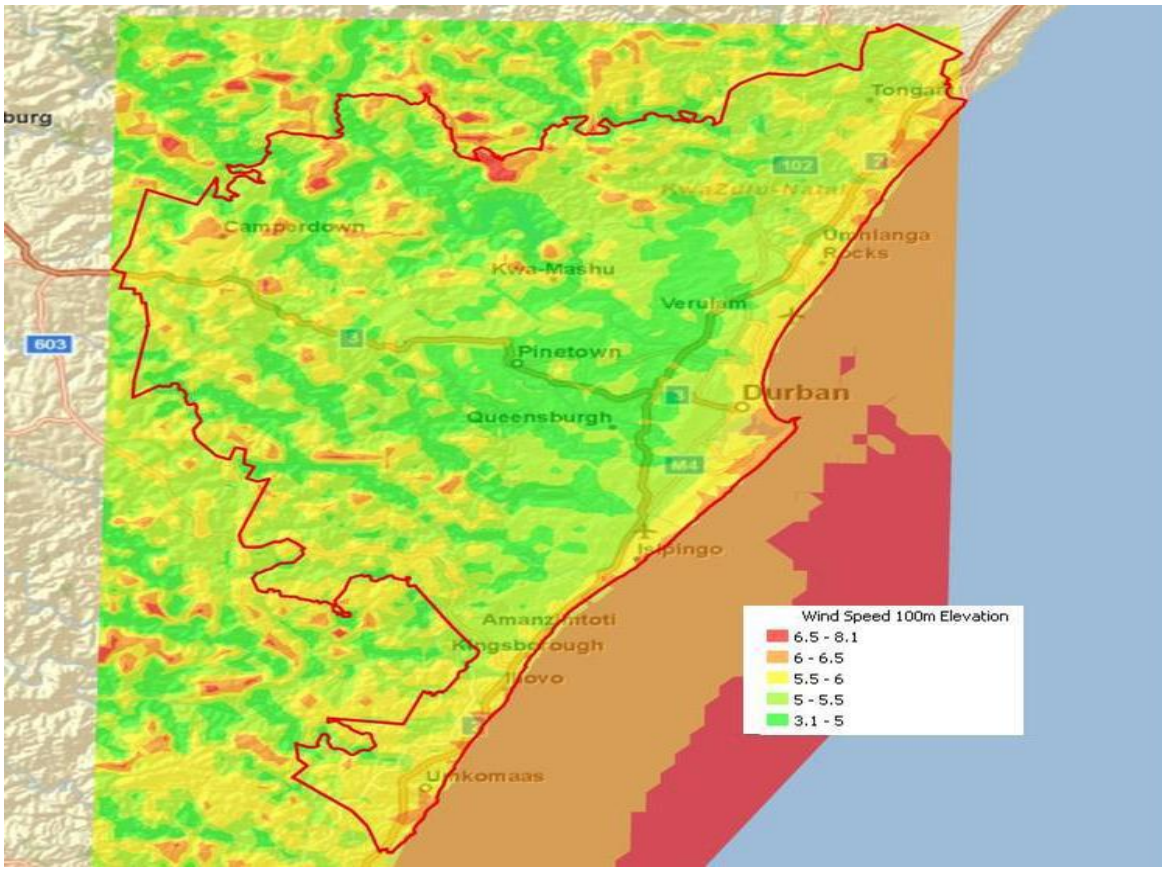

Figure 1-10 Wind resources across eThekwini Region at 100m AGL [15]

1.6 Application of wind turbines

Wind energy can be used in various methods as discussed in the Section 1.5 and power generation remains the most viable option. This can be obtained by installing large wind farms.

A wind farm is a group of wind turbines in the same location used for production of electric power. A large wind farm may consist of several hundred individual wind turbines, and cover an extended area of hundreds of square kilometers, but the land between the turbines may be used for agricultural or other purposes. A wind farm may also be located offshore.

Many of the largest operational onshore wind farms are located in the USA, of which Roscoe wind farm is the largest [**16**] onshore wind farm in the world with an installed capacity of 781.5MW.

There are currently no large scale wind farms operational in South Africa, though a number are in the initial planning stages. Most of these are earmarked for locations along the Eastern Cape coastline.

Eskom has constructed one small scale prototype wind farm at Klipheuwel in the Western Cape and another demonstration site near Darling where Phase 1 has been completed.

Ten sites were identified as potential sites within the EMA (eThekwini Municipal Area) that could be considered for further investigation as illustrated in Table 1-1. It should be noted that these sites were identified purely from a wind resource perspective. Further assessment of ownership, access, zoning, etc. still needs to be conducted [**15**].

Table 1-1 Potential 10 sites for wind farms within EMA [15]

Site Number/ Google Maps Link	Number of Turbines	Capacity MW	Mean Wind Speed (m/s)	Area (km^2)	Landmark/Area
site 1	10	25	6.5	2.337	Nagl Dam; Valley of a Thousand Hills; Sithumba
site 2	8	20	6.2	1.591	Directly south of Nagl Dam; west of Mr423 Road
site 3	11	27.5	7.3	2.249	Inanda Dam North
site4	9	22.5	6.2	1.873	Inanda Dam South East
site 5	8	20	6.7	1.476	Shongweni Dam South; south of Mr489 Road
site 6	9	22.5	6.6	1.231	Umlazi North West; Inwabi
site 7	9	22.5	6.2	2.153	Shongweni Dam West; directly next to Mr489
site 8	6	15	6.6	0.789	Inanda Dam Langefontein
site 9	8	20	6.6	1.158	Camperdown Rural; directly next to N3
site 10	8	20	6.7	1.324	Nkomokazi; Umbumbulu

1.7 Proposed research hypothesis

In this study we have developed two airfoil ring like structures in such a way that one forms the mirror of the other across the mirror line as shown in Figure 1-11 and then revolving it around the axis of

revolution to make a complete shroud. From the construction point of view we have adapted the design of the outer shroud as it was used by [**17**] to keep the design lighter and more economical.

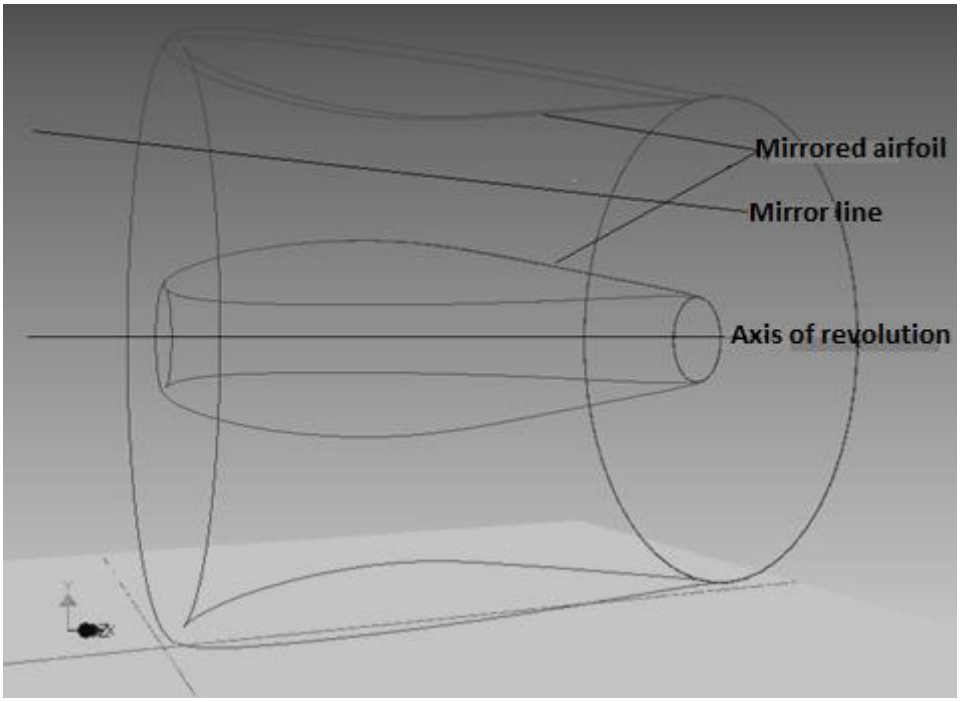

Figure 1-11 Wire frame

This design raised the question of how and where to accommodate the wind turbine inside the shroud. To solve that problem the lower shroud is divided into two parts, namely, front section and rear section as shown in Figure 1-12. The hub rests inside the lower shroud and the hub shaft which holds the turbine blades passes in the space between the front and rear section of the lower shroud. Both the outer and lower shroud have an airfoil profile shape and are connected rigidly to each other by means of back ribs to support the rear section of the lower shroud and front ribs to support the front section of the lower shroud as shown in Figure 1-12. Only three strong ribs in back and three ribs in front are used, to avoid any kind of hindrance in the wind path. The angle of attack of the airfoil for both the outer and lower shroud for the forward wind is 10^{o}. The internal structural design of the shroud profile is such that the total weight of the structure remains low and economical without compromising its strength and durability.

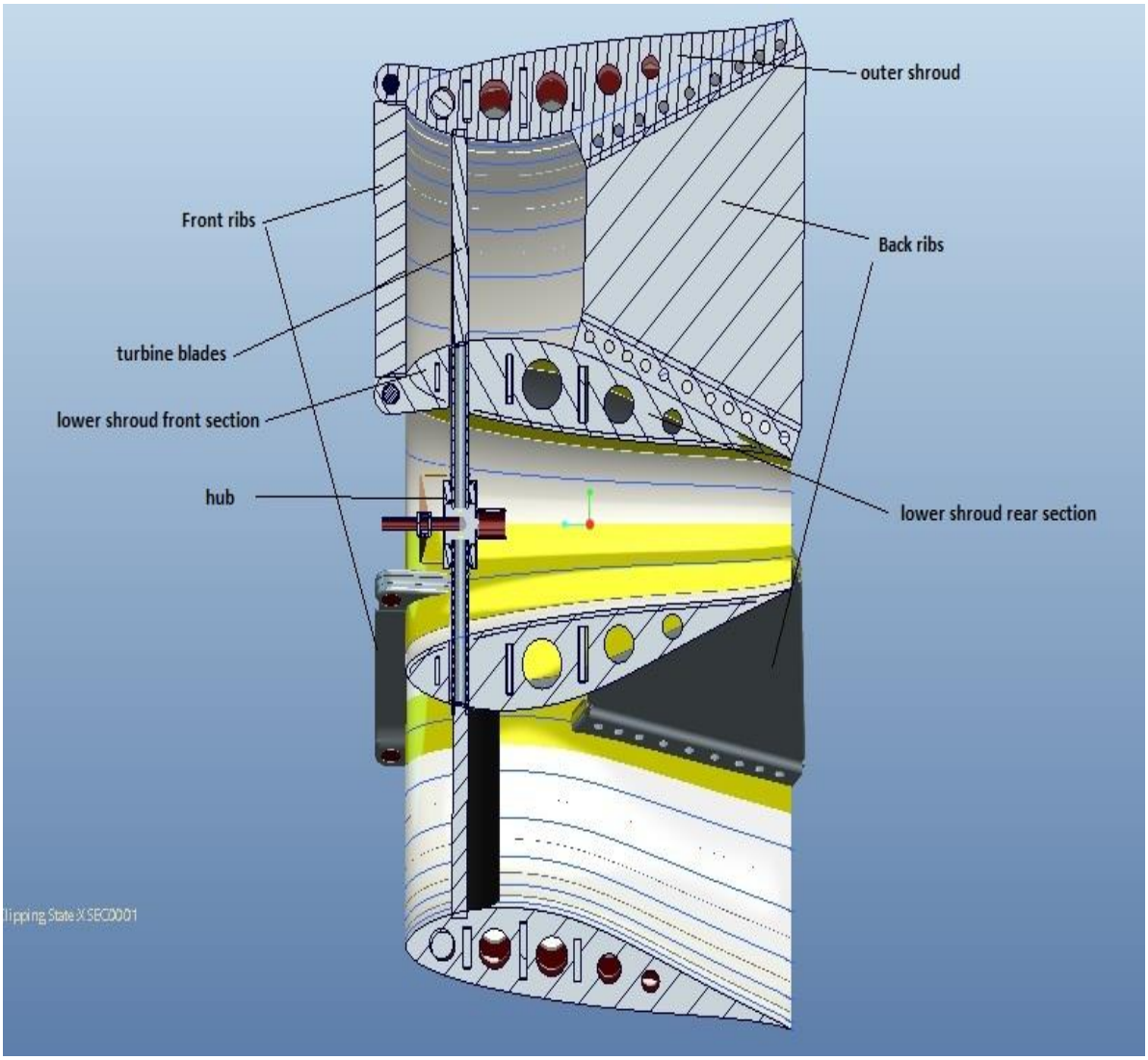

Figure 1-12 Detailed cross sectional view of double shrouded HAWT

Figure 1-13 shows a propeller type wind turbine with a double shroud which surrounds the wind turbine and is shown for the sake of construction possibility of the design.

For this research study various airfoil design data was chosen from the NACA airfoil data bank [**18**] for both outer and inner shroud design by using "Autodesk Inventor Professional 2012" (Autodesk® Inventor® 2012).

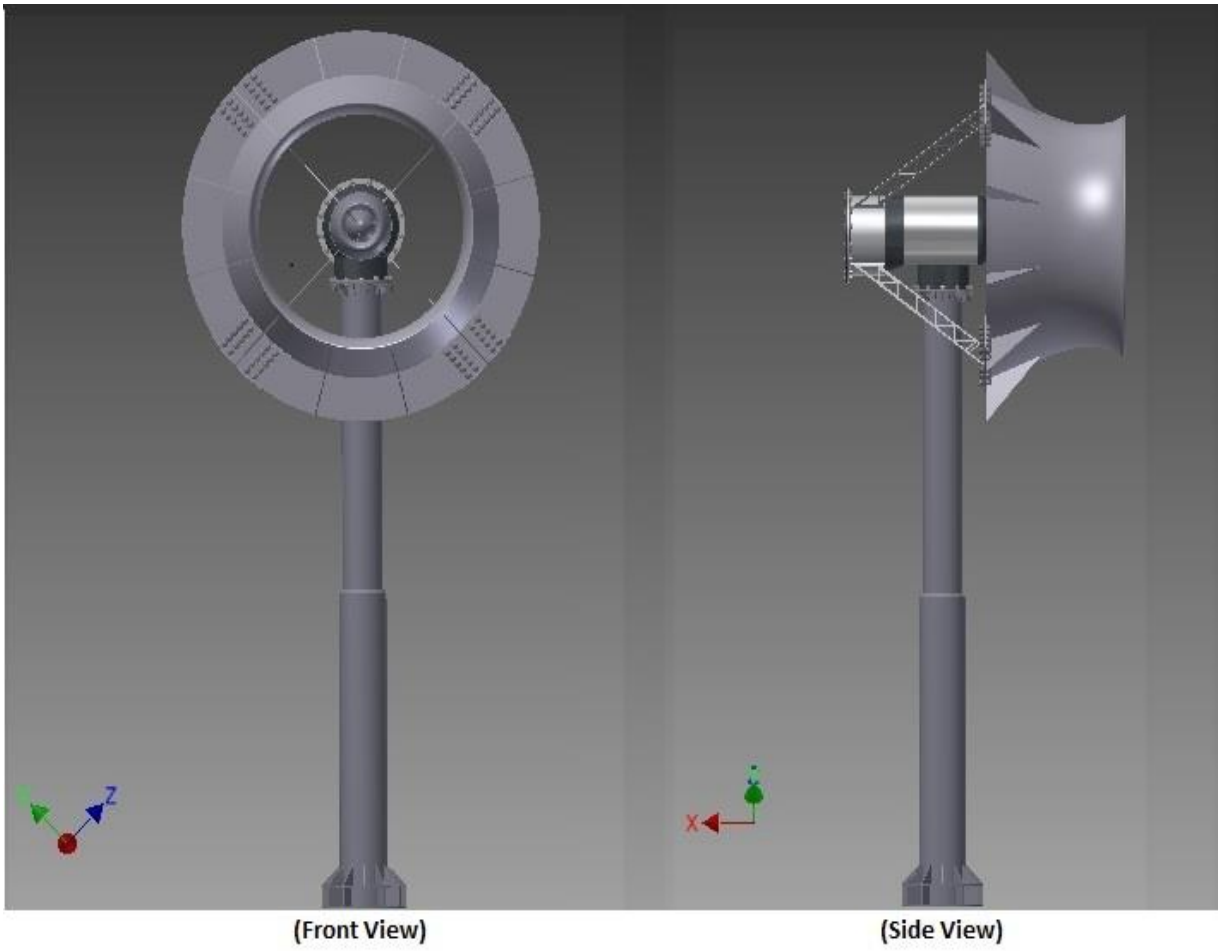

Figure 1-13 Proposed design of double shroud with flanged end

1.8 Layout of the dissertation

The first chapter focused on the background study of wind turbines and the evolution of the windmill to wind turbine and also to introduce a new design of the shroud to overcome the low wind speed due to urbanization and different hindrances which causes low wind speed and to extract wind energy from lower wind speed.

The second chapter consists of research studies conducted by various researchers and includes a detailed literature review regarding the Diffuser Augmented Horizontal Axis Wind Turbine (DAHAWT). In addition it contains the mathematical descriptions which are necessary to depict the performance of the shrouded wind turbine including the energy, mass and momentum mathematical formulations using the Computational Fluid Dynamics (CFD) approach.

The third chapter contains the research and design methodology comprising double shroud modeling with flanged end and the CFD results and calculation and selection of the best design for the maximum power and flow output. The CFD results are also used for finite element analysis to optimize the design.

The fourth chapter presents the comprehensive results collected from the rigorous simulation in chapter three. These results are basically the CFD and Finite Element Analysis (FEA) for various part of the shroud design. These results are carefully studied and presented in tables for better understanding and further changes are made in the design to optimize the results.

The fifth chapter mostly concentrates on the performance of the new proposed shrouded design throwing light on the up gradation of the existing conventional wind turbine to the new proposed design to maximize the output of power from wind using this wind turbine. Further implementation and recommendations for future study are highlighted..

2. LITERATURE REVIEW AND BASIC THEORY

2.1 Introduction

In the past few years global warming has become the biggest global issue for the world and has induced a demand for clean energy systems. It has been established that wind energy is the best energy resource among all the renewable energy resources. The development and application of renewable, clean energy has become a very important issue in recent years due to the serious effect of global warming and rapid depletion of fossil fuel [**19**]. There is a great need for the introduction of stand-alone power supply systems for sites such as radio relay stations in mountain areas where commercial power cannot be supplied [**20**]. Therefore, the introduction of a new wind power system that produces higher power output even in an area where low wind speeds and complex wind patterns are expected is strongly desired [**21**]. The power P_w that can be extracted according to Betz [**1**] is given by:

$$P_{max} = \frac{8}{27}\rho A_r v^3 \qquad (2.1)$$

where:

ρ	Density of air	[kg/m^3]
A_r	Area wind turbine	[m^2]
v	Wind Velocity	[m/s]

From the above equation wind power generation is proportional to the wind velocity cubed. Therefore, a large increase in output is brought about if it is possible to create even a slight increase in the velocity of the approaching wind to a wind turbine [**21**]. If we can increase the wind speed by utilizing the laws of fluid dynamics around a structure or topography, namely if we can concentrate the wind energy locally, the power output of the wind turbine can be increased substantially [**21**]. The power of the wind turbine can be increased by creating a field of low pressure behind the propeller [**22**].

A lot of studies have been made with regards to extracting wind energy using diffuser augmented wind turbines [**19**] [**20**] [**23**] [**21**]. All these studies are focused on the single shroud with flanged end which is a simple funnel like structure with a wide open angle to concentrate the wind energy. In 2003 Bet and Grassmann [**22**] developed a wing profile ring structure in the category of shrouded wind turbine. They reported that it is possible to increase the power of wind turbine by factor of 2 by the means of placing a wing structure around the turbine [**22**]. In this study we have developed two airfoil ring like structures in such a way that the one forms the mirror of the other across the mirror line as shown in the Figure 1-11 and then revolving it around the axis of revolution to make a complete shroud. For the construction point of view we have adapted the design of the outer shroud as it was used by [**17**] to keep the design lighter and more economical.

2.2 Literature survey

Chen and Cheng [**19**] observed that mounting the shrouded horizontal axis wind turbine on moving vehicles can also be very useful in terms of generating power. In their experiment they used a wind turbine with the flanged end diffuser of rotor size 30cm with a solidity of 20%-60% and a wind speed of 10-20m/s. The wind tunnel test result shows that a rotor with a solidity of 30%-40% generates the largest power and torque in comparison with a rotor with a solidity of 60%. Their study concluded that a small wind turbine has low torque, high rotational speed and high rotor solidity for maximum power output compared to a conventional large wind turbine.

Karasudani et al. [**21**] developed a shrouded wind turbine with a broad-ring shaped flange at the exit periphery of the shroud and a horizontal axis wind turbine inside. The placement of the flange at the exit is emphasized since the flange generates a low pressure field behind the flange due to vortex formation which happens due to mixing of the different flows of the wind mass at the end of the flange. This vortex forces more air mass inside the shroud and over the blades of the wind turbine inside. They performed a wind tunnel test and output was augmented by a factor of 4-5 compared to a bare wind turbine.

Ozer [**24**] proposed to enclose a wind turbine inside a specially designed shroud using various geometrics for the shroud. The results showed a significant power augmentation. He introduced a ring-shaped flap boundary layer control technique to optimize their results [**25**]. They demonstrated a significant 25% improvement in the efficiency of a wind turbine using an appropriate ring shaped shroud. A pilot plant producing 1hp at 5m/s with a 3m diameter turbine was built in order to carry out the experiment.

Foreman et al [**26**] performed a test on a diffuser augmented wind turbine. The test results show almost doubling of the wind power extraction capacity for DAWT as compared to a conventional wind turbine. Alaydi's [**27**] results show that the diffuser area ratio of 3 gives maximum augmentation. He also found in the economic assessment that the effective power cost was lower than the conventional wind turbine with a very large size rotor. Foreman [**26**] of the Solar Energy Research Institute SERI prepared a report under the auspices of the Grumman Aerospace Corporation, New York. The main objective was to assess the economic feasibility of a shrouded wind turbine or Diffuser Augmented Wind Turbine (DAWT).

Bussel et al. [**28**] estimated that adding small tip-vane auxiliary wings on the blade tips of horizontal axis wind turbines enhances the lift force in the direction of the axis which in turn deflects air radially outwards resulting in a diffuser affect. Bussel et al. also found that introducing a vane at the tip of the blade also helps eliminate tip vortices at high "TSR" tip speed ratio and increases the thrust coefficient by 1.5 as compared to 0.89 for conventional bare wind turbines. They also predicted a four-fold increase in mass-flow with augmentation 2.5 times that of conventional wind turbines.

Subramanian et al. [**29**] conducted a study on diffuser augmented wind turbines using hub-less wind generation. In a conventional wind turbine the rotor blades are mounted on the hub of the wind turbine but in these experimental studies blades are integrated with the circumference of the rotating ring. This ring housing facilitates the bindings and permanent magnets help in power generation using the concept of a DC induction brushless generator. The ring also gives the additional advantage of stud support to the blades and eradicates small vortex formation at the tip. CFD modeling gives promising results of power absorption.

Abe et al. [**30**] carried out experimental and numerical studies to depict the flow field of a small wind turbine with a flanged shroud. To explain and analyze the mean velocity profile behind the turbine a hot wired technique was used. The results were compared with those of a bare wind turbine and the difference was experienced as an elimination of tip vortex.

Kosasih and Tondelli [**31**] studied shrouded wind turbines and concluded that performance augmentation depends upon many factors including geometry of the shroud, airfoils and wind conditions. They carried out an experiment using different shapes and combinations of geometries such as straight diffuser, nozzle diffuser combination and brimmed diffuser combination. The design of the diffuser was determined as length (L/D=0.63 to 1.5) and flange height (H/D=0 to 0.2). Their test assessment shows that placing the

micro wind turbine inside the shroud enhances the performance of the turbine. The diffuser alone enhances the performance by 60% and the nozzle-diffuser enhances the performance by 63% as compared to a bare wind turbine. They also noticed that adding a flange at the end of the shroud (brimmed) remarkably increases the performance and also reduces the cut-in speed of the wind turbine.

Kishore et al. [**32**] designed a small scale portable wind turbine (SWEPT) which operates below 5m/s wind speed. Wind tunnel examinations were performed extensively to maximize the coefficient of performance of about 14% at the TSR of 2.9 at a very low cut-in wind speed of 2.7m/s using CFD simulation. They observed that a SWEPT produces 1.4 to 1.6 times more power than a bare wind turbine.

Aranake et al. [**33**] used the high resolution RANS Reynolds Averaged Navier-Stroke equation to developed shroud geometries capable of capturing high mass flow through the shroud. The researchers used airfoils Selig S1223 which have a high lift and low Reynolds number. The maximum augmentation was recorded as 1.9 times a bare wind turbine.

Angus [**34**] used four concentric airfoils to shroud the horizontal axis wind turbine. The main objective was to extract power similar to big diameter wind turbines without increasing the diameter of the turbine because big turbines brings hazards to birds since they can't see the big turbine blades running at high speed and get themselves killed during flight. However, using multiple shrouds around the turbine increases the visibility of the object and also encloses the moving parts inside the shroud.

Howey et al. [**35**] developed a 2cm diameter shrouded wind turbine using a 6 blade and 12 blade design. PCB Printed Circuit Board and flexible machining helps to achieve this small scale shrouded wind turbine and also utilized a jewel bearing for low friction. Wind tunnel tests performed with the 12 blade design recorded a 4.3mW power output at 10m/s wind speed. The main objective is duct sensing applications which do not need to rely on external power sources.

Presz and Werle [**36**] invented a shrouded wind turbine using the concept of the Mixer Ejector system to increase the efficiency of the bare wind turbine. They utilized the advance mixing technology single and multistage ejector which increase the energy extraction of the turbine

2.3 Development of shrouded wind turbines

The Betz limit is well known for the wind turbines which say that wind turbines give a power coefficient of 16/27. However the present wind turbine system was able to break the boundaries and was capable of overcoming this limit by introducing the shroud system around the turbine with a small near opening and a wide end opening. Some researchers put the airfoil ring like structures around the turbine to obtain more efficiency with the same class of turbine.

2.3.1 Preliminary design of Diffuser Augmented Wind Turbine (DAWT)

The preliminary Diffuser Augmented Wind Turbine (DAWT) was one of the first innovative wind energy conversion system designs to be funded by the U.S government and has been funded within the Grumman Aerospace funding program since 1975 [**37**]. This system is based on the concept that mass flow through the wind turbine can be significantly increased beyond the best of bare turbine operational conditions by the use of a diffuser to maintain a low pressure field downstream of the wind turbine. The suction created beyond this sub-atmospheric pressure enhances the air flow and increases the turbine power output well beyond conventional bare turbines [**37**]. Figure 2-1 shows the basic schematic of the DAWT with its flow field stream tube boundaries compared to those of a bare turbine. In this figure the cross-sectional view is shown in which the wind turbine is surrounded by a diffuser which is guiding the air into a concentrated region over the rotor.

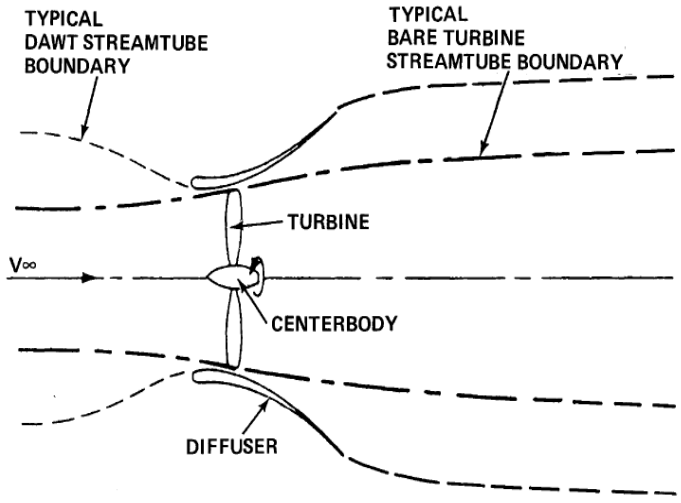

Figure 2-1 Basic schematic of the DAWT [37]

2.3.2 Small wind turbine with a flanged diffuser

In 2005 Abe et al. [**30**] developed an effective wind-acceleration system with a diffuser-shaped structure surrounding a wind turbine. A flange was introduce at the end to separate where a very low pressure region appears to draw more wind compared to a diffuser with no flange due to this flow coming into the diffuser being more effectively concentrated and accelerated. In this system the maximum velocity is obtained at the near the inlet of the diffuser and thus the wind turbine is placed there as shown in Figure 2-2 [**30**].

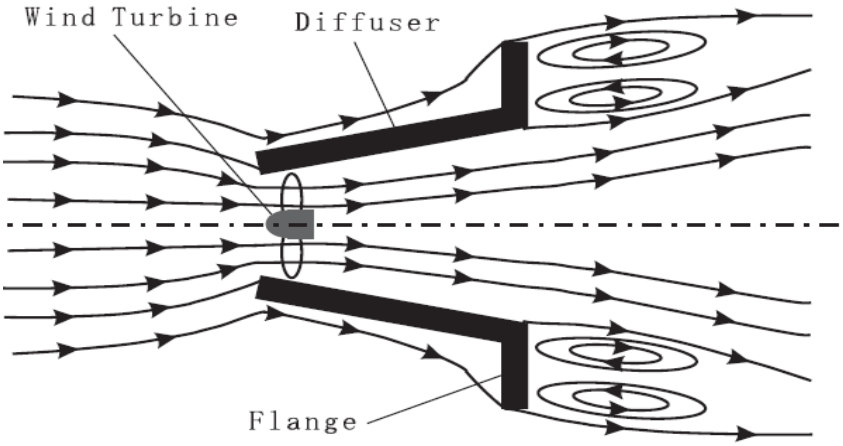

Figure 2-2 Flow mechanism around a flanged diffuser [30]

Figure 2-3 Schematic view of a diffuser shrouded wind turbine [30]

Figure 2-3 shows the schematic view of a flanged end diffuser type wind turbine where the three blade rotor placed at the center of the diffuser assembly is being tested in a wind tunnel.

2.3.3 Scoop design for small domestic wind turbine

In order to improve wind energy capture under low wind speed conditions in a built up area, the design of small wind generator for domestic use in such areas has been explored. Figure 2-4 shows the boundary condition pre-set for the computation fluid dynamic analysis while Figure 2-5 shows the scoop design in two dimensions. The primary results of the CFD analysis show a boost to airflow speed by a factor of 1.5 times equivalent to an increase in power output of 1.5^3 times with the same swept area. Use of a scoop also increases the efficiency of a wind turbine under low wind conditions [**38**].

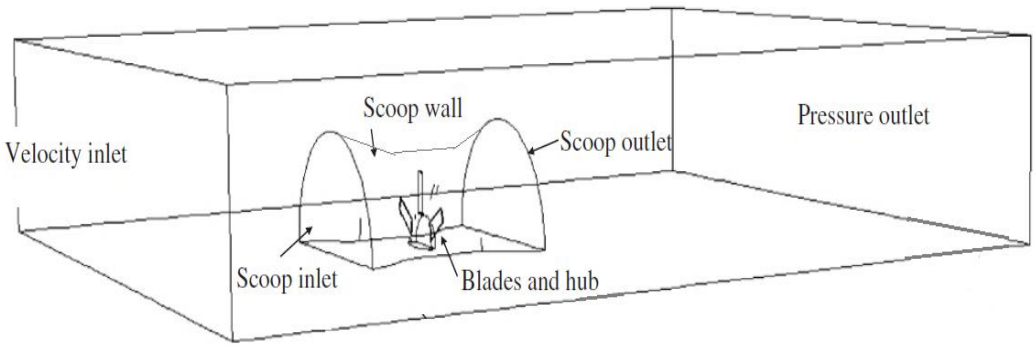

Figure 2-4 Computational domain with boundary condition for CFD test [38]

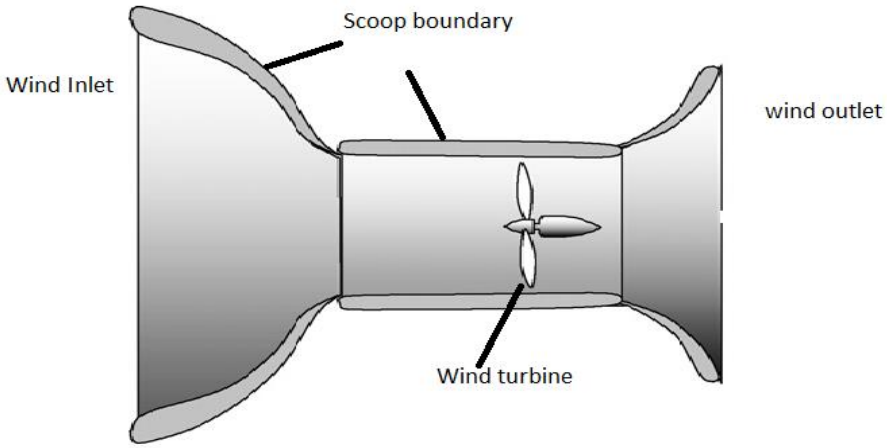

Figure 2-5 Design of the scoop [38]

2.3.4 Experiments with different shapes of shroud for wind turbine

In order to get the maximum accelerated wind speed inside the shroud the research team of Research Institute for Applied Mechanics, Kyushu University used three typical hollow structures as shown in Figure 2-6: a nozzle-type model that reduces the inside cross-section; a cylindrical-type model that has a constant inside cross-section, and; a diffuser-type model that expands the inside cross-section downstream [**21**].

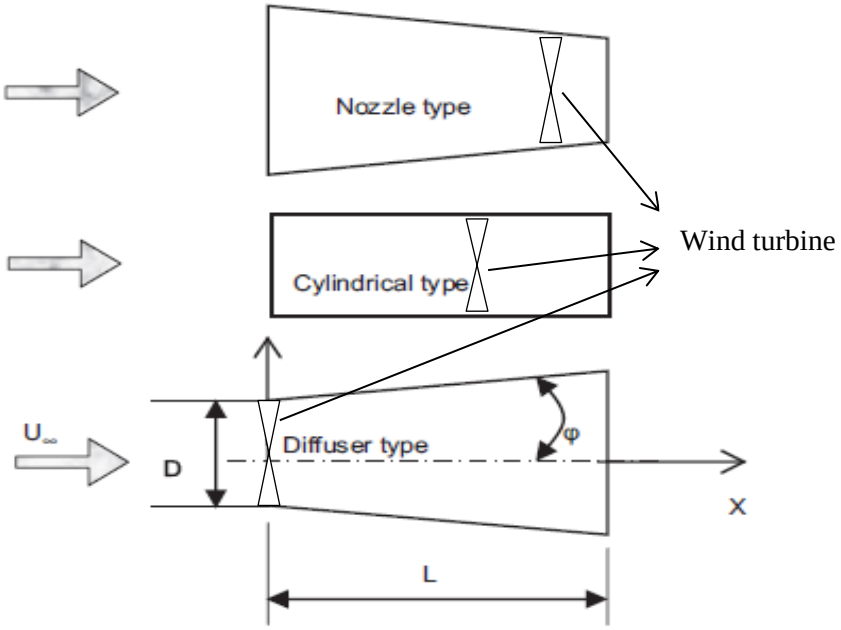

Figure 2-6 Three types of hollow structure [21]

All these hollow structures were tested inside a wind tunnel of 3.6m wide X 2m high X 15m long at a maximum wind test velocity of 30m/s. The results were examined on the basis of wind velocity and the static pressure distribution on the central axis of the hollow structure. The wind tunnel test on the cylindrical structural did not show much deviation but the nozzle type and diffuser type structures showed remarkable results as can be seen in Figure 2-7 [**21**].

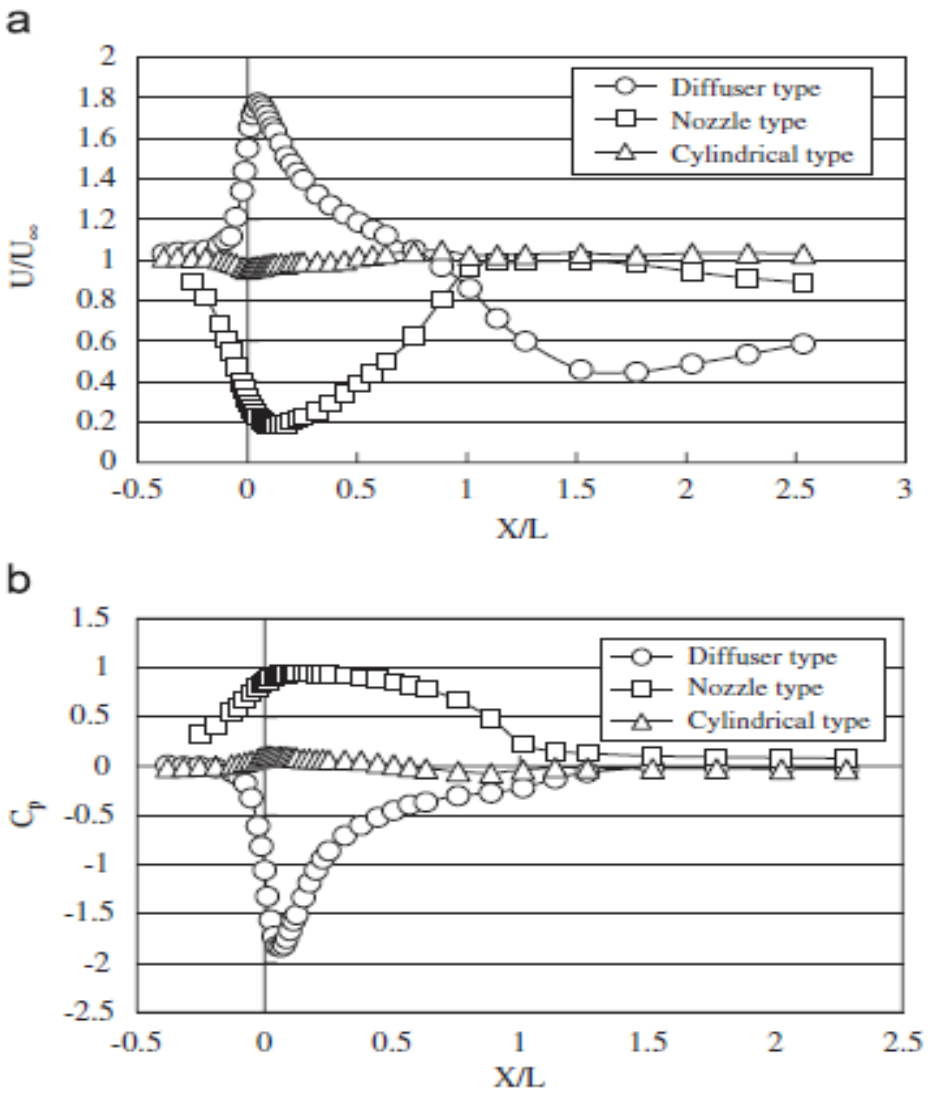

Figure 2-7 (a) Wind velocity and (b) static pressure [21]

2.3.5 Broad ring flanged shrouded wind turbine

The schematic diagram of a broad ring flanged shrouded wind turbine is depicted in Figure 2-8. This Diffuser Augmented Wind Turbine (DAWT) consists of a diffuser shroud with a broad-ring flange at the exit periphery and a wind turbine inside. The flanged-diffuser shroud device plays the role of collecting and accelerating the approaching wind. The flange generates the low pressure region in the exit neighborhood of the diffuser by vortex formation and draws more mass flow to the wind turbine inside the diffuser shroud [**21**] [**39**].

Figure 2-8 Broad ring flanged shroud [39]

2.3.6 Shrouded wind turbine with compact diffuser (wind lens)

This type of wind turbine was proposed with the aim of taking the weight and size parameters into account, since large shrouded wind turbines are difficult to fabricate and the load of the wind over the shroud is very high in high wind speed and it is not easy to design complex structures to bear the load of such winds on the surface of the shroud. By keeping the load and the economic factor in mind a team of researchers headed by Yuji proposed a wind lens design which is a very compact collection-acceleration structure utilizing a compact flanged diffuser (see Figure 2-9) [**40**].

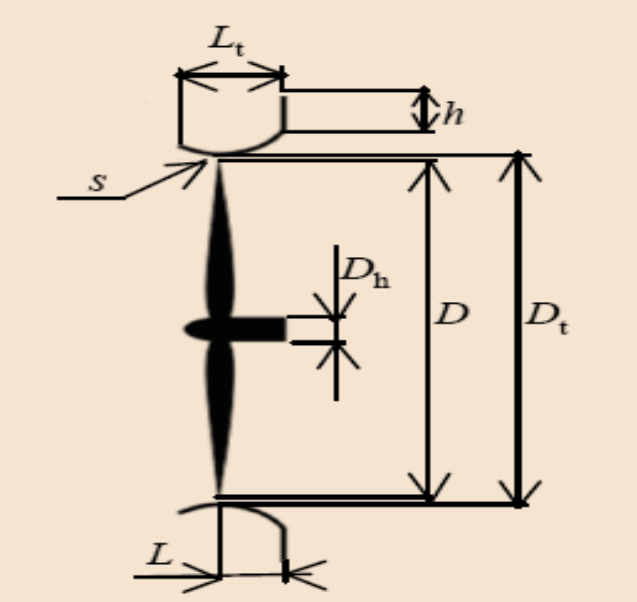

Figure 2-9 Dimensions description of wind lens [41]

As can be seen from Figure 2-9, the length L_t is much less compared to D diameter i.e. L_t < 0.4 D as shown in (Figure 2-10) [**41**]. To bring the plan into reality two 100kW wind-lenses as shown in Figure 2-10 have been installed at Ito Campus, Kyushu University, Japan.

Figure 2-10 100kW wind lens turbine [40]

2.3.7 Miniature shrouded wind turbine

This shrouded wind turbine is aimed at energy harvesting for power delivery to wireless sensors in pipes and ducts. This device has a rotor diameter of 2cm, with an outer diameter of 3.2cm, and generates electrical power by means of an axial-flux permanent magnet machine built into the shroud (see Figure 2-11). This device can operate at low air speed of up to 3m/s [**35**]. The advantage of using such a small scale turbine is that it can be installed in very small spaces to provide energy to a sensor installed in ducts and pipes which run on very low voltage current.

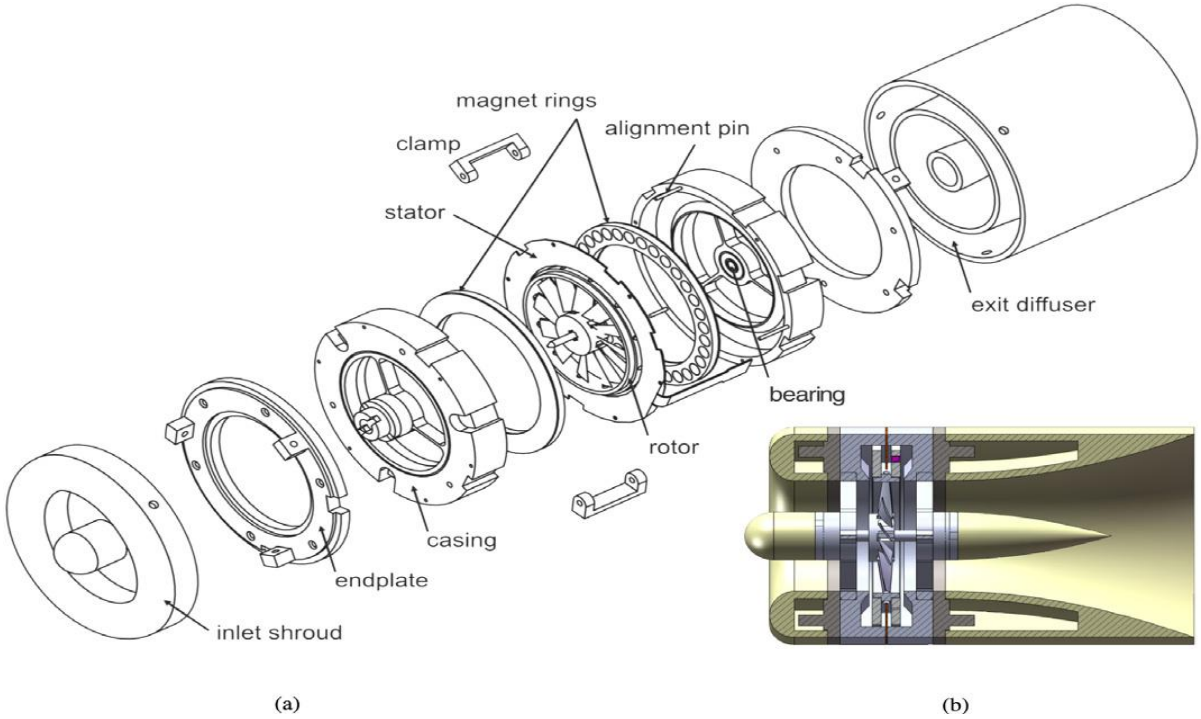

Figure 2-11 Schematic diagram of miniature shrouded wind turbine showing (a) exploded and (b) cut away views [35]

2.3.8 Vortec 7 diffuser augmented wind turbine

The Vortec 7 shown in Figure 2-12 is a fully scaled diffuser augmented wind turbine built by Vortec Energy Limited. The turbine has of blade of 7.3m diameter surrounded by a diffuser. The resulting low pressure in the diffuser draws more air onto the turbine plane, and more power can be generated compared to a bare turbine of the same rotor blade diameter [**42**].

Figure 2-12 The Vortec 7 [42]

2.3.9 Cascaded diffuser wind turbine

This diffuser augmented wind turbine or ducted wind turbine uses a cascading arrangement as shown in Figure 2-13. Using this type of arrangement helps save land space since turbines can be placed closely to one another resulting in an economy of land space usage [**43**]. Two 200W capacity cascaded diffuser augmented wind turbine were tested in a wind tunnel. Results were measured for various cross wind degrees with the distance between the yawing centers of the turbines. Results suggested that when the cross-wind angle was less than 45-degrees, the interference effect was low with very small variation of the power output [**43**].

Figure 2-13 Cascade wind turbine JPS-200 [43]

2.3.10 Rimmed rotor design wind turbine

This rim integrated with blades and rotor in ducts or diffuser has been used from time to time in the history of wind technology [**44**]. The Swift turbine as shown in Figure 2-14 has a diameter of 2m and 1.5kW capacity. The function of the rim is as much to provide a safer, stronger, quieter rotor assembly as it is to enhance aerodynamic performance [**44**].

Figure 2-14 Rimmed rotor deign - Swift 1.5kW [44]

2.4 Mathematical formulations

2.4.1 Power contained in wind

It is known that wind energy provides low quality energy. There is a limit to extracting power from wind. This is shown in Appendix A.

$E \propto v_{\infty}^{3}$ (See Appendix A equation A.2)

The relationships above suggest that a slight change in speed will greatly or substantially change energy.

Considering an area A out of which the wind is flowing through an imaginary disk marked blue with positive and negative pressure before and after the disk simultaneously as shown in Figure A-0-1(see Appendix A). The question is: out of this area how much is the extractable quantity of energy? To calculate this extractable energy Bernoulli derived a set of equations which is described in Appendix A.

2.4.2 Betz theory

Betz's law is a theory about the maximum possible energy that can be derived from a "wind-engine". The Betz law states that wind turbines can never exceed 59.3% efficiency [**45**] [**46**].

Assumptions

The turbine used is a uniform actuator disk which creates a discontinuity of pressure in the stream tube of air flow through it. This analysis uses the following assumptions [**47**]:

- Homogeneous, incompressible, steady state fluid flow;
- No frictional drag;
- The turbine or the machine has an infinite number of blades mounted on the rotor which do not have any drag force resistance with the flowing wind through them;
- Uniform thrust over the disc or rotor area;
- A non-rotating wake; and
- The static pressure far upstream and far down stream of the rotor is equal to undisturbed ambient static pressure. (Refers the Appendix A)

In the case of a thrust operated wind turbine, a rotor disk is experiencing the wind force is receding with the wind. If the disk moves with the wind velocity than the power extracted in this case will be zero and if the rotor disk is stationary then the power output is also zero. So we have to find a value of velocity u of the rotor disk at which power output is maximum see Appendix A.

Force applied by the wind F on the disk results in a change in momentum of the rotor disk and not all wind force is transferred therefore there is a force coefficient C_F. Therefore when the rotor disk recedes with speed u, force is F given by:

$$F = C_F \rho A (v_\infty - u)^2 \qquad \text{(See Appendix A equation A.21)}$$

Power extracted is given by:

$$P = C_F \rho A (v_\infty - u)^2 u \qquad \text{(See Appendix A equation A.22)}$$

The reference power for the Betz efficiency calculation is the power in a moving fluid in a cylinder with cross sectional area A and velocity v and can be expressed as follows:

The power coefficient $C_p = \frac{P}{P_{wind}}$ has a maximum value of:

$$C_p = \frac{16}{27} = 0.593 \qquad \text{(See Appendix A equation A.26)}$$

From the above discussions it is necessary to develop new kind of wind turbine which does not work on the thrust principle. Therefore all new modern turbines work on the aerodynamic principles of lift and drag.

2.4.3 Aerodynamics principles

The aerodynamics of a Horizontal Axis Wind Turbine (HAWT) is not straightforward. The air flow at the blades is not the same as the airflow further away from the turbine. The very nature of the way in which energy is extracted from the air also causes air to be deflected by the turbine. In addition the aerodynamics of a wind turbine at the rotor surface exhibit phenomena that are rarely seen in other aerodynamic fields.

In case of wind turbines, the different forces acting on the blade – namely lift and drag – cause a change in angular momentum which rotates the turbine and exert thrust force (caused by the drag forces). Figure 2-16 shows a blade profile such as 'Angle of attack α' which is the angle at which the relative wind attacks the leading edge of the blade to produce the forces referred to above. The chord is the length of the airfoil; the mean chamber line is the imaginary parabolic line which divides the airfoil in two halves.

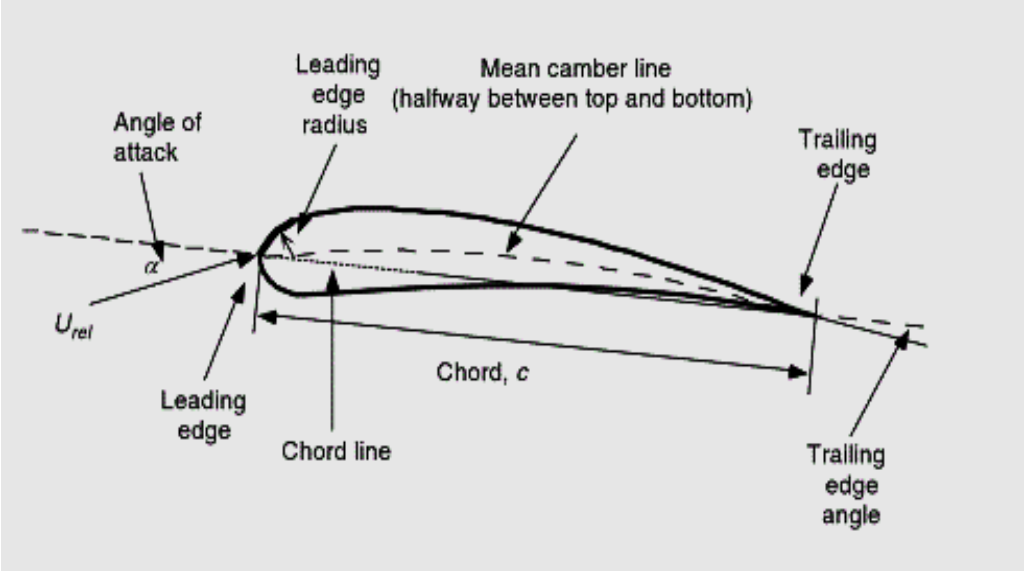

Figure 2-15 Nomenclature of airfoil [49]

Figure 2-17 shows airfoil loading which is necessary to understand in order to design a wind turbine including the vector representation of the various forces acting on the wind turbine blade profile,

Where:

- F_L is the lift force acting on the blade profile;
- F_D is drag force on the airfoil
- F_T is the thrust acting on the profile
- u is linear velocity of the blade;
- v is the wind velocity; and
- w is relative velocity of the wind and blade linear velocity.

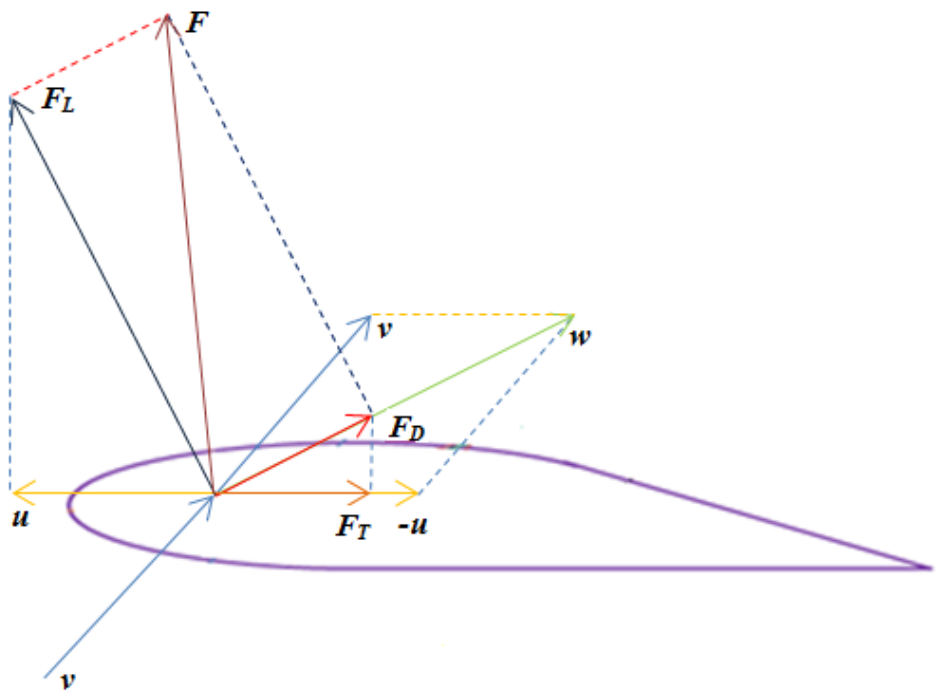

Figure 2-16 Force acting on an airfoil

Figure 2-18 shows a simplified vector illustration for the blade loading. The wind v is almost perpendicular to the plane of rotation, u is velocity of the blade element parallel to the plane of rotation and w is the relative velocity whereas F_L and F_D are corresponding lift and drag forces respectively.

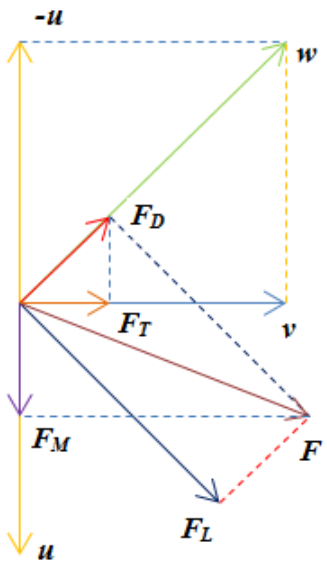

Figure 2-17 Vector representation

Solving the vector equation with reference to Figure 2-18 above:

$$dF_L = \frac{1}{2}\rho\, dA\, w^2\, C_L \quad (2.27)$$

$$dF_D = \frac{1}{2}\rho\, dA\, w^2\, C_D \quad (2.28)$$

$$dF_T = dF_L \cos I + dF_D \sin I \quad (2.29)$$

$$dF_M = dF_L \sin I - dF_D \cos I \quad (2.30)$$

$$dM = r[dF_L \cos I + dF_D \sin I] \quad (2.31)$$

(**Note all the above equations have been derived using Bernoulli's equation and mass flow conservation.)

Other important considerations associated with wind turbine are as follows:

- Tip Speed Ratio (TSR) = $\frac{Speed\ of\ the\ tip}{v_\infty} = \frac{2\pi Rn}{v_\infty}$

where:

R Radius of the tip [m]

n Rotation per second $[\theta/S]$

- Power Coefficient $C_P = \frac{Power\ output\ by\ wind\ turbine}{Power\ contained\ by\ wind\ turbine}$

The Figure 2-19 shows the surge of the power coefficient with TSR Increasing Tip Speed ratio for a fundamental wind turbine according to the above defined relations. The power coefficient always comes to a saturation level after a certain TSR Tip Speed Ratio and Power Coefficient start degrading up to the cutoff wind velocity keeping the safety factor in mind. The Figure 2-20 shows the comparison between different wind turbine how the Power Coefficient changes with different TSR.

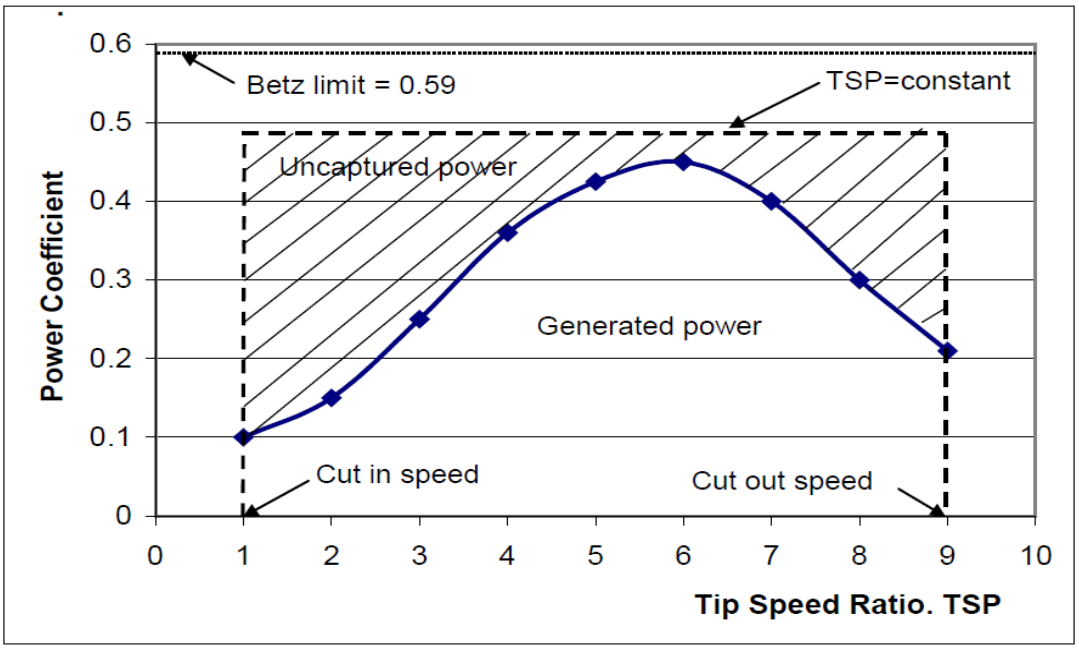

Figure 2-18 Power coefficient as a function of tip speed ratio for a two bladed rotor [50]

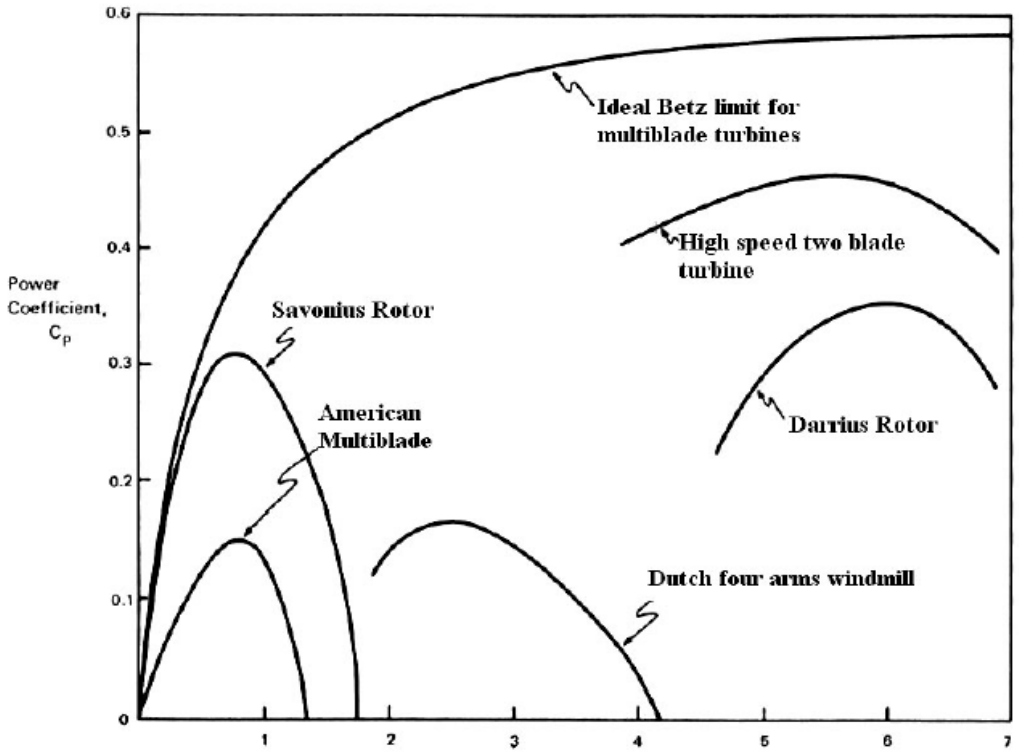

Figure 2-19 Ratio of blade tip speed to wind speed [50]

Important factors to take into consideration while designing the blade of a wind turbine are as follows:

- Taper the blade from inside out because the (u) is less inside and more towards outside;
- Give a twist in the blade (not the pitch angle) so the relative wind (w) parameters balance; and
- Keep the TSR constant since wind speed varies (because C_P is max at specific TSR). Due to this we need to keep on varying the rotation of the blades by changing the pitch of the blade according to the relative speed of the wind.

2.4.4 NACA airfoils

The NACA airfoils are airfoil shapes developed by the National Advisory Committee for Aeronautics (NACA). The NACA airfoils are used to design the blade and the diffuser profile. The shape of an NACA airfoil is described using a series of digits following the word "NACA." The parameters in the numerical code can be entered into equations to precisely generate the cross-section of the airfoil and calculate its properties.

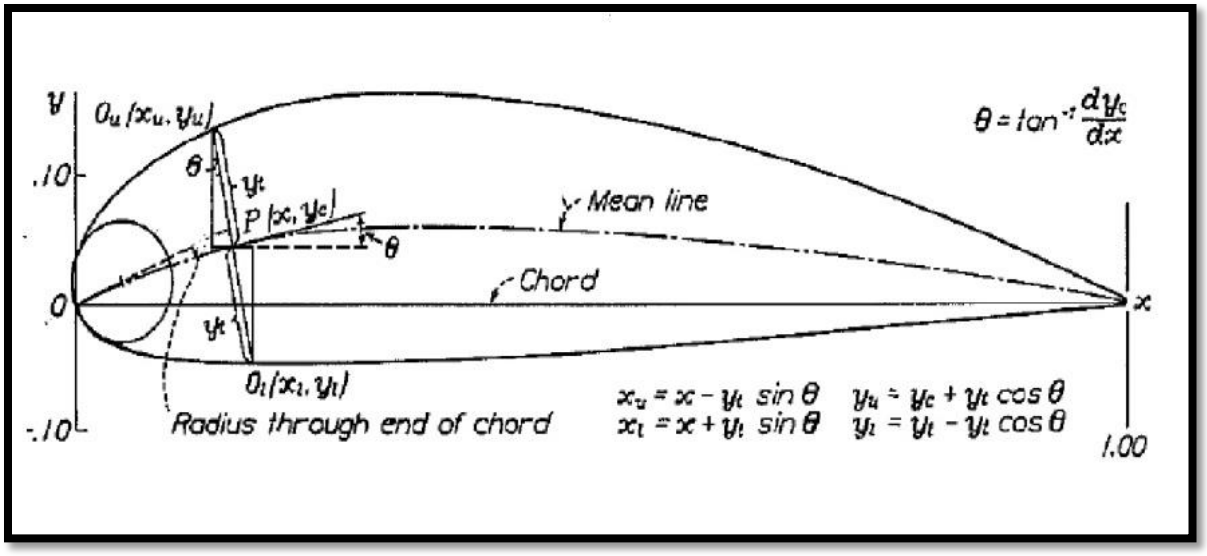

Figure 2-20 NACA airfoil geometry construction [51]

There are two types of NACA series for design of airfoils:

a) NACA 4-digit series airfoils.

These are symmetric airfoils and are designated by a 4-digit number of the form NACA 00xx. The first two digits indicate a symmetric airfoil; the second denotes the thickness-chord ratio. The ordinates for the NACA four digit airfoils family (Refer to Figure 2-21) are described by the following equation [**52**]:

$$\frac{y}{c} = a_0\left(\frac{x}{c}\right)^{1/2} + a_1\left(\frac{x}{c}\right) + a_2\left(\frac{x}{c}\right)^2 + a_3\left(\frac{x}{c}\right)^3 + a_4\left(\frac{x}{c}\right)^4 \qquad (2.33)$$

b) NACA 4-digit-modified series airfoils.

The 4-digit modified series airfoils are designated by a 4-digit number followed by a dash and a 2-digit number (example NACA 0012-63). The first two digits are zero for a symmetrical airfoil and the second two digits indicate the thickness-chord ratio. The first digit after the dash is leading edge-radius index number, and the second is the location of the maximum thickness in tenths of chord aft of the leading edge.

The equation for modified series is given by Ladson [**52**].

$$\frac{y}{c} = d_0 + d_1\left(1 - \frac{x}{c}\right) + d\left(1 - \frac{x}{c}\right)^2 + d_3\left(1 - \frac{x}{c}\right)^3 \quad (2.34)$$

where:

c	Chord length	[m]
x	Position along the chord from 0 to c	[-]
y	Half the thickness at a given value of x (centerline to surface)	[-]
d_n and a_n	Associated constant values	[-]

2.5 Designing of diffuser

The governing principle in fluid dynamics is the conservation law for mass, momentum and energy [**53**]. Designing a diffuser requires the concept of Bernoulli's Equation, and the governing equations of computational fluid dynamics. The governing equations represent mathematical statements of the conservation laws of physics which are as follows [**54**]:

- Mass is conserved for the fluid;
- Newton's second law: the rate of change of momentum equals the sum of forces acting on the fluid; and
- First law of thermodynamics: the rate of change of energy equals the sum of the rate of the heat addition to the fluid and the rate of work done on the fluid.

2.5.1 Bernoulli's Equation

The fundamental advances in fluid dynamics that occurred in the 18th century began with the work of Daniel Bernoulli (1700-1782) [**55**]. The principle states that in a flowing fluid, as the velocity increases, the pressure decreases [**55**].

Bernoulli's Equation is written as follows:

$$\frac{1}{2}\rho v^2 + \rho g z + p = \text{Constant} \quad (2.35)$$

where:

ρ	Density	[kg/m^3]
v	Velocity	[m/s]
g	Acceleration due to gravity	[m/s^2]
z	Height	[m]

2.5.2 Conservation of Mass and Equation of Continuity

The Law of Conservation of Mass states that mass can be neither created nor destroyed [**56**] that the rate of increase of mass within a fixed volume must be equal to the rate of inflow through the boundaries [**57**]. The mass of a moving fluid doesn't change as it flows. This leads to an important quantitative relationship called the continuity equation [**58**]. Common applications where the Equation of Continuity is used is shown in Figure 2-22 representing a mass of moving fluid in a duct with different cross sectional areas A_1 and A_2 with simultaneous flowing fluids or gases of different velocity v_1 and v_2.

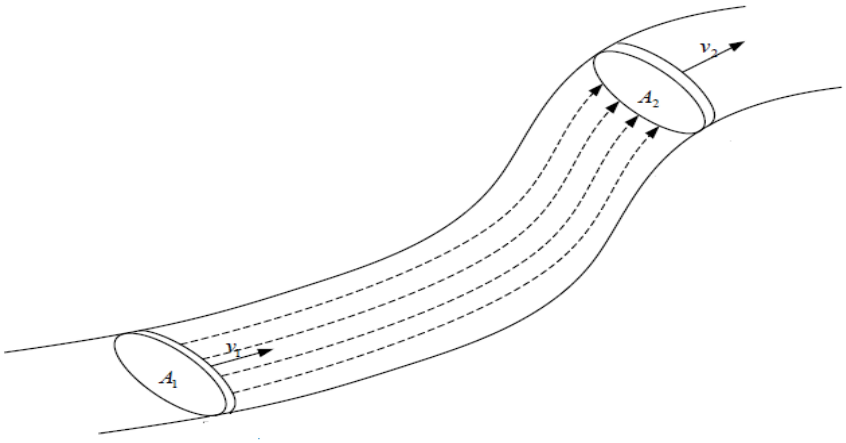

Figure 2-21 Diagrammatic representation of a flow with changing cross sectional area [58]

The Equation of Continuity can be expressed as follows:

$$Q_{in} = Q_{out} \tag{2.36}$$

$$A_1 v_1 = A_2 v_2 \tag{2.37}$$

where:

Q_{in}	Mass flow rate in	[kg/m^3]

Q_{out}	Mass flow rate out	[kg/m^3]
A_1	Area in	[m^2]
A_2	Area out	[m^2]
v_1	Velocity in	[m/s]
v_2	Velocity out	[m/s]

The differential form of the continuity equation is obtained by considering the flow into and out of an elementary control volume of the rectangular Cartesian coordinates system, with coordinates x, y, z measured relative to a stationary frame of reference and the corresponding velocity components u, v, w the continuity equation is [**59**]:

$$\frac{\partial \rho}{\partial t} + \frac{\partial (\rho u)}{\partial x} + \frac{\partial (\rho v)}{\partial y} + \frac{\partial (\rho w)}{\partial z} = 0 \tag{2.38}$$

where:

ρ	Density of the fluid	[kg/m s]
u	Velocity in x direction	[m/s]
v	Velocity in y direction	[m/s]
w	Velocity in z direction	[m/s]
t	Time	[s]

2.5.3 The Conservation of Momentum

The Conservation of Momentum requires that the time rate of change of momentum in a given direction is equal to the sum of forces acting in that direction [**56**]. In addition, according to Newton Second law of Motion, the sum of forces acting on the fluid element equals the product of its mass and acceleration of the element. The three scalar relations along the x, y, z direction of the Cartesian frame for which the fundamental law can invoke [**54**] Newton's second law in the x direction is as follows:

$$\sum F_x = ma_x \tag{2.39}$$

Also acceleration a_x in the x direction and the mass of the fluid element m is given by:

$$a_x = \frac{Du}{Dt} \tag{2.40}$$

and mass m is:

$$m = \rho \Delta x \Delta y \Delta z \tag{2.41}$$

Putting equation (2.40) and (2.41) into equation (2.39) we get the rate of increase of x momentum as:

$$p_x = \rho \frac{Du}{Dt} \Delta x \Delta y \Delta z \tag{2.42}$$

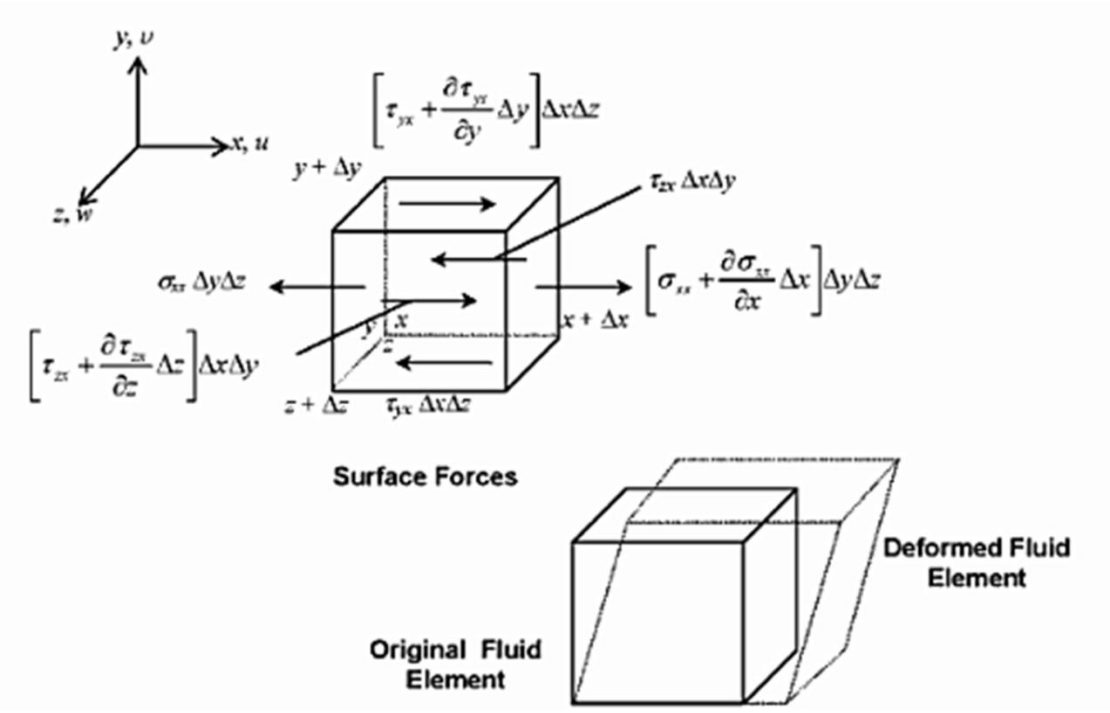

Figure 2-22 Surfaces forces on infinitesimal control volume [54]

As can be seen in Figure 2-23 an infinitesimal small element of fluid is shown with length of Δx breath of Δy and the height of Δz. The surface forces for the velocity component u as shown in Figure (2-22) that deform the fluid element are due to the normal stress σ_{xx} and tangential stress τ_{yx} and τ_{zx} acting on the surface element [**54**]. The x-momentum equation can be written as:

$$\rho \frac{Du}{Dt} = \frac{\partial \sigma_{xx}}{\partial x} + \frac{\partial \tau_{yx}}{\partial y} + \frac{\partial \tau_{zx}}{\partial z} + \sum F_x^{body\ forces} \tag{2.43}$$

Similarly the y-momentum and the z-momentum equation can be written as:

$$\rho \frac{Dv}{Dt} = \frac{\partial \tau_{xy}}{\partial x} + \frac{\partial \sigma_{yy}}{\partial y} + \frac{\partial \tau_{zy}}{\partial z} + \sum F_y^{body\ forces} \tag{2.44}$$

$$\rho \frac{Dw}{Dt} = \frac{\partial \tau_{xz}}{\partial x} + \frac{\partial \tau_{yz}}{\partial y} + \frac{\partial \sigma_{zz}}{\partial z} + \sum F_z^{body\ forces} \tag{2.45}$$

where:

ρ	Density of the fluid	[kg/m^3]
u	Velocity in x direction	[m/s]
v	Velocity in y direction	[m/s]
w	Velocity in z direction	[m/s]
t	Time	[s]
σ	Normal stress	[kg/m s]
τ	Tangential Stress	[kg/m s]

2.5.4 Equation for shrouded/diffuser system

The governing equations are written for a control volume using a cut incorporating the turbine blades (modeled as an actuator-disc discontinuity with zero leakage around its edge (Figure 2-24)) and the duct/shroud (with its attendant force on the flow), along with parallel, constant static pressure inflows and outflows at upstream and downstream infinity [**62**].

2.5.4.1 Power in shrouded wind turbine horizontal axis

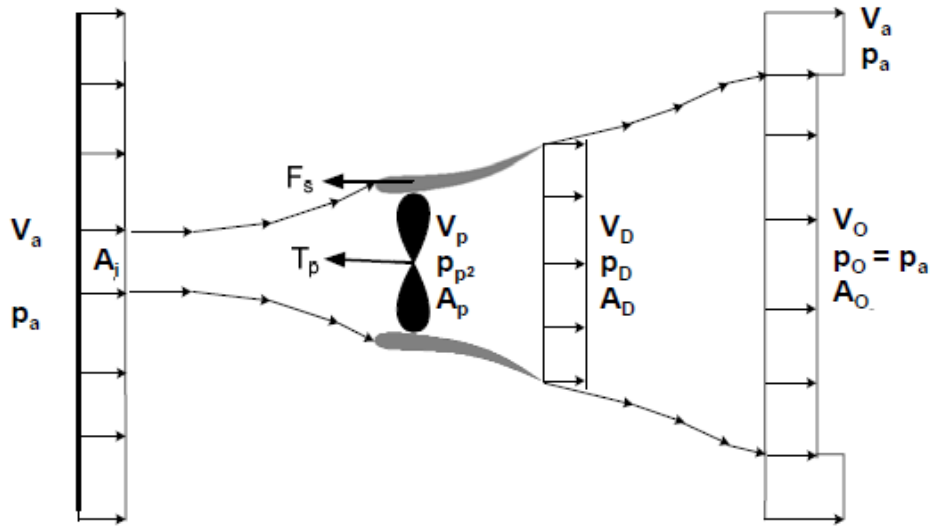

Figure 2-24 Shrouded system nomenclature

Taking into consideration the above conditions, the conservation of mass, momentum and energy for a low speed and/or incompressible fluid lead to the equation for power extracted. The power that can be derived from a shrouded wind turbine as shown in Figure 2-25 can be formulated by using the concept of the pressure jump and can be written as:

$$P = \frac{\left[\frac{1}{2}\rho A_p(V_o^2 - V_a^2) + F_s\right](V_o + V_a)}{2} \qquad (2.46)$$

where:

V_a	Normal Wind velocity	[m/s]
V_o	Velocity behind shroud	[m/s]
F_s	Force on shroud	[kg m/s^2]
p_a	Normal wind Pressure	[kg/m s]
p_p	Pressure inside shroud	[kg/m s]

p_0 Pressure behind shroud [kg/m s]

2.5.4.1 Shrouded force

The axial shroud force F_s in Equation (2.49) can be taken to be directly related to the pressure jump across the disk/turbine through a non-dimensional shroud force coefficient, C_s, and results in the following expression:

$$F_s = \frac{1}{2}[\rho A_p((V_o^2 - V_a^2)]C_s \quad (2.47)$$

where:

C_s Coefficient of shroud [-]

F_s Force on shroud [kg m/s^2]

A_p Area of the shroud inlet [m^2]

ρ Density of air [kg/m^3]

2.5.4.2 Velocity

The resultant internal velocity of the turbine V_p:

$$V_p = \frac{1}{2}(1 + C_s)(V_o + V_a) \quad (2.48)$$

2.5.4.3 Total thrust

The resulting thrust produced on the turbine T:

$$T = \frac{(1+C_s)P}{V_p} = \frac{2P}{(V_o + V_a)} \quad (2.49)$$

Where:

T Thrust on wind turbine [kg m/s^2]

2.4.1.5 The maximum power C_{Pmax}

From Equation (2.51) and (2.52) it is shown that the maximum power that can be extracted by a shrouded wind turbine is given as:

$$C_{Pmax} = -\frac{P}{\left[\frac{1}{2}\rho A_p V_a^3\right]} = \frac{16}{27}[1 + C_s] \tag{2.50}$$

The graph in Figure 2-25 shows the different ratios of wind speed before air enters the shroud and just behind the shroud with respect to air speed inside the shroud.

(**Note that the un-shrouded wind turbine case is recovered using $C_s = 0$).

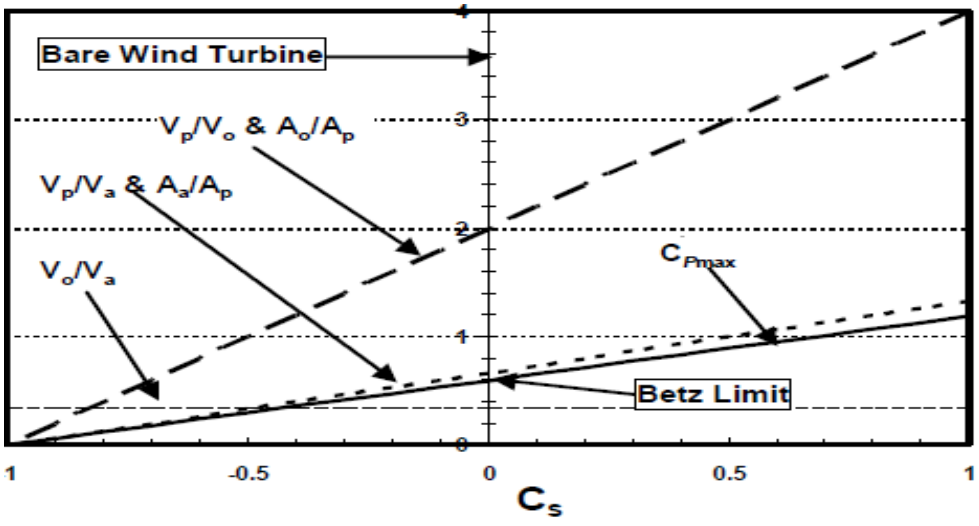

Figure 2-25 Wind turbine max power characteristics

This is shown in Figure 2-26 along with the attendant flow properties given as:

$$V_{oa} \equiv \left(\frac{V_o}{V_a}\right) = \frac{1}{3} \tag{2.51}$$

$$V_{pa} \equiv \left(\frac{V_p}{V_a}\right) = A_{ip} \equiv \left(\frac{A_i}{A_p}\right) = \frac{2}{3}(1 + C_s) \tag{2.52}$$

$$A_{op} \equiv \left(\frac{A_o}{A_p}\right) = \left(\frac{V_{pa}}{V_{oa}}\right) = 2(1 + C_s) \tag{2.53}$$

where:

V_{oa}	Velocity ratio between velocity behind shroud and wind velocity	[-]
V_{pa}	Velocity ratio between velocity at shroud and wind velocity	[-]
A_{op}	Area ratio between exit area and area of the rotor disk	[-]
A_p	Area of rotor disk	[m^2]
A_o	Exit area	[m^2]

The validity and utility of the current formulation can best be demonstrated through comparison with the CFD results of Hansen et al. [**62**] where they present a range of power extraction levels for flow through an actuator disk simulating a pressure drop across a wind/water turbine.

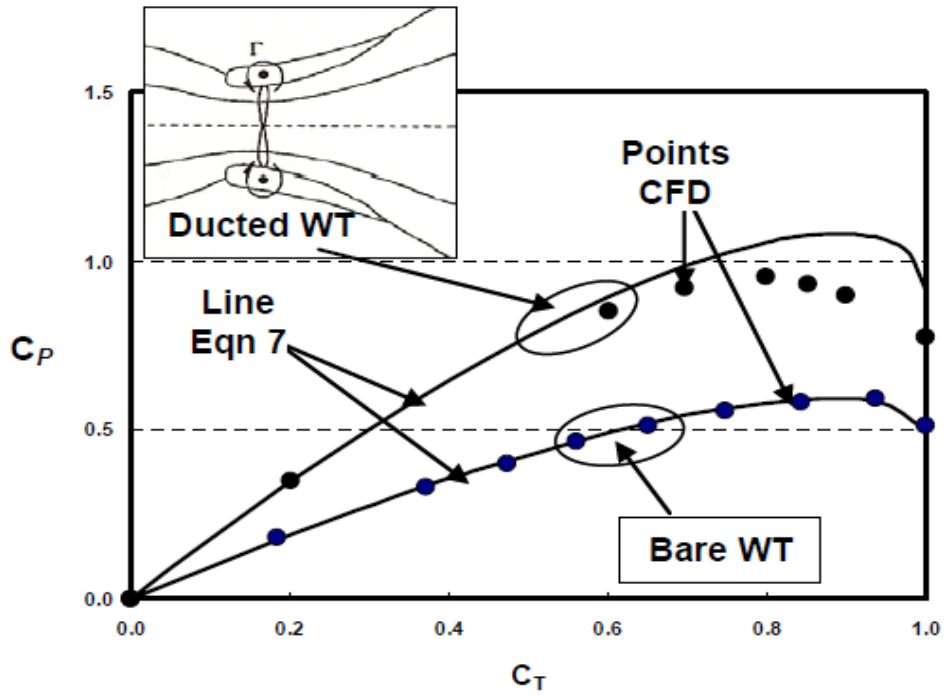

Figure 2-23 Comparison with CFD analysis

Results were presented for an un-ducted case as well as an aerodynamically contoured ducted case with an aggressive exit area ratio: $\frac{A_d}{A_p}$. Figure 2-27 shows the comparison between the bare wind turbine and

the ducted wind turbine. The graph is plotted between the coefficient of performance C_p and coefficient of thrust C_T.

3. RESEARCH DESIGN AND METHODOLOGY

3.1 Introduction

The aim of the study is to upgrade existing shrouded wind turbines to double shrouded wind turbines for higher energy efficiency. We employed a double shroud on existing wind turbines of class IV and class III which operate on very low wind speed. Low wind speed is common in urban areas due to hindrance of mega structures and turbulence due to building and related structures all of which gradually decrease wind speed. This chapter comprises CFD and FEA analysis and simulation of the design with the results optimized for best performance and economic affordability.

3.2 Methodology

The flow chart of the research methodology is shown in the Figure 3-1.

For the solid modeling and designing of the structure of the shroud Autodesk Inventor 2012 was used which is a very robust high end designing software package used by industry.

For the CFD analysis a very high end computing software Star CCM+ 7.02.008 was used which is a very powerful CFD software package used by many researchers and designers to study fluid action and reaction on their prototypes.

The CFD results were used for finite element analysis of the design to optimize the results and to get the final design. Auto Desk Inventor 2012 FEA module and SimXpert 2011 were used for finite element analysis for every single component of the proposed model.

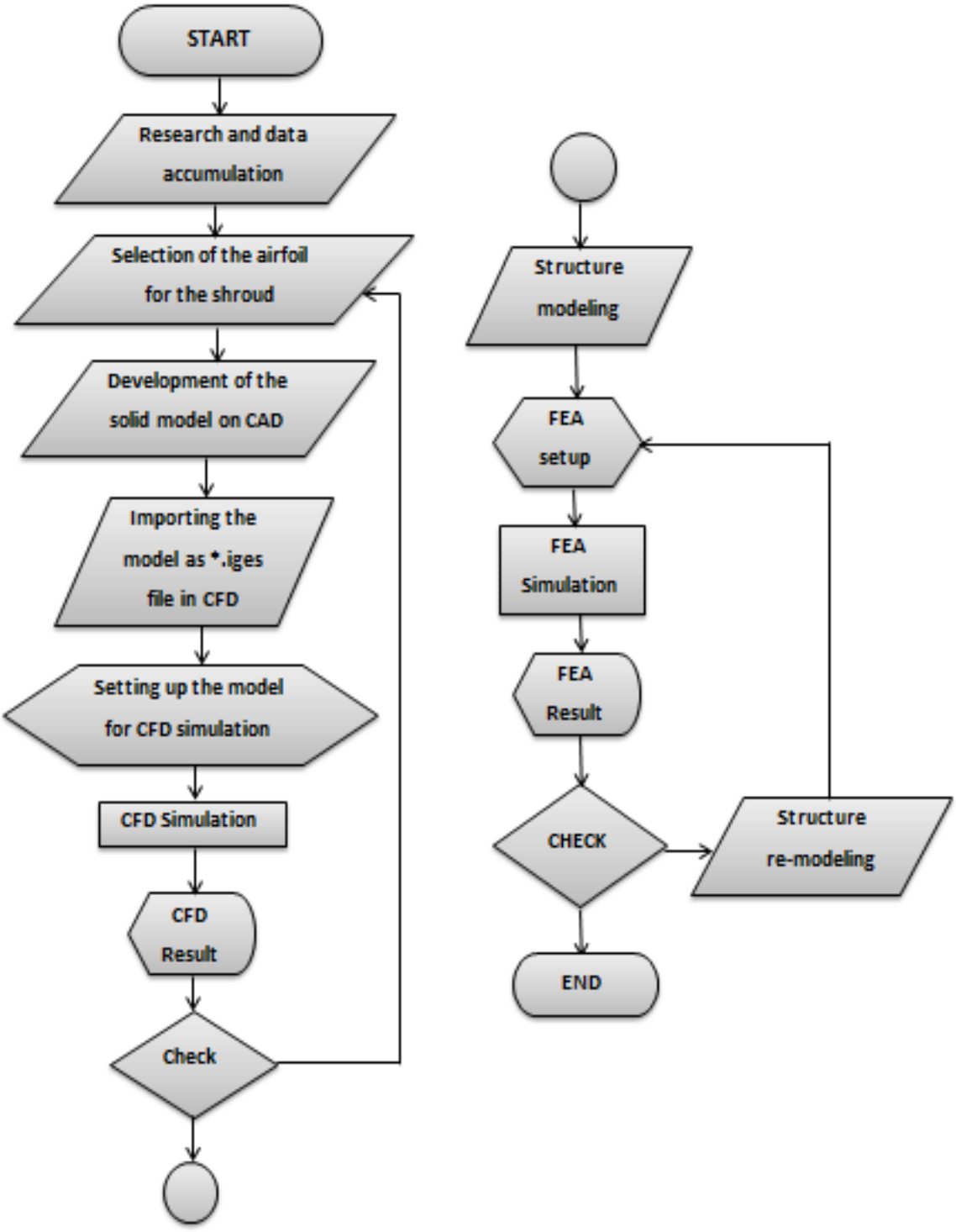

Figure 3-1 Flow chart of research methodology

3.3 Solid modeling of the double shroud

The following procedure was used to create a solid model of the shroud. The airfoil profile x-y coordinates were taken from Group UIUC Applied Aerodynamics [**18**] and were imported into the CAD software as shown in Figure 3-2 then the whole points were selected and rotated at an angle of 10º so that AOA becomes 10º as shown in Figure 3-2.

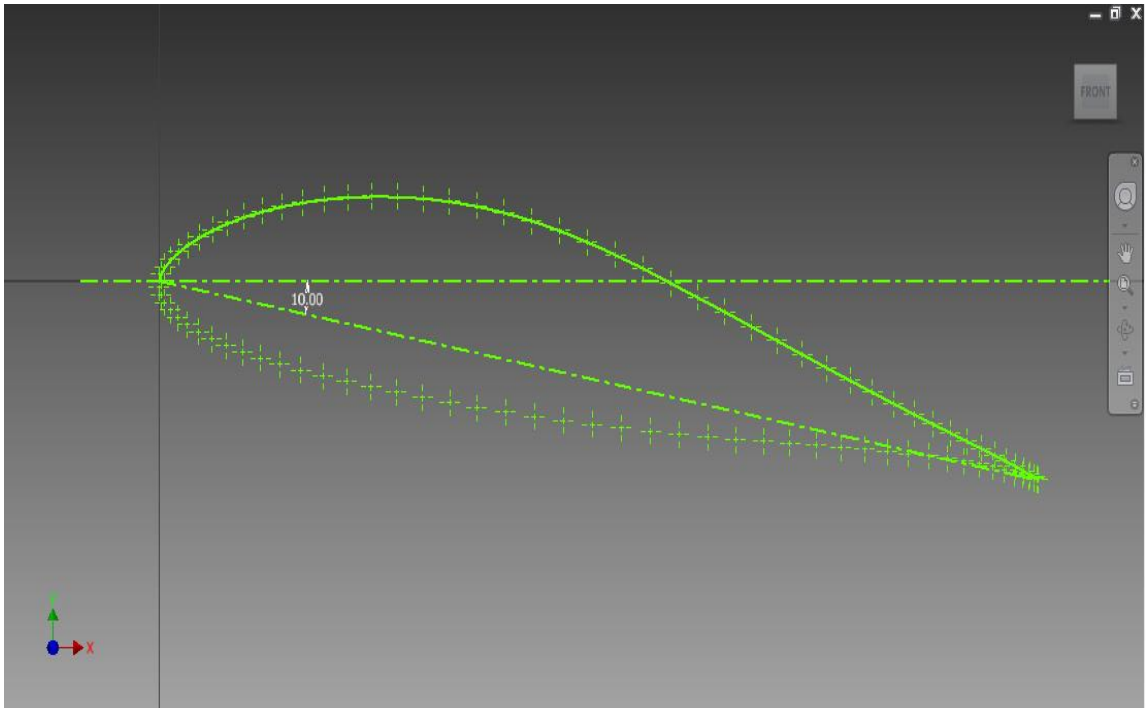

Figure 3-2 Airfoil points imported in Autodesk Inventor

The whole profile is then scaled to 3 times the original size and a new profile is mirrored across the mirror line to form the upper shroud as shown in Figure 3-3. The points above the chord line in the upper shroud are shredded in order to make the structure lighter since it plays no role in the design. A flanged end is added to the design.

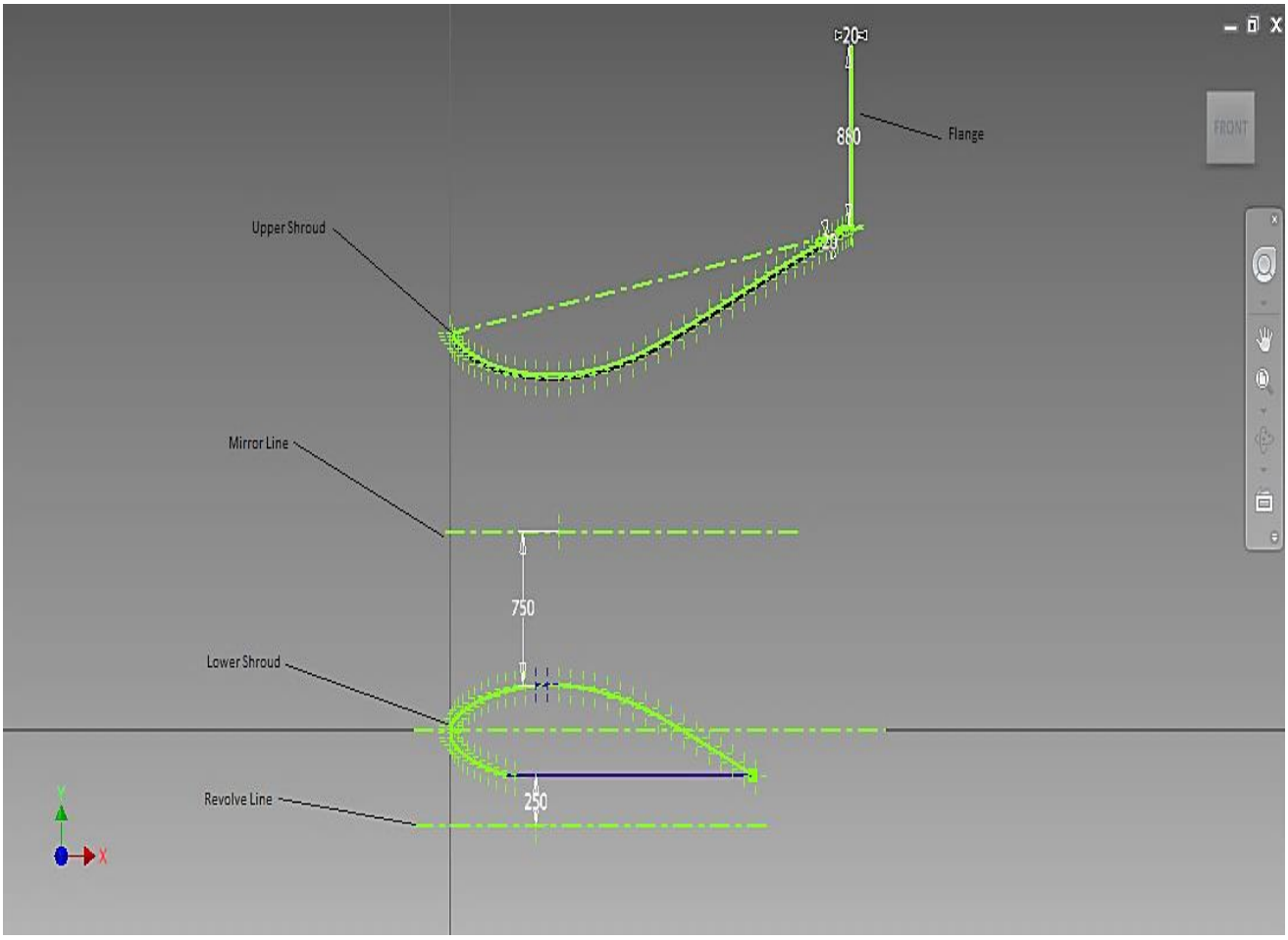

Figure 3-3 Shredded points of airfoil all dimensions are in mm

The whole closed profile is then revolved around the center line as shown in Figure 3-4 to make a complete solid model using the revolve extrude tool and also to accommodate a rotor of effective diameter of 3m. Figure 3-4 (a) shows the half revolved solid shroud and Figure 3-4 (b) shows the full revolved solid shroud. In this, the inner shroud, the upper shroud and the flanged end are all revolved simultaneously for the ease of the creation of the IGES model which is then later on required for the CFD simulation and analysis. The revolve line is 250mm distanced from the base line of the lower shroud and the mirror line is 750mm distanced from the lower shroud crest point. The flange is 880mm long and 20mm thick. The upper shroud thickness is kept to 20mm in order to keep the design light. An *.iges file is created so that the model can be examined for the computational fluid dynamics in the CFD software Star CCM+ 7.03.008.

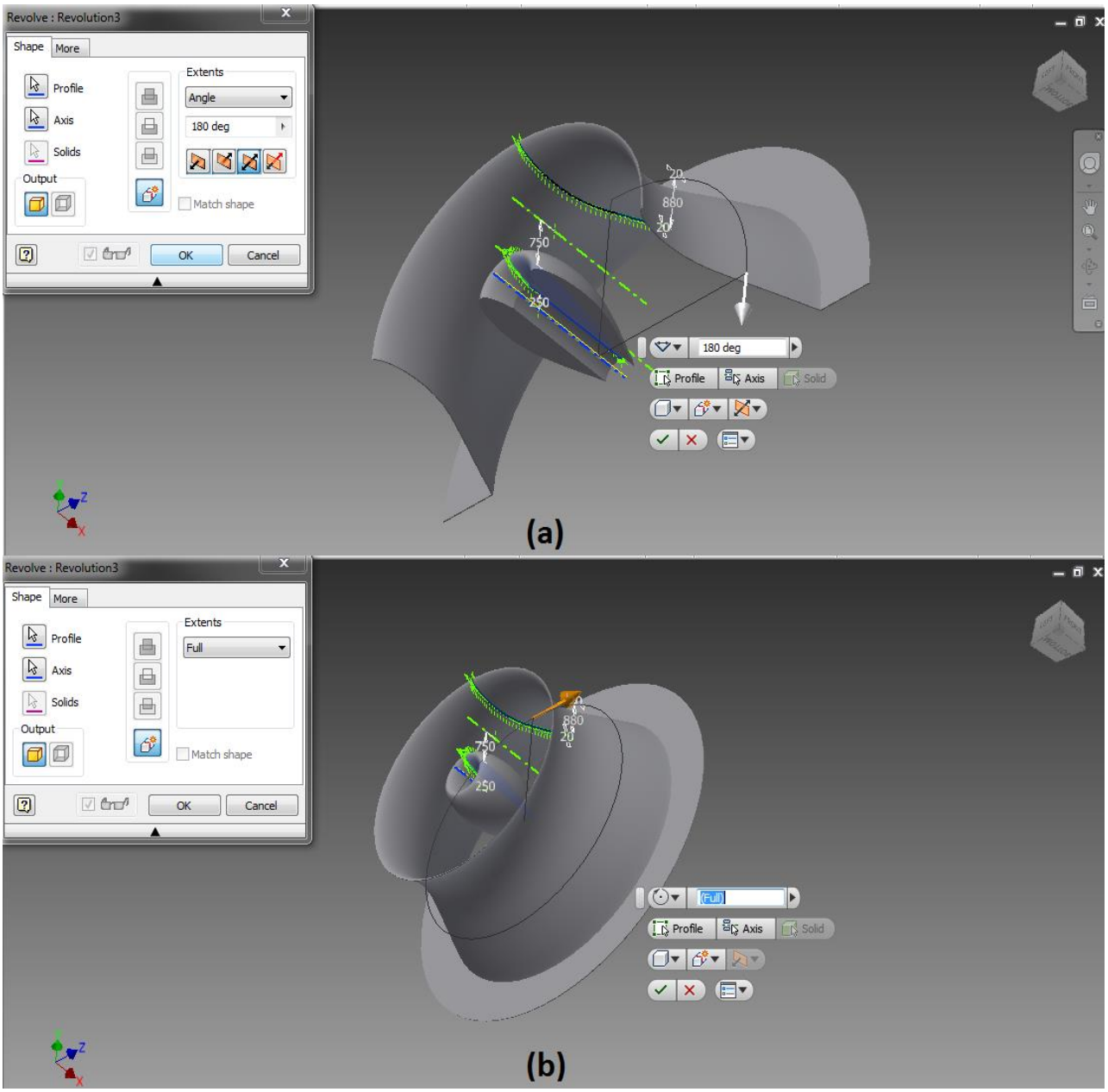

Figure 3-4 Revolved extrution of the airfoil (a) half revolved (b) full revolved

3.4 Computational Fluid Dynamics CFD

Fluid dynamics is the science of fluid in motion and is commonly studied in one of the following three ways:

- Experimental fluid dynamics;
- Theoretical fluid dynamics; and
- Numerically or Computational fluid dynamics.

The computational method works under the following principles and techniques:

- Analysis begins with a mathematical model of a physical problem;
- Conservation of matter, momentum, and energy must be satisfied throughout the region of interest;
- Fluid properties are modeled empirically;
- Simplified assumptions are made in order to make the problem tractable (e.g., steady-state, incompressible, in-viscid, and two-dimensional);
- Appropriate initial and boundary conditions for the problem are provided;
- CFD numerical methods (called discretization) are applied to develop approximations of the governing equations of fluid mechanics in the fluid region of interest; and
- The solution is post-processed to extract quantities of interest (e.g. velocity, pressure, shear forces on the surfaces etc.).

The flow chart in Figure 3-5 describes the process of the CFD simulation.

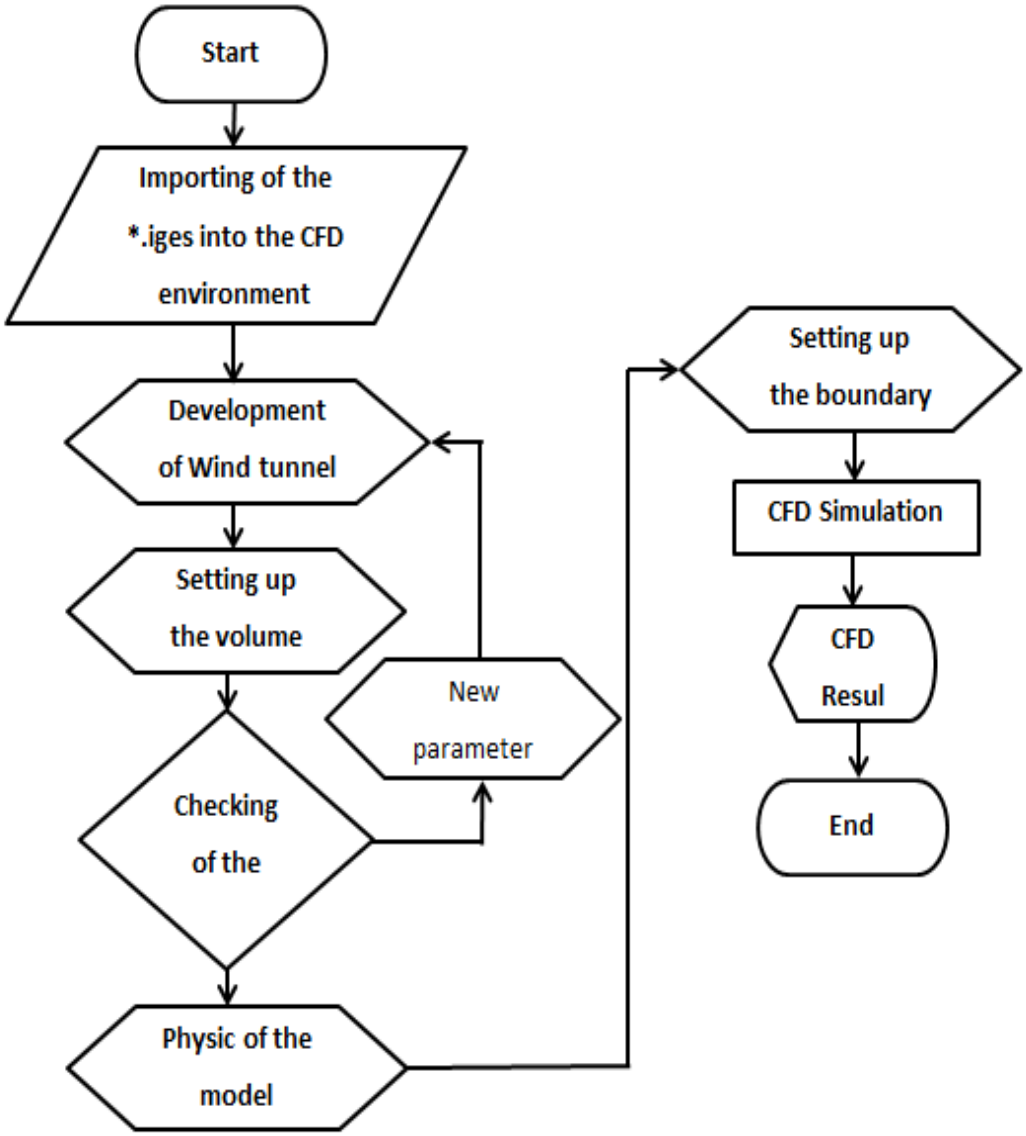

Figure 3-5 Flow chart of CFD analysis

3.4.1 Simulation of model

In order to simulate the increased wind speed of the wind inside the shrouded domain where the wind turbine blades rotate, a wind tunnel is created around the shroud as shown in Figure 3-6. The dimension of the tunnel is 80m length 70m width and 65m height. The wind tunnel is large enough to simulate a real time wind test on the shroud. The model is placed 35m from the air inlet and 45m from the pressure outlet.

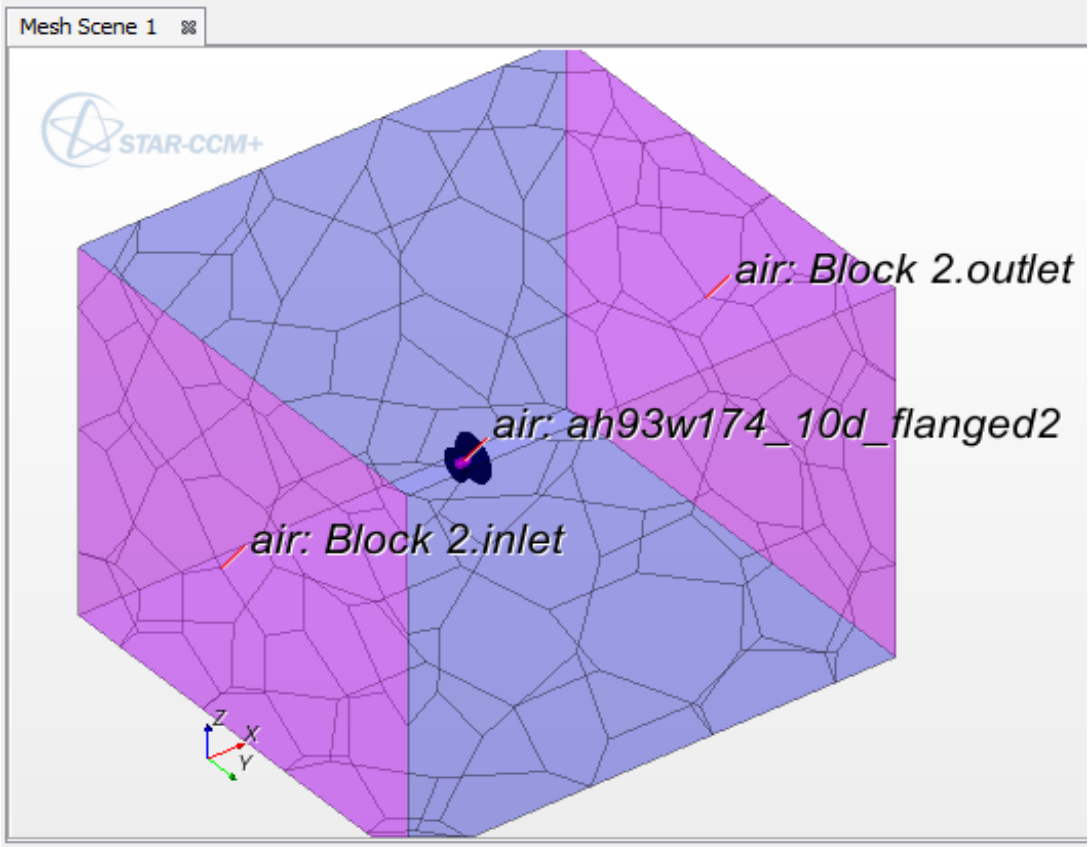

Figure 3-6 Wind tunnel testing with three dimensional volume meshes

3.4.2 Meshing of the model

The solid model which was created using Autodesk® Inventor® 2012 was then imported into Star CCM+ as an *.iges file. Due to poor surface quality and triangulation in the imported mesh, the model was re-meshed since high accuracy is required in the closed vicinity around the shroud. These regions and surfaces were meshed using the finest mesh parameters in the model as shown in Figure 3-6.

A base value of 10m was used for the global mesh base size for the wind tunnel of the double shroud, 0.5m size for the shroud region and 0.045m for the shroud surfaces. The shroud surfaces required an extremely fine mesh size to capture the geometry of the shroud surfaces accurately. In order to control these, volumetric controls were used as shown in Table 3-1. This volumetric control tool allows us to control the selected volume in order to save time and computing memory.

Table 3-1 Volumetric control

Volumetric control	Region	Absolute Value
1	Upper Shroud	0.045mm
2	Lower shroud	0.045mm
3	Block Region (control region)	0.5m
4	Wind Tunnel Region (global mesh)	10m

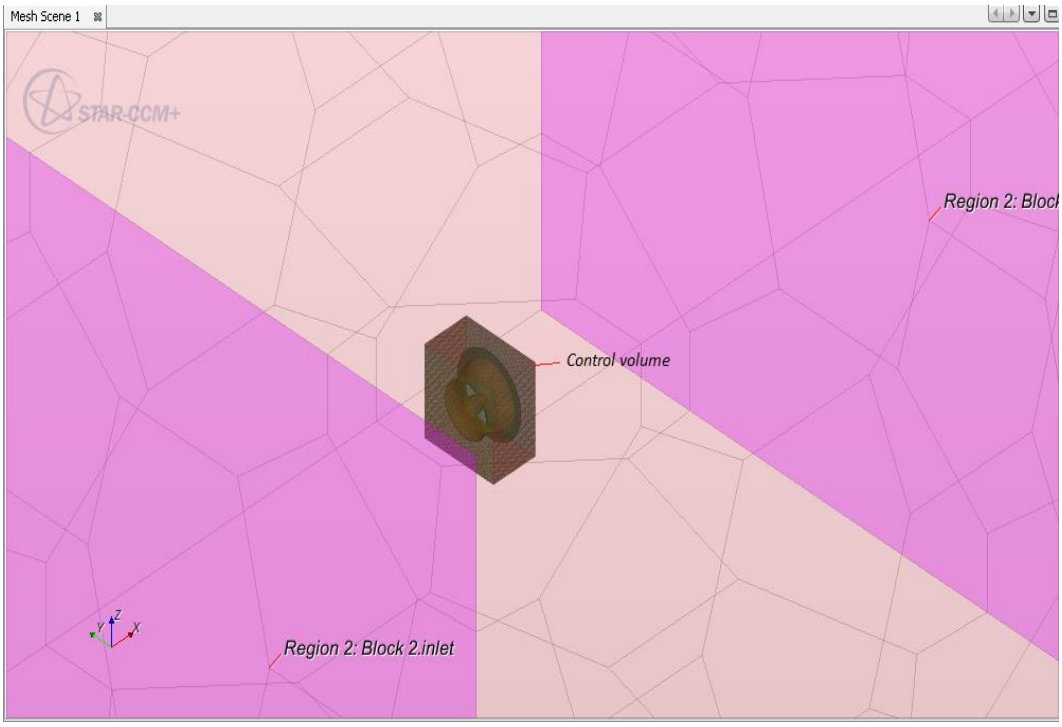

Figure 3-7 Illustration of volumetric control

To develop surface mesh and volume mesh, surface re-mesher was used together with polyhedral mesher for the modal. The following parameters were applied as shown in Table 3-2 to both the volume and surface mesh. An image of the volumetric control is shown in Figure 3-7.

Table 3-2 Reference mesh values

Parameter	Settings
Base Size	10m
Surface Curvature	36pts/circle
Surface growth rate	1.3
Surface proximity	4 points in gap
Tet/poly density & Tet/poly volume blending factor	1

As per the label of Figure 3-8 shows (a) the volume meshed and (b) the surface re-meshed. This surface mesh was used along with polyhedral mesher to create both the surface and the volume mesh for the model as shown in the figure.

Figure 3-8 Illustration of the (a) volume meshed and (b) surface re-meshed

3.4.3 Physics of the model used in the simulation

Defining the physics of the model is done when the mesh produced is satisfactory. This definition provides the real time conditions to which the model will be subjected. The following are the conditions:

- Since the geometry of the model is in space, three dimensional models are selected for the space model;
- The material selected for the continuum is air as has ideal gas properties and behavior;
- Since the simulation is done on a low Mach number and with a slight compressibility effect, a segregated solution method is used;
- Turbulence effect is modeled using *k*-ε turbulence, with following parameters; and
- The Reynolds Averaged Navier Strokes (RANS) model is also selected to model the effects of turbulent fluctuation on the mean flow.

Table 3-3 Turbulence parameter

Parameter	**Settings**
Turbulence specification	Intensity + viscosity ratio
Turbulence intensity	0.01
Turbulence viscosity ratio	10
Turbulence velocity scale	1.0 m/s

The successful analysis of the model requires the calculation of the set of appropriate turbulence values as shown in Table 3-3 for the inflow boundary conditions. The turbulence intensity is defined as the ratio of the root-mean-square of the velocity fluctuation to the mean stream velocity whereas the turbulent viscosity ratio is simply defined as the ratio of turbulent to laminar (molecular) viscosity [**63**].

3.4.4 Boundary conditions

The boundary condition and the initial condition are applied to the model so simulation can be set up correctly. Figure 3-9 shows the boundary condition of the model. The boundary conditions were specified as follows:

- The front of the wind tunnel is specified as the velocity inlet;
- The rear portion of the wind tunnel is specified as the pressure outlet; and
- Boundary walls are set as the wall of the wind tunnel.

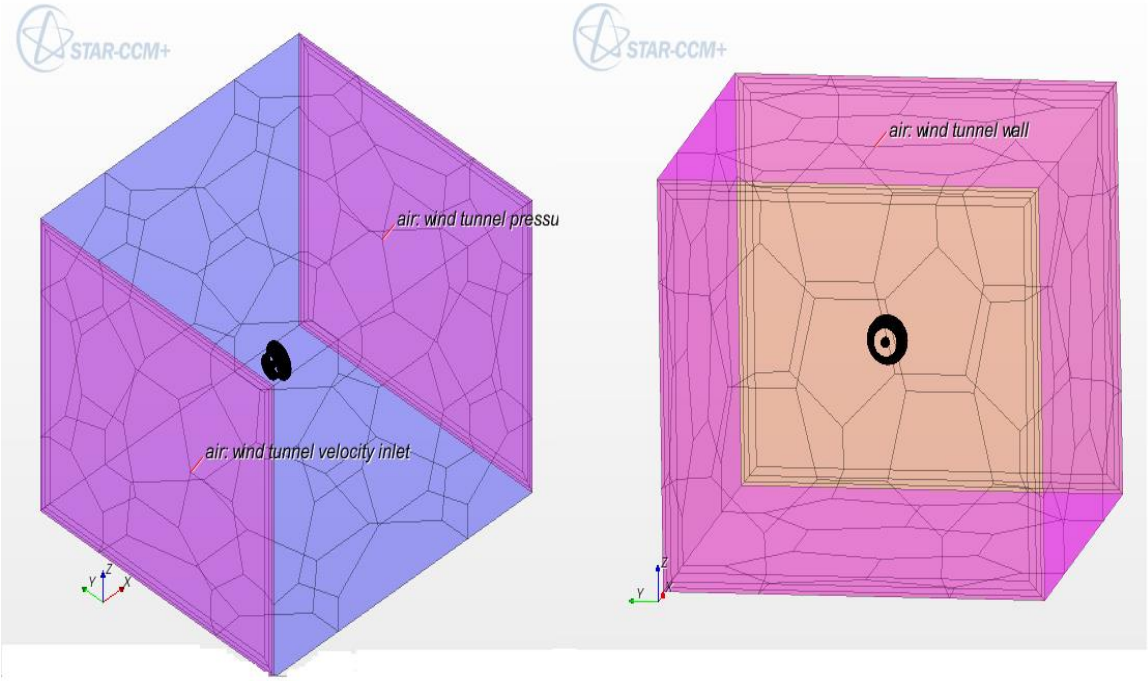

Figure 3-9 Boundary condition of the model

3.5 Structure modeling on CAD

The results obtained from the CFD simulation were studied and analyzed properly in order to prepare a structural model on CAD software. With the help of CAD software every single component was designed properly keeping the following things in mind:

- Weight optimization;
- Safety factor;
- Easy construction and fabrication of the parts; and
- Economic feasibility

3.5.1 Development of the upper shroud

The upper shroud forms the outer shroud of the design. Development of the upper shroud is done by importing the coordinates of the **"ah93w174"** airfoil point in the sketch environment of the inventor part modeling and then shredding the points above the chord line to reduce the weight of the part. The flange is also incorporated in the design.

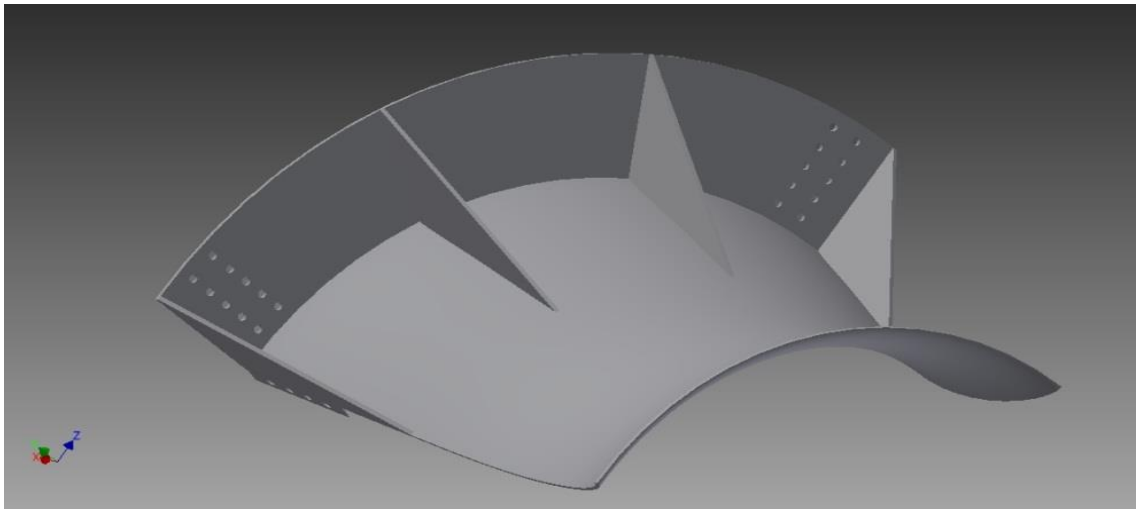

Figure 3-10 Segment of the upper shroud

The center line of the extrusion is sketched to revolve the whole profile of the upper shroud 90º for the ease of fabrication on the shop floor (Figure 3-10). Ribs are added for additional strength. The holes were made on the flanges as shown in the figure for assembly purposes and to add bracing to hold the whole shroud weight. The brackets is added so that the lower shroud can be connected to the upper shroud with the help of the inside cross bracing.

The physical properties of the outer shroud are described in Table 3-4.

Table 3-4 Physical properties of the outer shroud

Material	**SAN Plastic**
Density	1.068g/cm^3
Mass	402.116kg
Area	37.089m^2
Volume	0.37m^3
Centre of Gravity	x=2.176725m y=6.11315×10^{-1}m z=1.697612m

3.5.2 Development of the lower shroud

The lower shroud forms the lower part of the design. This lower part is divided into two with a front part and rear part. The front part is integrated with the hub of the wind turbine as shown in the Figure 3-11. The procedure of developing this part is the same as the procedure for developing the outer shroud. The points are imported in the sketch environment of the part modeling and then the excess points are deleted to reduce the total weight of the part. The whole profile is revolved around the center line to get the desired part model. The hub forms the core of the front part of the inner shroud which is then solidly connected to the shroud with the help of ribs.

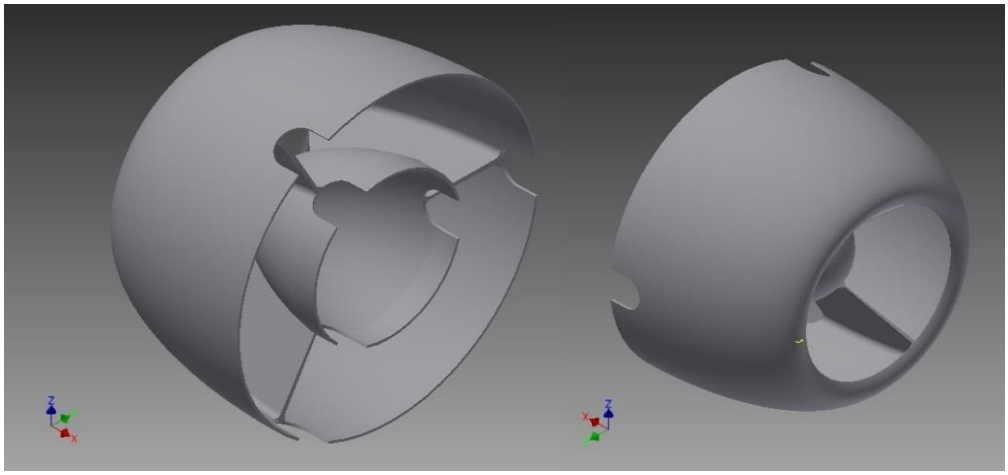

Figure 3-11 Integrated front and hub

The physical properties of the hub are described in Table 3-5.

Table 3-5 Physical properties of the hub

Material	**SAN Plastic**
Density	1.068g/cm^3
Mass	39.949kg
Area	9.17m^2
Volume	0.037m^3
Centre of Gravity	x=0.388833m y=-0.436418m z=1.0×10^{-6} m

The rear part of the inner shroud is designed using the same procedure as for designing the outer shroud and the front part of the inner shroud. As can be seen in Figure 3-12, bracing is added to hold the part in place and inside cross bracing and ribs are added to make it structurally stronger and more stable.

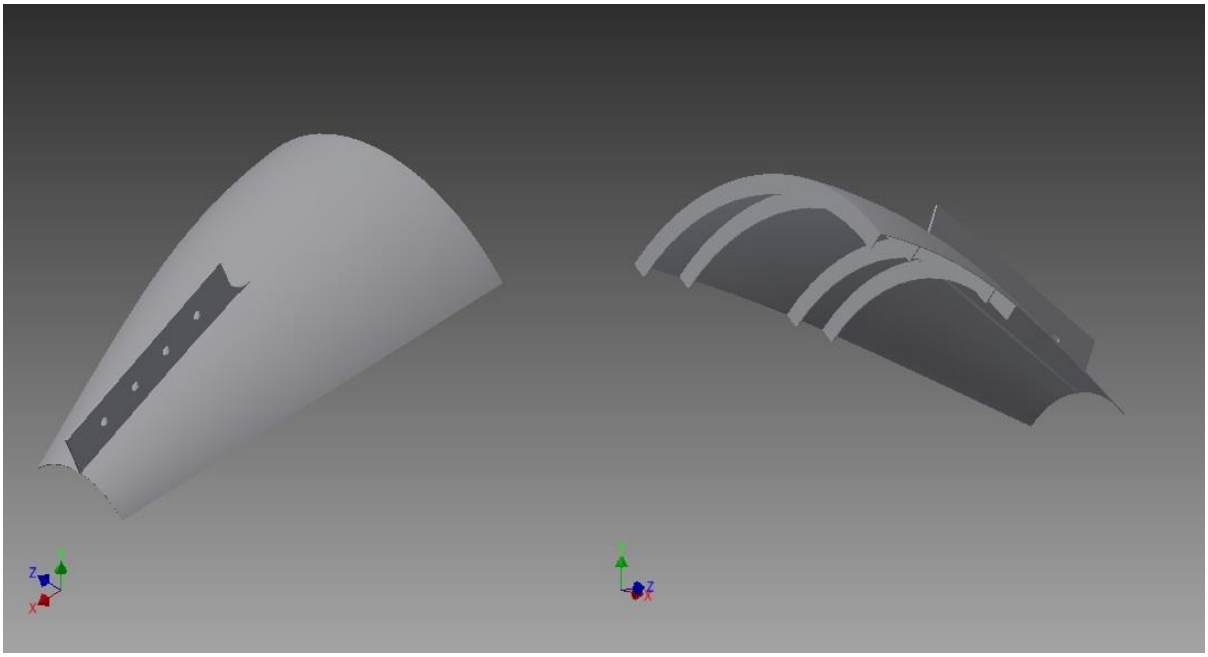

Figure 3-12 Shroud rear part

The physical properties of the inner shroud rear part are described in Table 3-6.

Table 3-6 Physical properties of the shroud rear part

Material	**SAN Plastic**
Density	1.068g/cm^3
Mass	4.694kg
Area	2.709m^2
Volume	0.0043m^3
Centre of Gravity	x=1.448371m y=-3.9796×10^{-2}m z=1.48×10^{-4}m

3.5.3 Hold-down arms (truss bracing)

Four hold-down arms are truss bracing which hold the outer and the inner shroud in the assembled formation. These also play the vital role of carrying the load of the whole shroud structure and the wind turbine as shown in Figure 3-13. These arms are designed so that they can withstand the drag and thrust forces created by strong hurricane winds. The truss design is utilized to lower the effective weight of the arms keeping economic feasibility in mind but without compromising safety.

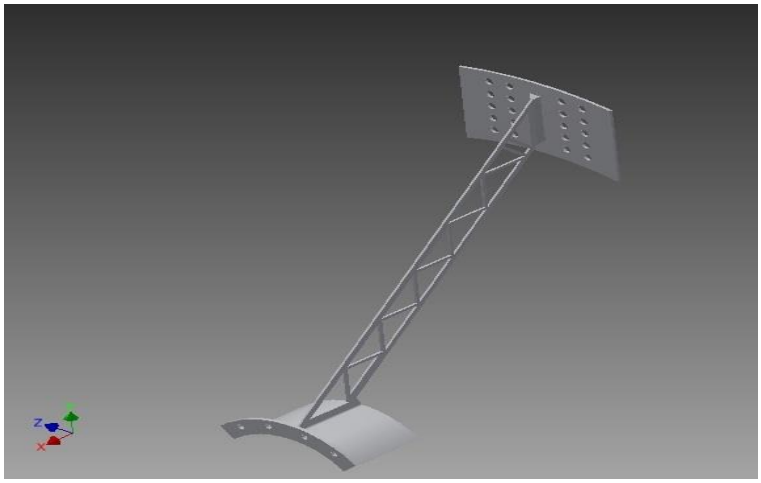

Figure 3-13 Hold-down arms

The physical properties of the hold-down arm are described in Table 3-7.

Table 3-7 Physical properties of hold-down arms

Material	**Aluminium 6061**
Density	2.71g/cm^3
Mass	201.45kg
Area	6.69m^2
Volume	0.0743m^3
Centre of Gravity	x=5.69044×10^{-1}m y=2.01117m z=6.7301×10^{-10}m

3.5.4 Inside cross bracing (connector bracing)

This inside cross bracing (also known as connector bracing) is shown in Figure 3-14 and is used in the design to connect the inner shroud to the outer shroud. This also uses a truss design in order to hold the weight of the inner shroud and also withstand the drag and the thrust forces developed by the wind. The truss design also helps to keep the bracing in shape without deforming and keeps the whole assembly intact.

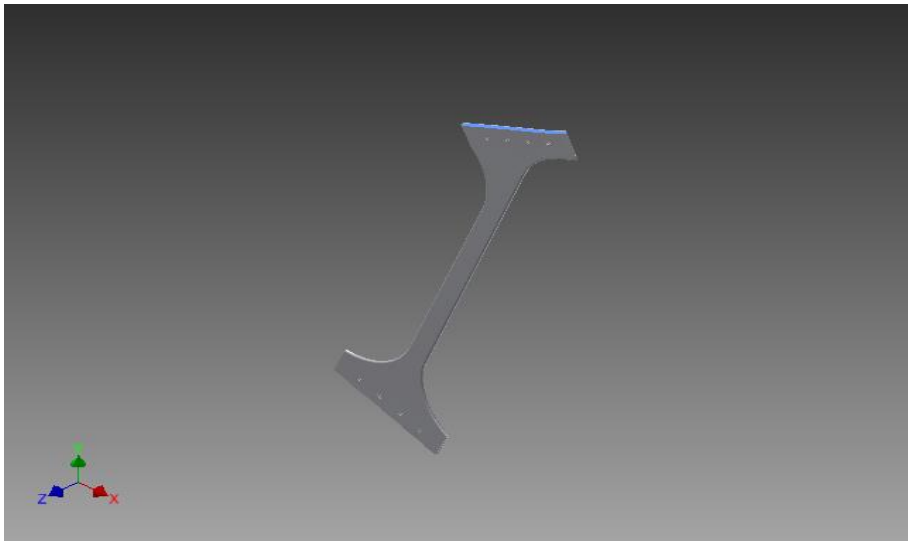

Figure 3-14 Inside cross bracing

The physical properties of the cross bracing described in Table 3-8.

Table 3-8 Physical properties of cross bracing

Material	**Aluminium 6061**
Density	2.71g/cm^3
Mass	27.0312kg
Area	1.69m^2
Volume	0.0099m^3
Centre of Gravity	x=2.39699m y=3.8603×10^{-1}m z=2.35194×10^{-6}m

3.5.5 Nacelle

The nacelle is one of the main components of the wind turbine and holds the AC generator, gear box and other instruments which are vital in the conversion of wind energy. The nacelle is shown in Figure 3-15.

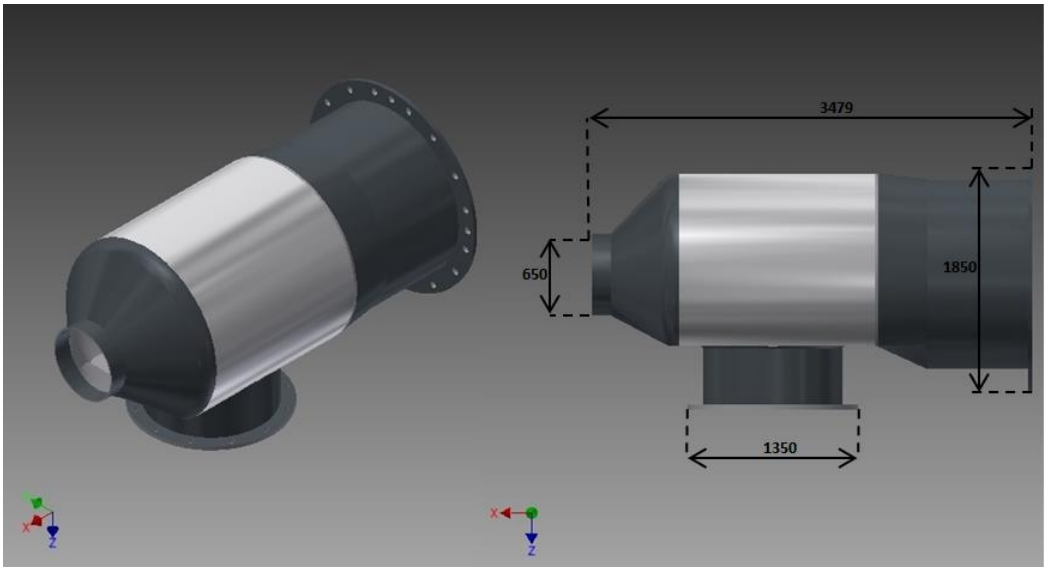

Figure 3-15 Nacelle all dimensions are in mm

3.5.6 Tower

The tower as shown in Figure 3-16 is another important part of the wind turbine. The tower must be strong enough to hold all the components of the wind turbine in position above the ground and designed in such a way that it can bear the vertical load of the components due to gravity and the horizontal load

due to the drag and thrust of the turbine and shroud. The tower consists of the two base plates joined together with the help of ribs to provide a rigid support at base level. A pipe made of mild steel forms the stem and top flange to connect the nacelle. A solid concrete structure is made into which the pole is grouted with the help of foundation bolts.

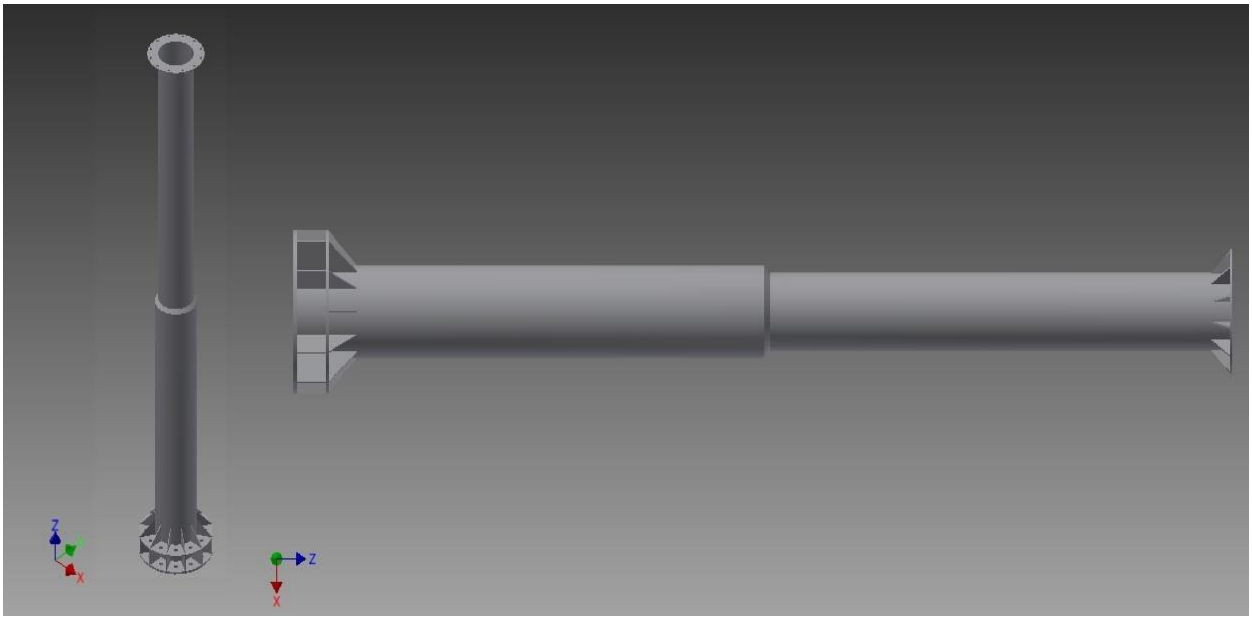

Figure 3-16 Tower

3.6 Finite element modeling

A number of methods have been adopted in the engineering field for the analysis of solid structures among which numerical simulation techniques have been developed including the finite element method (FEM), the finite difference method (FDM) and the recently developed mesh free method [**64**]. The FEM is enabling remarkable developments in fluid and large surface structure interactions like ship hydrodynamics, off-shore structures, dam spillways [**65**], designing and development of motor vehicle tires [**66**] and recently finite element analysis (FEA) is playing a vital role in the field of knee arthroplasty [**67**].

3.6.1 Introduction

In this study, FEA was used to ensure structural stability and strength without compromising safety; keep weight as low as possible so that projects are economically viable, and; to analyze the dynamic behavior

of the shroud under different loads and pressure. FEA provides various advantages including design of a more reliable system and helping to save time and money.

3.6.2 Background of finite element modeling

This method is the most efficient way of analyzing the shroud and is most widely used in the wind turbine and aircraft industry. This method was originally developed by the engineers ad researchers in order to analyze aircraft wings. In this method the structural domain is broken into a series of smaller regions called elements in which the governing partial differential equation of each element is solved. All the elements are interconnected via nodes.

There are various computer software packages available to industry providing FEM capability to engineers, including MSC NASTRAN, ADINA, ANSYS, SIMULIA, Autodesk Inventor etc.

3.6.3 Process overview

The FEM process starts with designing of the part in the CAD environment and then importing it to the FEA environment. The simulation starts with assigning of material to the part after which the constraints are added to make the model fixed in all directions. After adding the constraints, loads are applied to the model which can be pressure, forces, bearing load, moment and gravity. Then mesh is generated to subject the model to finite elements and nodes. After the mesh has been checked the simulation is started otherwise the parameters of the mesh are changed to obtain the right mesh configuration. The flow chart in Figure 3-17 shows the synopsis of the procedure for the FEA of the shroud and other components.

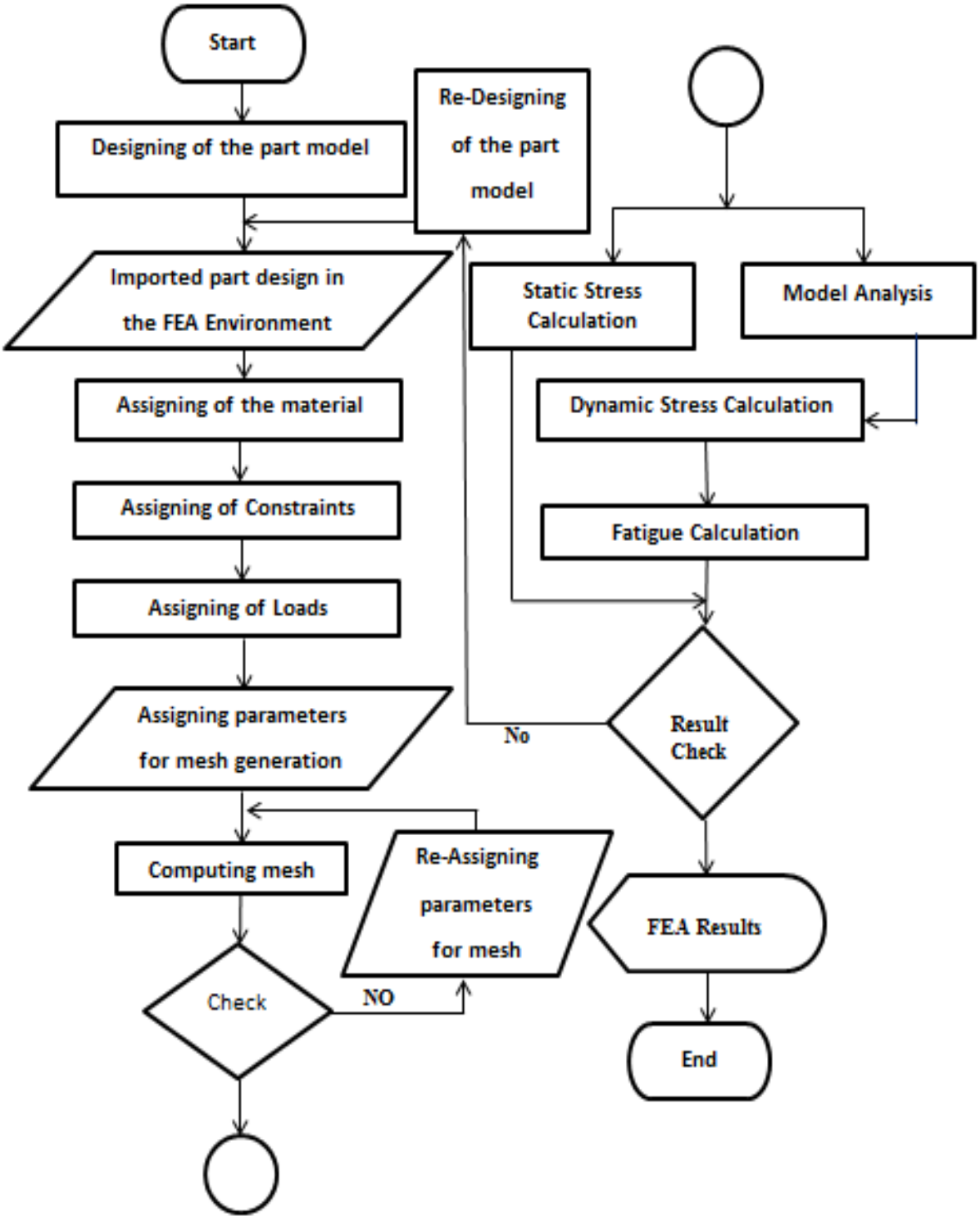

Figure 3-17 Flow chart of FEA analysis

3.6.4 Setting up the model

This section discusses the results of the FEA which were collected after the FEA simulation. The results will be discussed with the help of the following points:

- General design objective and settings which define the single point dimensioning or parametric dimensioning;
- Mesh setting which constitutes average element size, minimum element size, grading factor and max turn angle; and
- Design constraints which concentrate on optimizing weight within the safety factor.

It is difficult to analyze the whole assembly at once since every single component requires its own mesh parameters and generalizing the global mesh parameters for all parts would have taken too much computing time and memory, therefore in this study every single part was analyzed individually.

3.6.4.1 FEA model setup of the outer shroud

The parametric design objective was selected and the static analysis for the simulation type was designated. Fixed constraint type was selected as shown in Figure 3-18 with blue color. Mesh settings of the outer shroud are given in Table 3-9.

Table 3-9 Mesh setting of outer shroud

Average Element Size (fraction of model diameter)	0.8
Minimum Element Size (fraction of average size)	0.08
Grading Factor	1.5
Maximum Turn Angle	60^{O}
Create Curved Mesh Elements	Yes

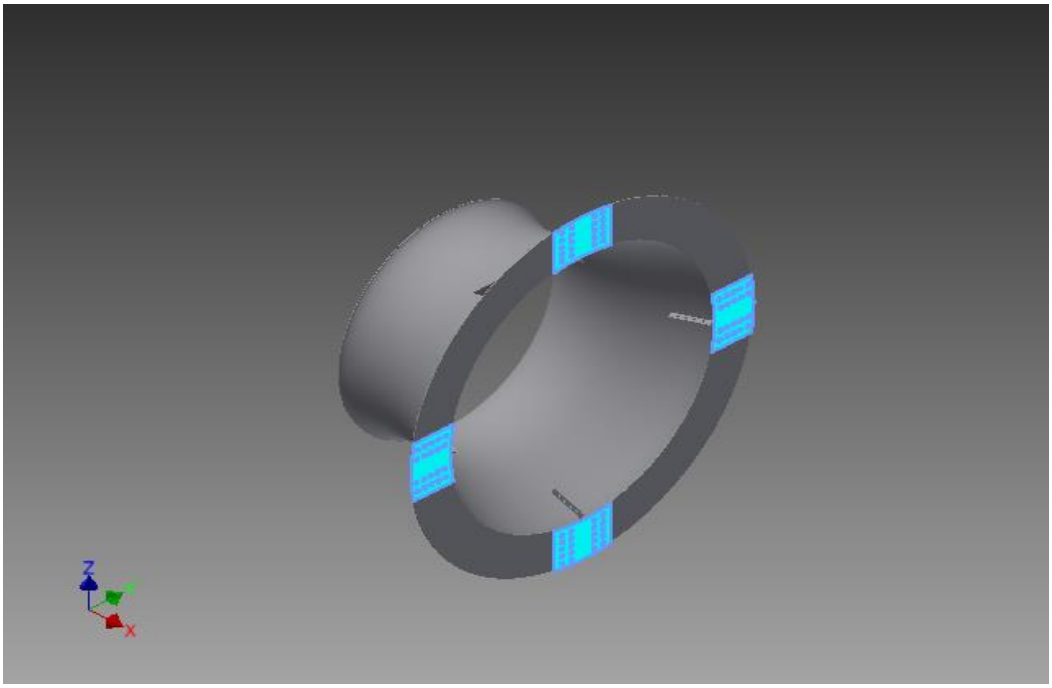

Figure 3-18 Fixed constraints positions

The mesh result is shown in Figure 3-19 (a) with 33617 nodes and 15818 elements. The results from the CFD simulation were taken into consideration in order to assign the load on the outer shroud as shown in Figure 3-19 (b) which is enumerated in Table 3-10.

Table 3-10 Loads and constraints on outer shroud

Surface	**Load type**	**Direction**	**Magnitude**
Flanged end	Pressure	X	11688Pa
Flanged end	Force	X	117N
Outer ring surface	Pressure	X	5035Pa
Outer ring surface	Pressure	Y	641Pa
Outer ring surface	Force	X	135N
Outer ring surface	Force	Y	-4.65N
Whole part body	Gravitational	-Z	16080N

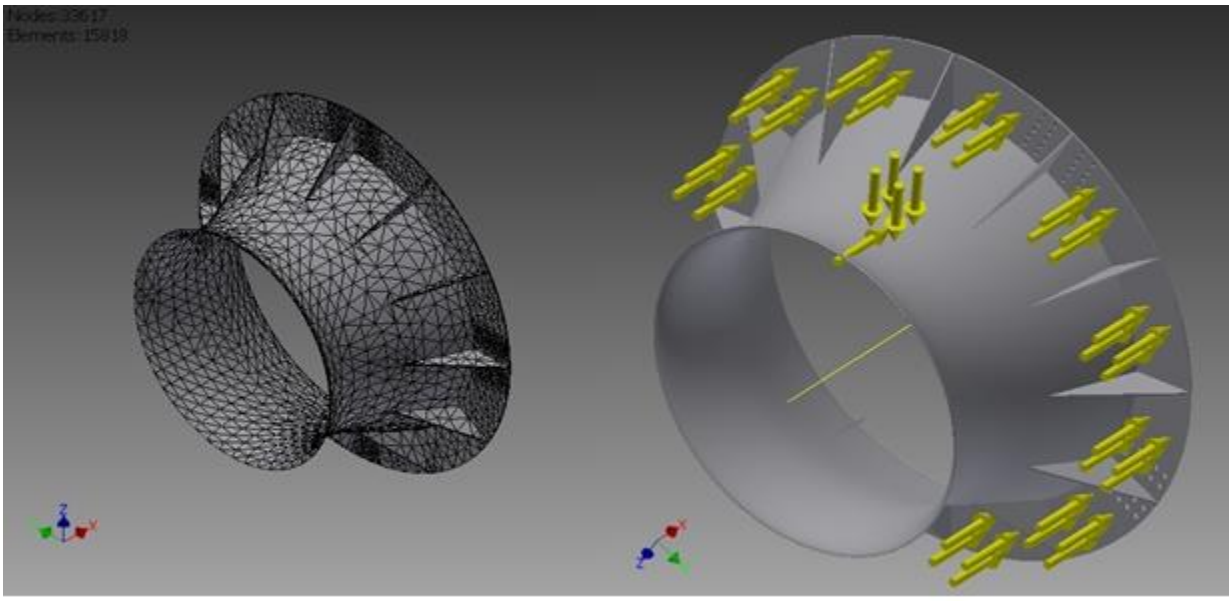

Figure 3-19 Mesh (a) of the model and the different loads (b) on the outer shroud

3.6.4.2 FEA model setup of the lower shroud front part

The single point design objective was selected and the static analysis for the simulation type was designated. The fixed constraint type was selected as shown in Figure 3-20 highlighted with blue color.

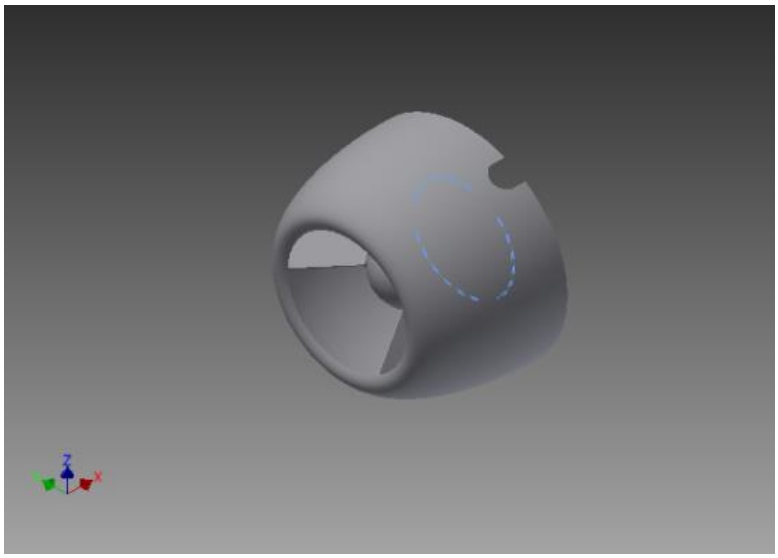

Figure 3-20 Fixed constraints position on the lower shroud front part

The load settings and the constraint settings on the hub are described in Table 3-11 below.

Table 3-11 Loads and constraints on lower shroud front hub

Surface	Load type	Direction	Magnitude
Outer surface	Pressure	X	412Pa
Outer surface	Pressure	Y	36Pa
Outer ring surface	Force	X	40N
Outer ring surface	Force	Y	9.95 e-02N

Mesh settings of the lower shroud front part are shown in Figure 3-21 (a) and the different types of load assigned to the lower shroud front part are shown in Figure 3-21 (b).

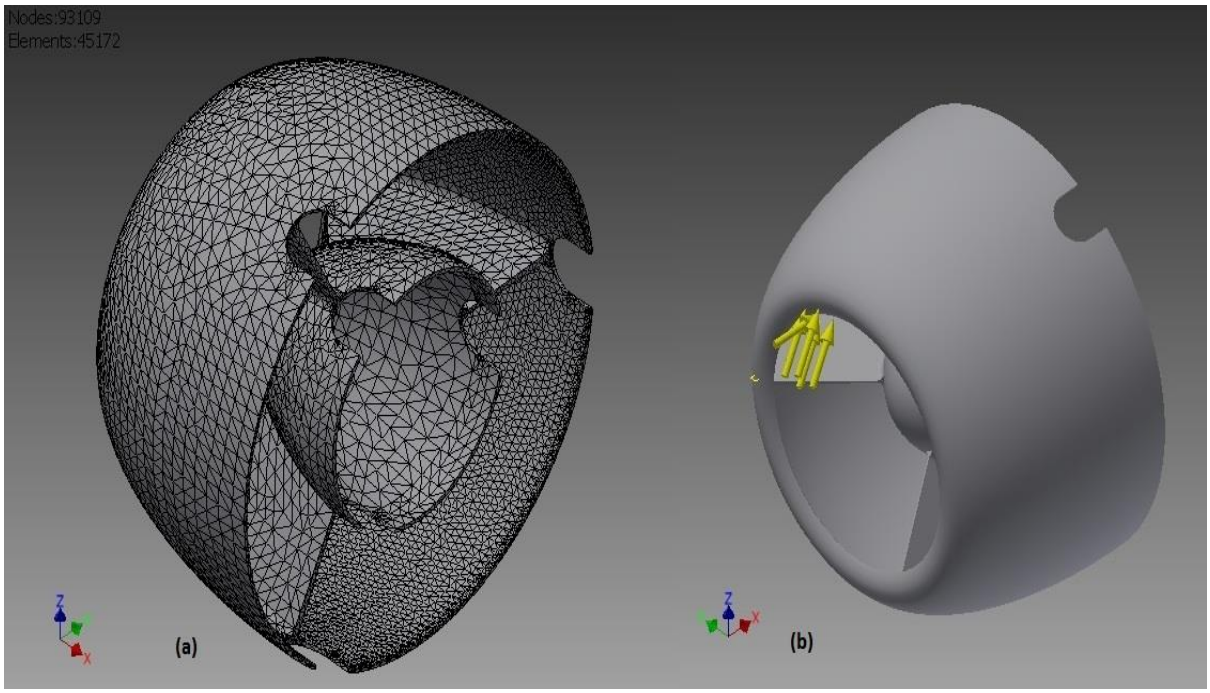

Figure 3-21 Mesh of the model and the different loads on the front inner shroud

The mesh settings of the lower shroud are given in Table 3-12.

Table 3-12 Mesh settings lower shroud front hub

Average Element Size (fraction of model diameter)	0.25
Minimum Element Size (fraction of avg. size)	0.05
Grading Factor	1.5
Maximum Turn Angle	60^{O}
Create Curved Mesh Elements	Yes

3.6.4.3 FEA model setup of the lower shroud rear part

The single point design objective was selected and the simulation type static analysis designated. Fixed constraint type was selected as shown in Figure 3-22.

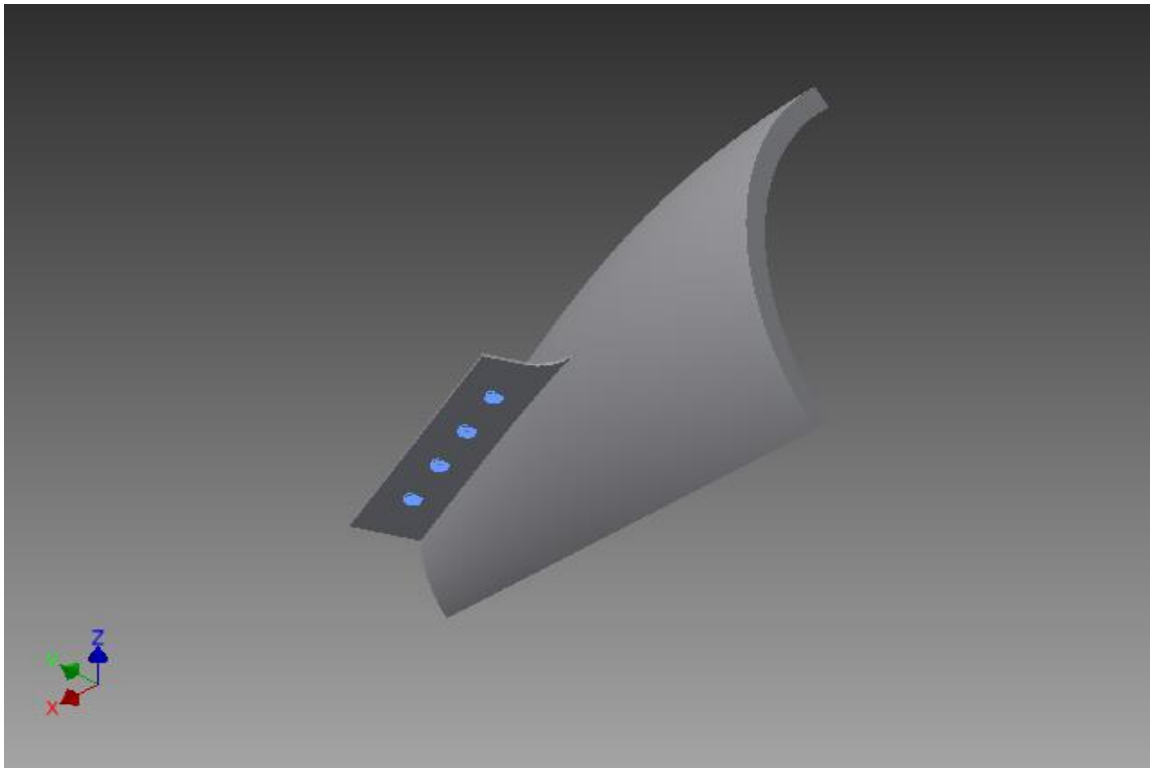

Figure 3-22 Fixed constraints positions on the lower shroud rear part

Mesh settings for the lower shroud rear part are shown in Figure 3-23 (a).

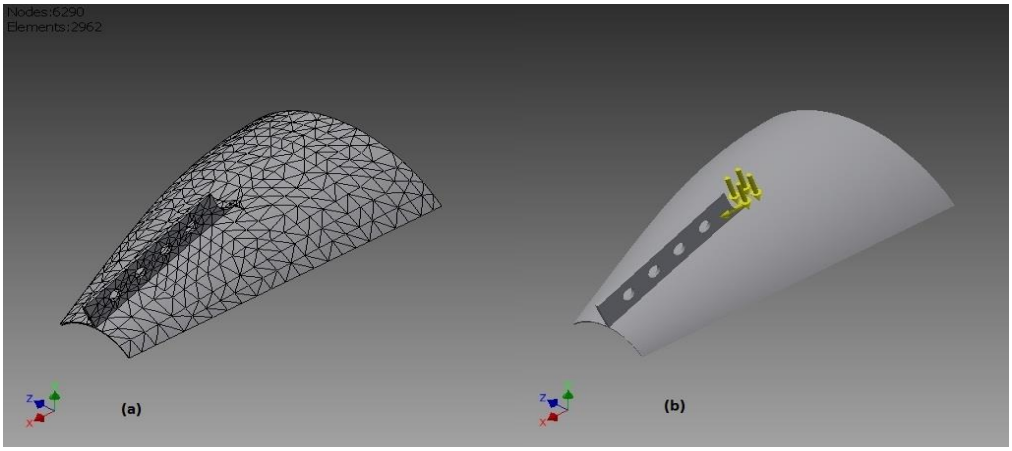

Figure 3-23 Mesh (a) of the model and the different loads (b) on the rear of inner shroud

Table 3-13 describes the parameters selected for the mesh settings of the lower shroud rear part.

Table 3-13 Mesh settings for lower shroud rear part

Average Element Size (fraction of model diameter)	0.1
Minimum Element Size (fraction of avg. size)	0.2
Grading Factor	1.5
Maximum Turn Angle	60^0
Create Curved Mesh Elements	Yes

Different loads assigned to the lower shroud rear part are described in Table 3-14 and shown in Figure 3-23 (b).

Table 3-14 Loads and constraints of lower shroud rear part

Surface	**Load type**	**Direction**	**Magnitude**
Outer surface	Pressure	X	412Pa
Outer surface	Pressure	Y	36Pa
Outer ring surface	Force	X	40N
Outer ring surface	Force	Y	9.95 e-02N

3.6.4.4 FEA model setup of the hold-down arms part

The single point design objective was selected and static analysis for the simulation type was designated. Fixed constraint type was selected as shown in Figure 3-24 marked with blue color.

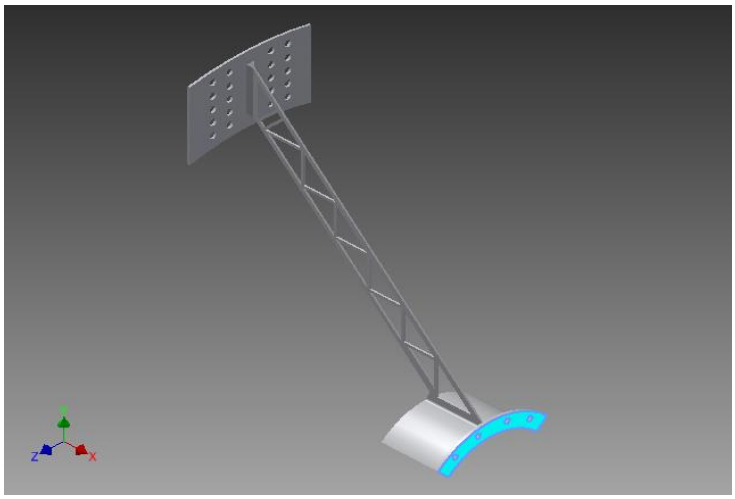

Figure 3-24 Fixed constraints position on the holding arms

Mesh settings of the hold-down arms part are shown in Figure 3-25 (a). The different types of load assigned to the hold-down arms part are shown in Figure 3-25 (b).

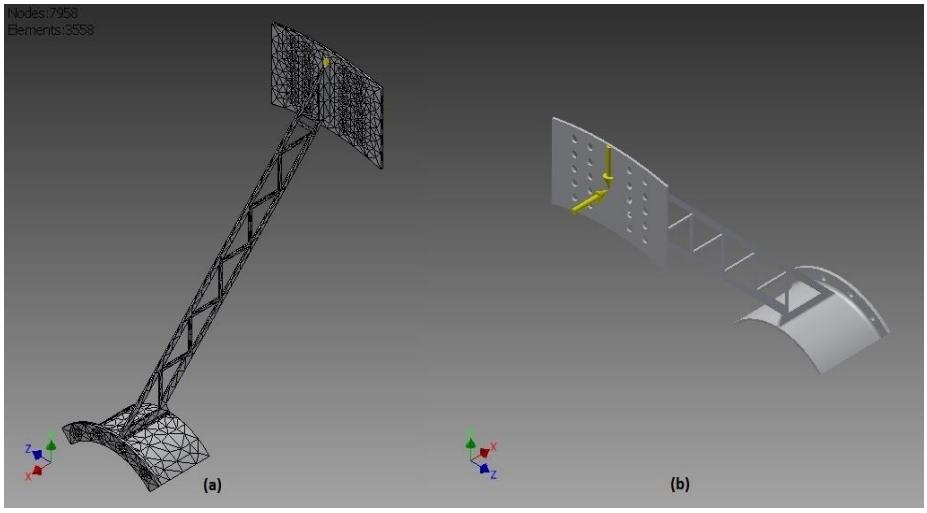

Figure 3-25 Mesh (a) of the model and the different loads (b) on the hold-down arms

The mesh settings used to perform the FEA on the hold-down arms are given in Table 3-15.

Table 3-15 Mesh settings of hold-down arms

Average Element Size (fraction of model diameter)	0.1
Minimum Element Size (fraction of avg. size)	0.2
Grading Factor	1.5
Maximum Turn Angle	60^0
Create Curved Mesh Elements	Yes

The loads which the hold-down arms are subjected to are given in Table 3-16.

Table 3-16 Loads and constraints on hold-down arms

Surface	**Load type**	**Direction**	**Magnitude**
Holding plate	Force	X	350N
Holding plate	Force	Y	10000N

3.6.4.5 FEA model setup of the cross-bracing part

The single point design objective was selected and the simulation type static analysis designated. Fixed constraint type was selected as shown in Figure 3-26 with the color blue.

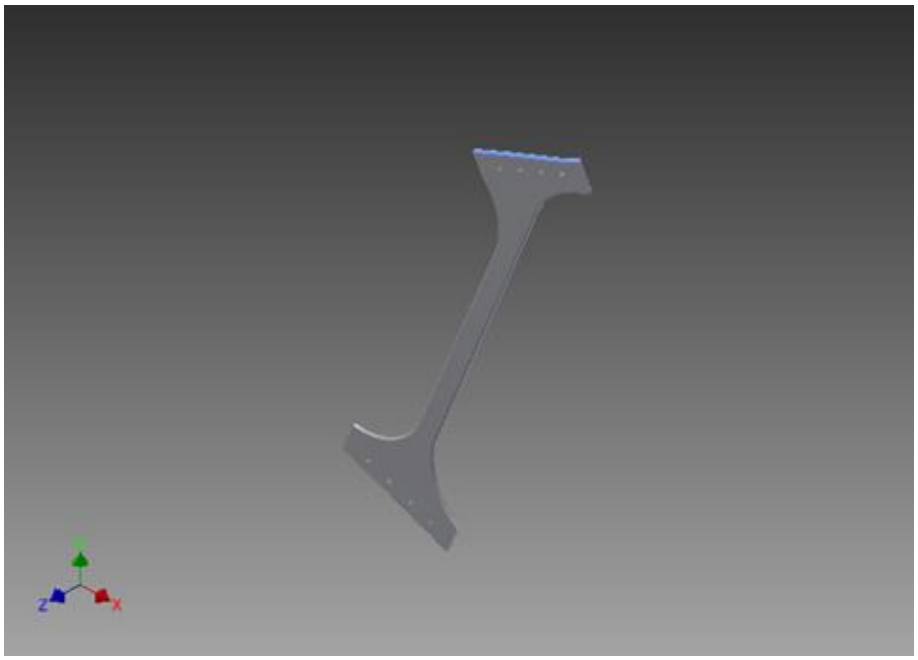

Figure 3-26 Constraints position on cross-bracing

The mesh settings for the cross-bracing part are shown in Figure 3-27 (a) and the loads applied on the cross-bracing is shown in Figure 3-27 (b).

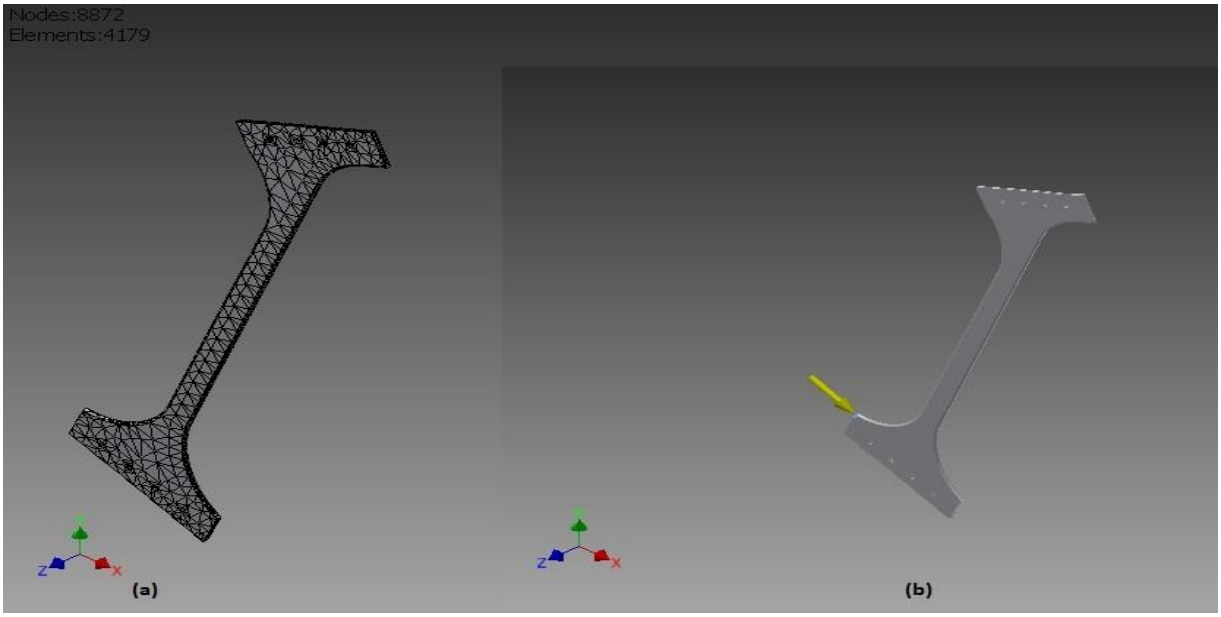

Figure 3-27 Mesh (a) of the model and the different loads (b) on the cross-bracing

Mesh settings for the cross-bracing for the FEA of the part are given in Table 3-17.

Table 3-17 Mesh settings of cross-bracing

Average Element Size (fraction of model diameter)	0.1
Minimum Element Size (fraction of avg. size)	0.2
Grading Factor	1.5
Maximum Turn Angle	60^0
Create Curved Mesh Elements	Yes

The different types of load that are applied over the cross-bracing part are given in Table 3-18.

Table 3-18 Loads position on cross-bracing

Surface	**Load type**	**Direction**	**Magnitude**
Surface	Force	X	1865N
Surface	Force	Y	820N

3.6.4.6 FEA model setup of the pole part

The single point design objective was selected and the simulation type static analysis designated. Fixed constraint type was selected as shown in Figure 3-28 with the color blue.

Figure 3-28 Fixed constraint position on the pole

The meshed surface of the pole is shown in Figure 3-29 (a) and the load applied to pole is shown in Figure 3-29 (b).

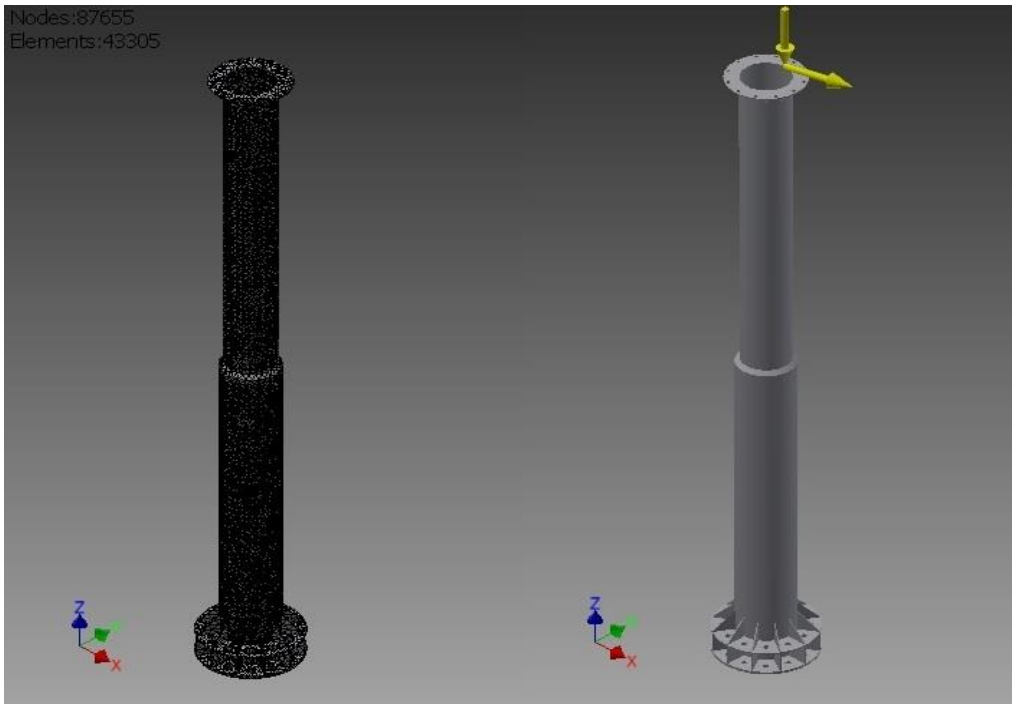

Figure 3-29 Mesh (a) of the model and the different loads (b) on the pole

The FEA mesh settings for the pole are described in Table 3-19.

Table 3-19 Mesh settings of the pole

Average Element Size (fraction of model diameter)	0.1
Minimum Element Size (fraction of avg. size)	0.2
Grading Factor	1.5
Maximum Turn Angle	60^0
Create Curved Mesh Elements	Yes

The loads that are applied on the pole including the weight of the pole itself are described in Table 3-20.

Table 3-20 Loads applied on the pole

Surface	**Load type**	**Direction**	**Magnitude**
Surface	Force	X	6500N
Surface	Force	-Z	40000N
Gravity	Force	-Z	30111.3N

4. ANALYIS AND DISCUSSION OF RESULTS

4.1 Presentation of CFD results

Figure 4-1 shows a segmented blade of the wind turbine in order to understand how wind distribution will affect the turbine blade system which will be placed in the throat of the shroud to gain maximum energy. The results of wind distribution on the blade segments are as follows:

- For outer most span near the tip or segment (1) the wind speed is of the range 4.64m/s.
- For the span or segment (2) the wind speed is of the range 4.62-3.86m/s.
- For the span or segment (3) the wind speed is of the 3.86-3.4m/s.
- For the span or segment (4) the wind speed is of the range 4.25-3.86m/s.
- For inner most span near the root or segment (5) the wind speed is of the range 4.25m/s.

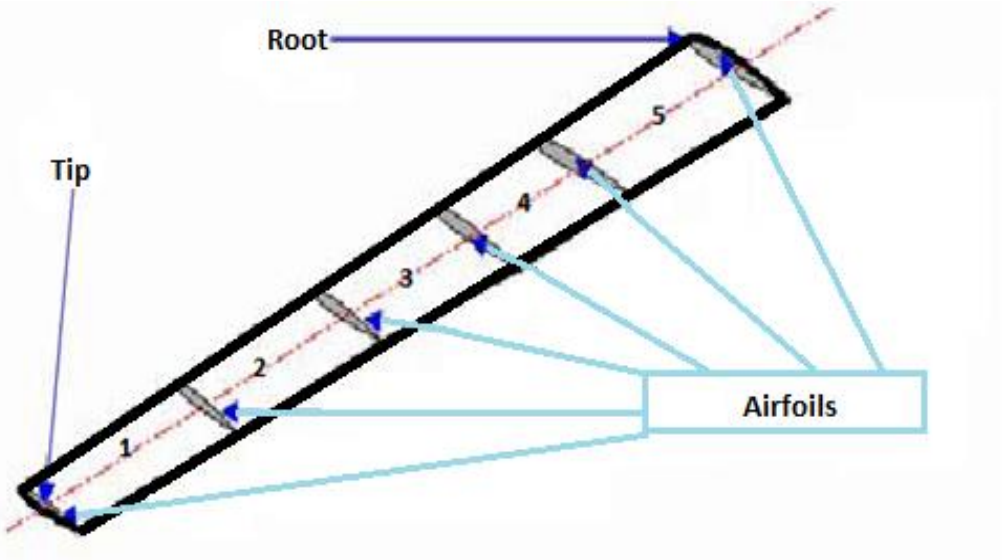

Figure 4-1 Segmented Airfoil distribution of wind on turbine blade

Wind speed was simulated in the double shroud at a wind speed of 2m/s and results of the simulation are shown in Figure 4-2. Analysis of the wind distribution is shown by means of different color contours. It was found that wind speed was highest at the entrance of the shroud where the two crests of the airfoil are opposite each other and at the lower rear end of the shroud. The outlet wind speed was drastically reduced behind the flanged end.

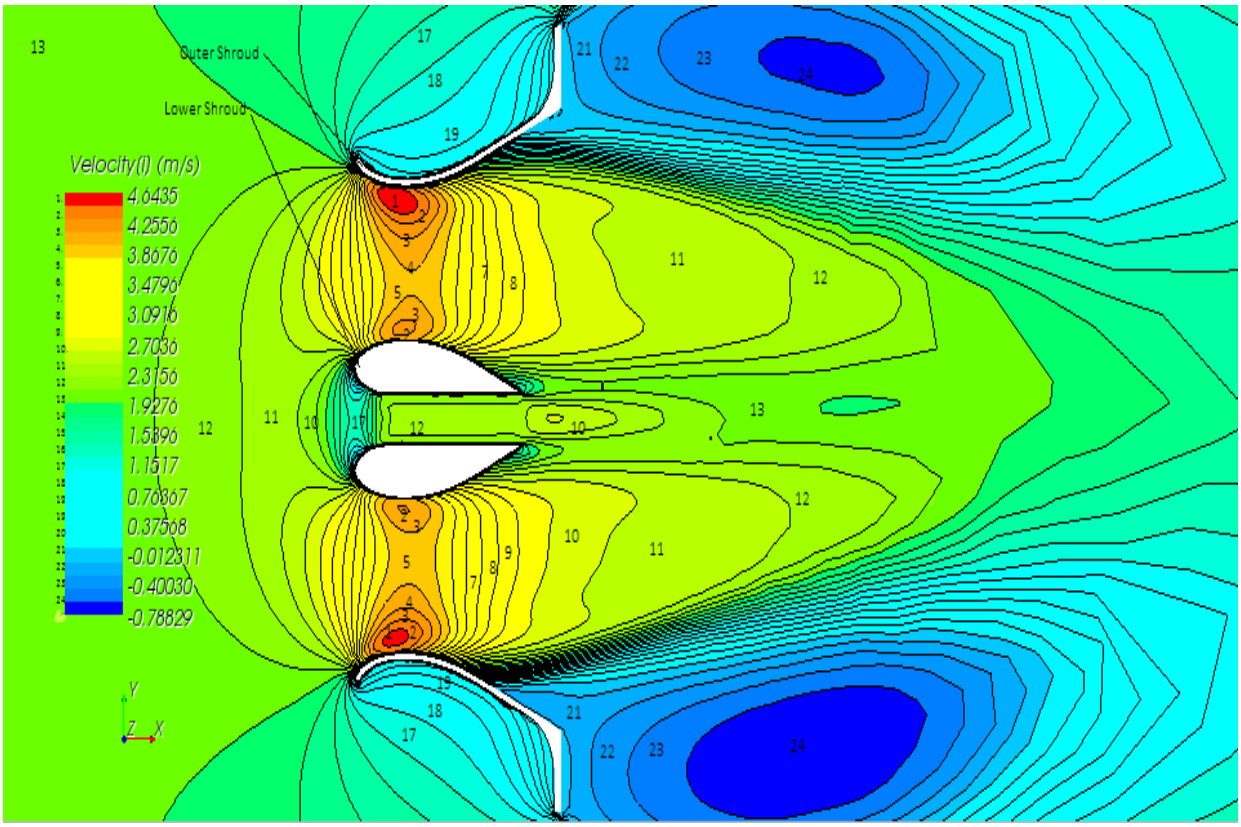

Figure 4-2 Velocity field illustration at 2m/s wind speed

Figure 4-3 shows the pressure distribution in derived plane regions at a wind speed of 2m/s. The maximum pressure on the outer and the low pressure beneath the outer shroud inside surface together tries to squeezing the whole outer shroud outside in and in case of lower shroud there is only one negative pressure region on the crest of the lower shroud. Due to this, only a small amount of force is developed on the surface of the lower shroud compared to the outer shroud. This happens because the design cut the cylindrical protrusion out from the lower shroud to make it more symmetrical to make space for the shaft carrying the wind turbine blades. Therefore it does not create any interference with the air so the pressure inside the lower shroud remains unaffected.

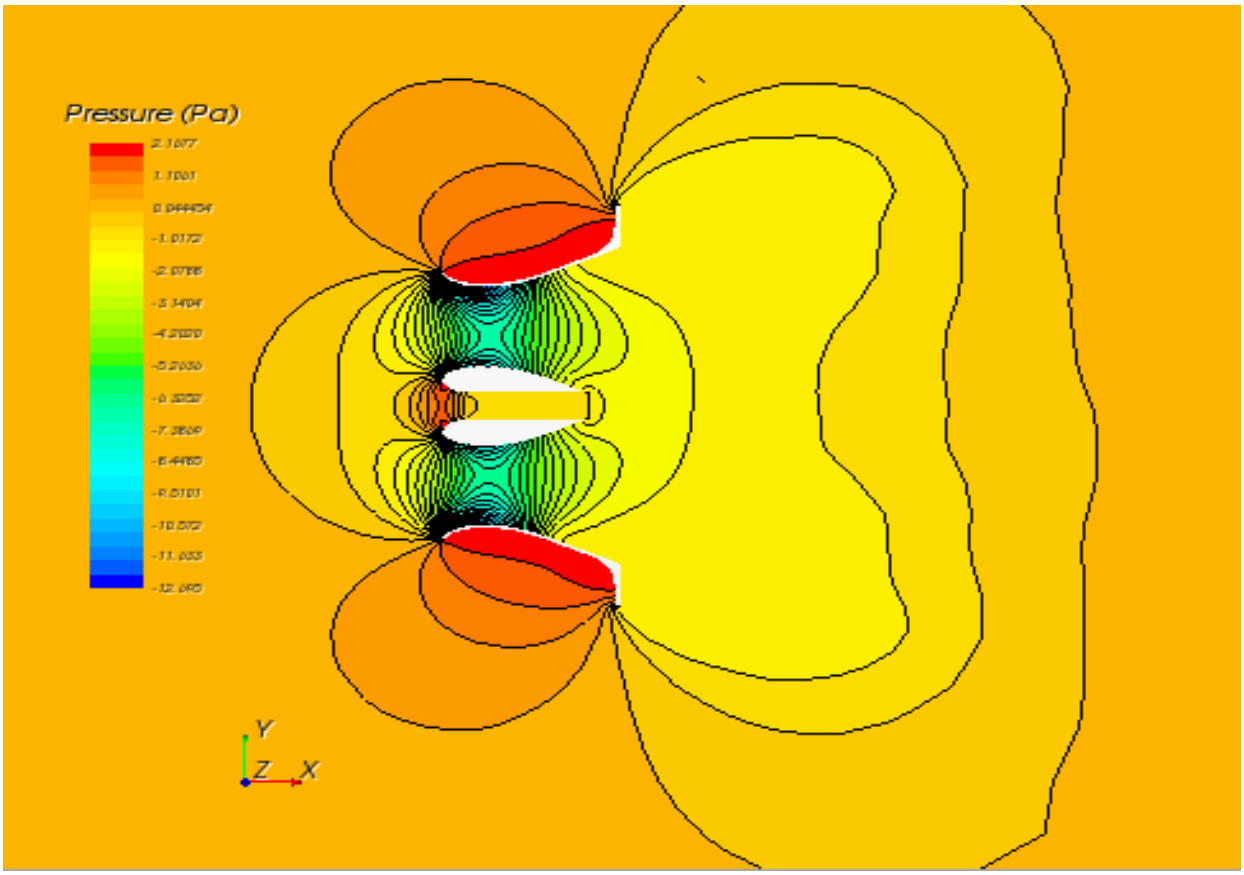

Figure 4-3 Pressure field representation at 2m/s wind speed

Turbulence plays a vital role in designing any machine which uses fluid dynamics so it is important to keep the turbulence factor in mind all the time while designing. Turbulence is generally created in fluid flows in which fluid undergoes irregular fluctuation, or mixing, in contrast to laminar flow, in which the fluid flows in smooth paths or layers. In turbulent flow the speed of the fluid at a point is continuously undergoing changes in both magnitude and direction [**68**].

Figure 4-4 shows the turbulence kinetic energy field in the derived cross sectional plane. We can clearly see that there is no turbulence in the throat region where the blades of the turbine will be rotating so there will be only laminar flow which is advantageous since laminar flow is required to extract maximum amount of energy. A small amount of turbulence kinetic energy will be experienced by the shroud at the boundary of the shroud at the inner side which will not affect the energy extraction process. The maximum turbulence is experienced behind the flange and also at the edges of it.

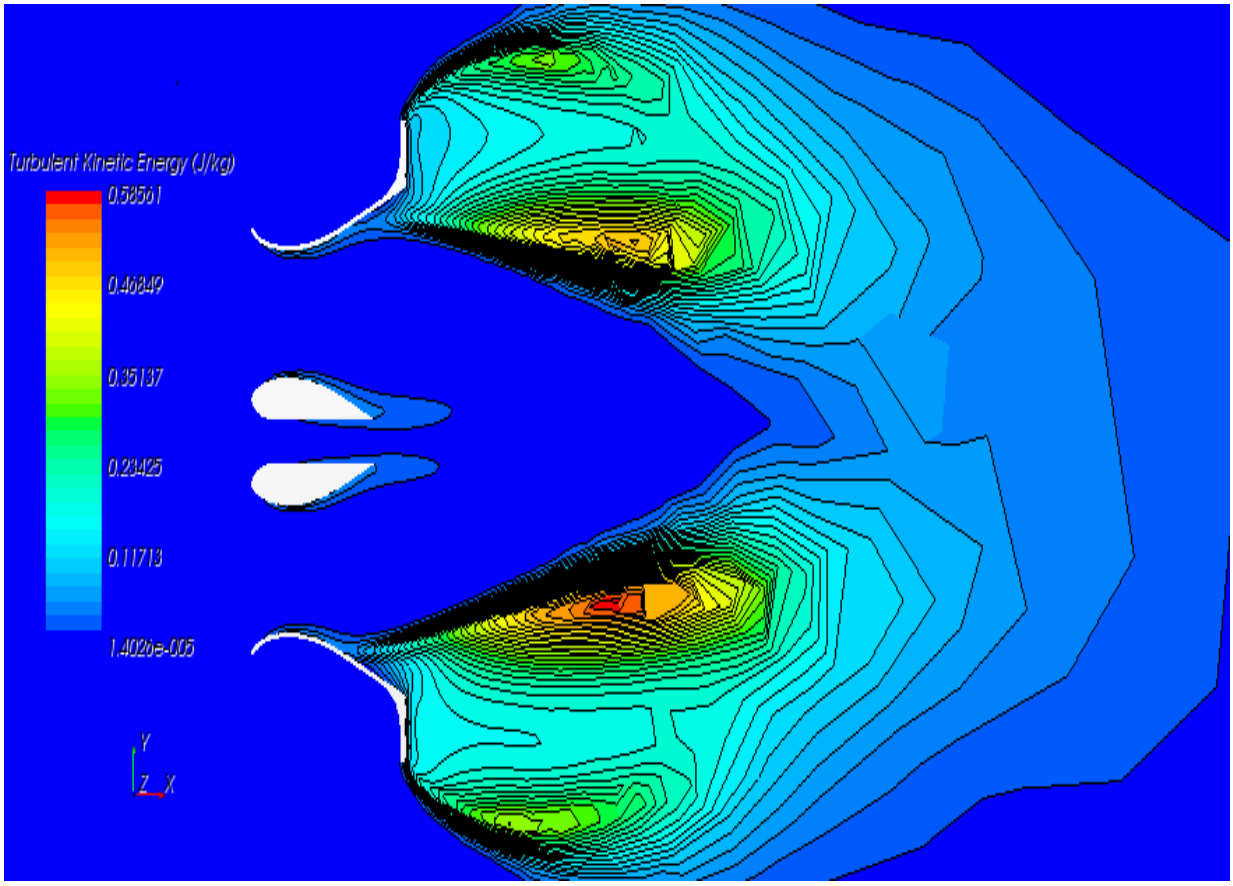

Figure 4-4 Turbulent kinetic energy field

Figure 4-5 shows the simulation results for the maximum output wind speed at 2m/s normal wind speed inside the shroud at the throat which is the red contour color shown in Figure 4-6. The maximum output wind speed is 4.62m/s against reproductive cycle or iteration. For the first ten iterations the graph moves up to 6.5m/s due to the edges of the flange but during cycles 100-200 it comes down to 5.2-5.0m/s and after the 200th cycle starts declining till 500th cycle when it becomes steady or constant at the mark of 4.62m/s.

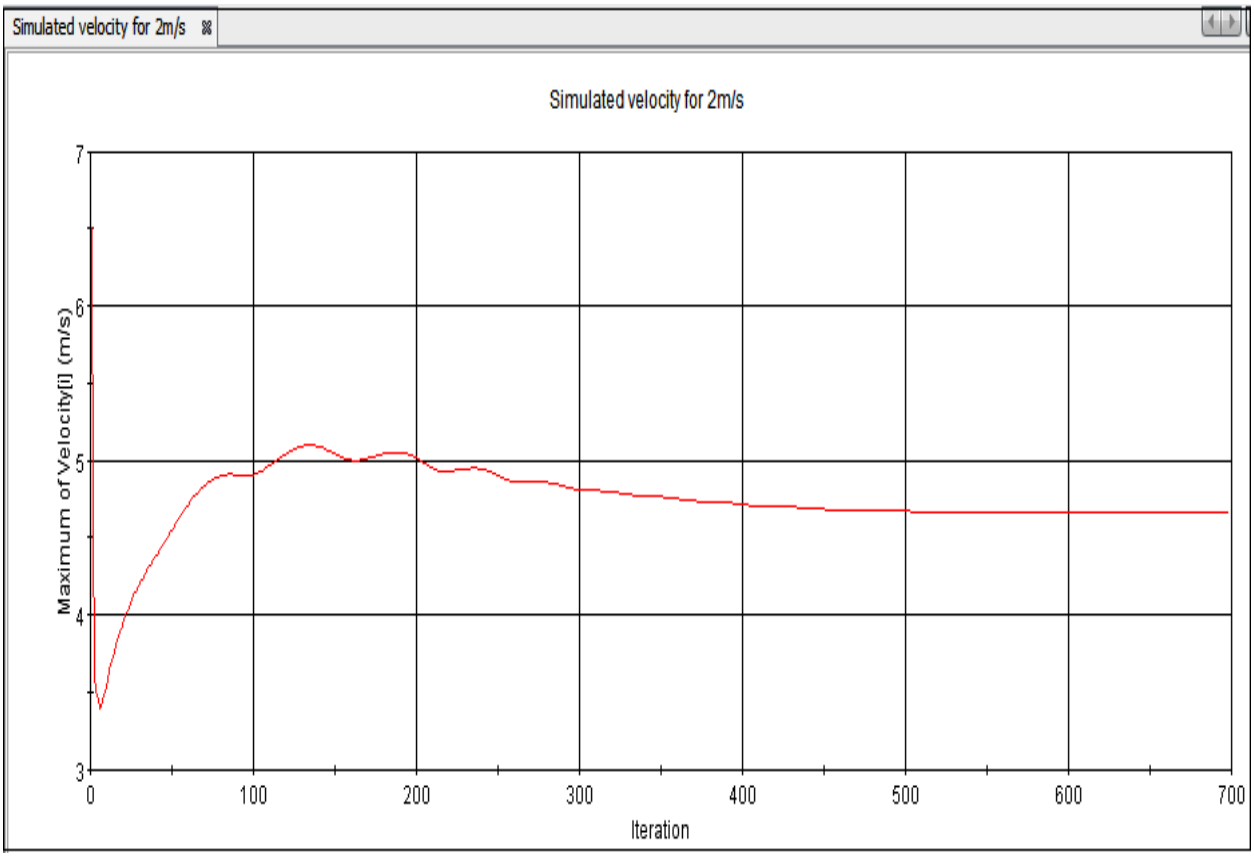

Figure 4-5 Velocity output graph for 2m/s

To test the design in the extreme conditions of a hurricane during which the wind speed is about 30-40m/s, a mandatory CFD simulation was required to analyze the maximum pressure and shear stress on the surface of the shroud design. The results thus produced were used to modify and optimize the design keeping the safety factor as the highest priority. Figure 4-6 shows the results for a wind speed of 40m/s.The following are results of the wind distribution on blade segments at 40m/s wind speed:

- For the outer most spans near the tip or segment (1) the wind speed is of the range 84.275m/s.
- For the span or segment (2) the wind speed is of the range 84.275-70.436m/s.
- For the span or segment (3) the wind speed is of the 70.436-63.517m/s.
- For the span or segment (4) the wind speed is of the range 77.356-70.436m/s.
- For inner most span near the root or segment (5) the wind speed is of the range 80.25m/s.

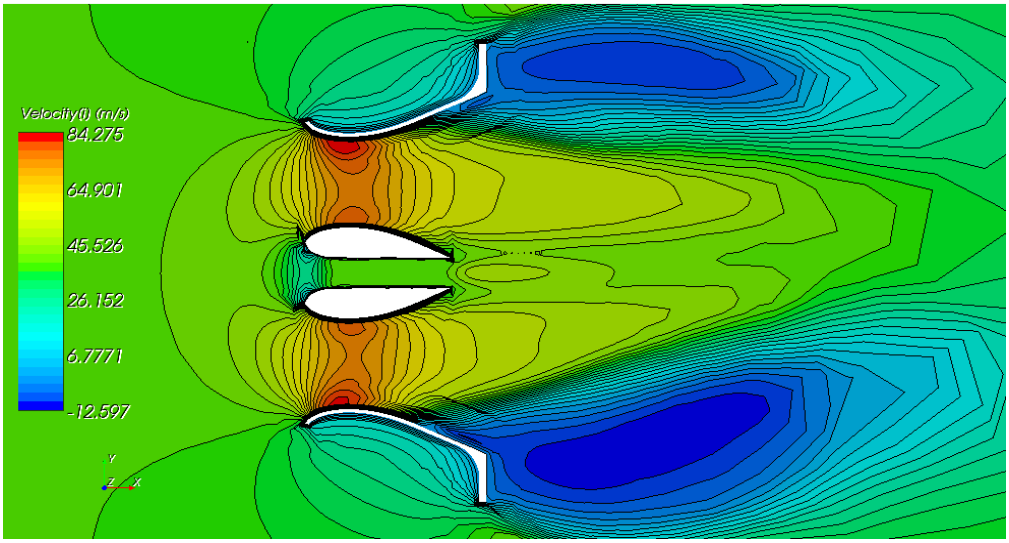

Figure 4-6 Velocity filed profile at 40m/s wind speed

The above results show a very high speed wind domain which is going to be very dangerous for the blades of the wind turbine so special attention should be paid while designing the turbine blades since velocity profile over the blade is very typical therefore requiring out of the box design of the blade. Figure 4-7 shows the pressure field representation at a wind speed of 40m/s. This simulation was performed to obtain the maximum pressure and the shear stress that the design has to sustain without losing the shape and entity.

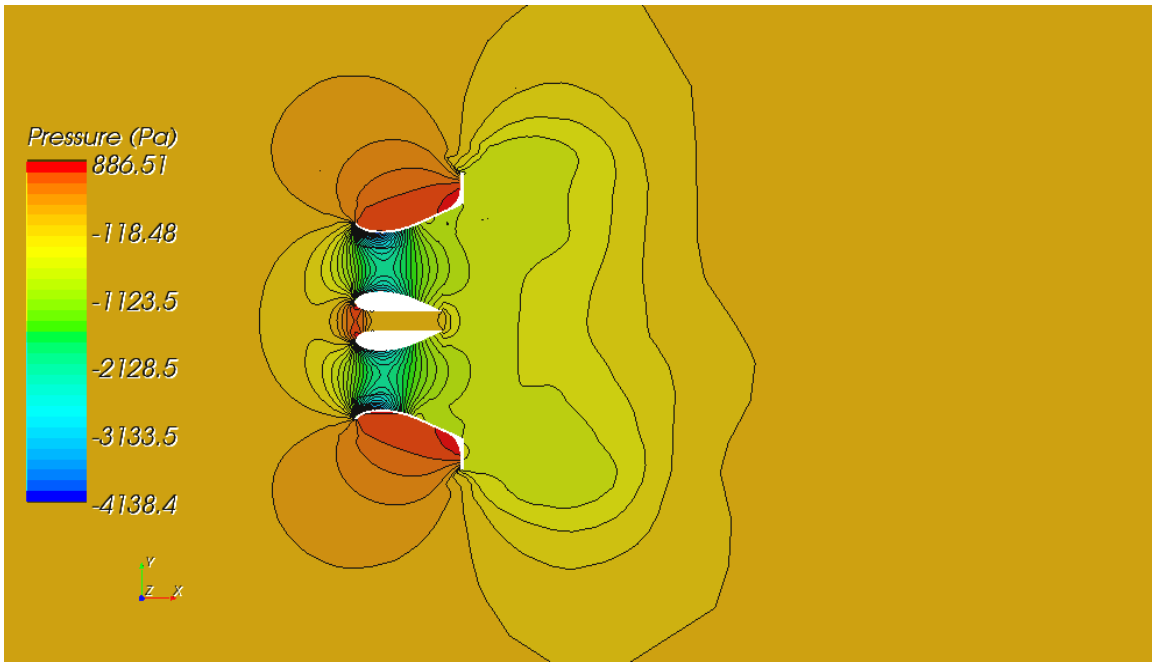

Figure 4-7 Pressure field at 40m/s wind speed

Figure 4-8 shows the pressure profile distribution on the surface of the shrouds. This helps us design the shroud so that it can withstand intense pressure during extreme hurricane conditions without failing. Different pressure reports were produced on different surfaces of the shrouds so that the FEA can be performed and the design can be optimized.

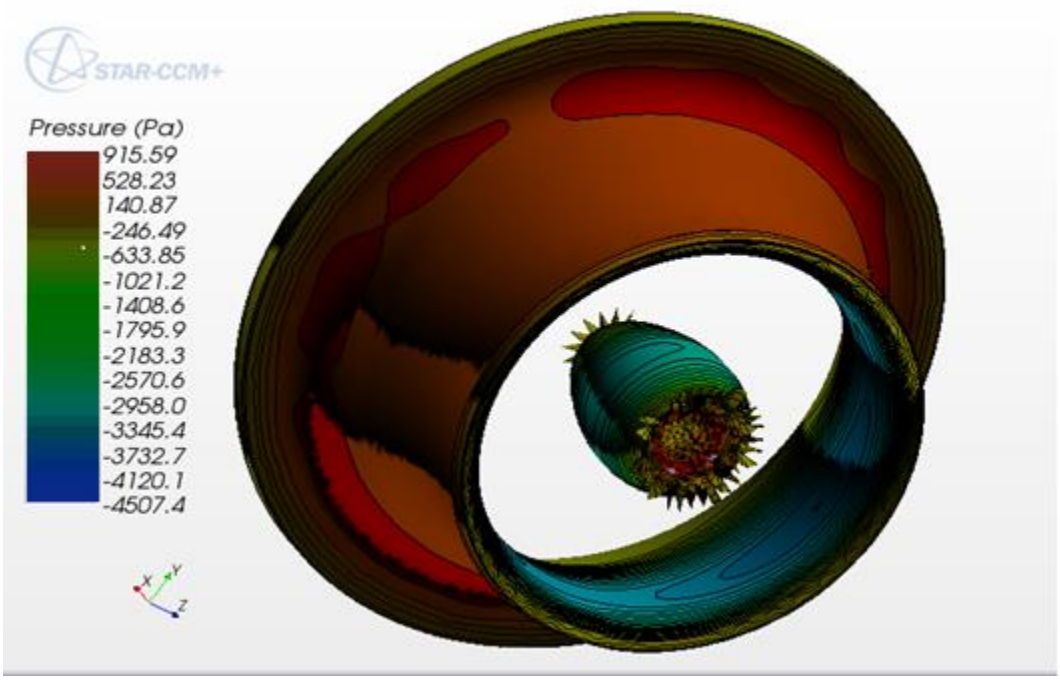

Figure 4-8 Pressure profile on the surfaces of the shrouds

4.2 The pressure and the force reports on the different surfaces of shrouds

All the reports in this section are produced considering the maximum wind velocity of 40m/s (due to unforeseen circumstances like storms or cyclonic activities) so that the design can bear that extreme pressure and thrust. All the data accumulated from the CFD analysis is then used to optimize the design for better functionality.

4.2.1 Flange pressure report

The pressure report of the flanged end of the shroud is shown in Report 4-1. The report was produced considering the wind flow perpendicular to the flange. The maximum value that is reported is 11688.003Pa.

Report 4-1 Pressure on flange

Reference Pressure = 0.0 Pa
Direction: [1.0, 0.0, 0.0]
Coordinate System: Laboratory

Vectors

Part	Pressure(N)	Net(N)
ah93w174_10d_flanged1.Face4	[1.168890e+04, -1.096692e-08, 5.004508e-12]	[1.168890e+04, -1.096692e-08, 5.004508e-12]
Total:	[1.168890e+04, -1.096692e-08, 5.004508e-12]	[1.168890e+04, -1.096692e-08, 5.004508e-12]

Component in direction: [1.000000e+00, 0.000000e+00, 0.000000e+00] in Laboratory coordinate system

Part	Pressure(N)	Net(N)
ah93w174_10d_flanged1.Face4	1.168890e+04	1.168890e+04
Total:	1.168890e+04	1.168890e+04

Monitor value: 11688.9033203125

4.2.2 Flange force report

The force report of the flanged end of the shroud is shown in Report 4-2. The report was produced considering the wind flow perpendicular to the flange. The maximum value that is reported is 117.142N.

Report 4-2 Force on flange

Reference Pressure = 0.0 Pa
Direction: [1.0, 0.0, 0.0]
Coordinate System: Laboratory

Vectors

Part	Shear(N)	Net(N)
ah93w174_10d_flanged1.Face4	[-1.171420e+02, 9.912401e-01, 3.335331e-01]	[-1.171420e+02, 9.912401e-01, 3.335331e-01]
Total:	[-1.171420e+02, 9.912401e-01, 3.335331e-01]	[-1.171420e+02, 9.912401e-01, 3.335331e-01]

Component in direction: [1.000000e+00, 0.000000e+00, 0.000000e+00] in Laboratory coordinate system

Part	Shear(N)	Net(N)
ah93w174_10d_flanged1.Face4	-1.171420e+02	-1.171420e+02
Total:	-1.171420e+02	-1.171420e+02

Monitor value: -117.14201354980469

4.2.3 Outer shroud pressure report X-direction

The pressure report of the outer shroud is shown in Report 4-3. The report was produced considering the flow of wind parallel to the axis of the shroud. The maximum value that is reported is 5035.272Pa.

Report 4-3 Pressure on outer shroud X-direction

```
Reference Pressure = 0.0 Pa
Direction: [1.0, 0.0, 0.0]
Coordinate System: Laboratory

Vectors

Part                          Pressure(N)                                  Net(N)
----------------------------- -------------------------------------------- --------------------------------------------
ah93w174_10d_flanged1.Face5   [ 5.035272e+03, -6.416971e+02,  2.930068e+03] [ 5.035272e+03, -6.416971e+02,  2.930068e+03]
----------------------------- -------------------------------------------- --------------------------------------------
Total:                        [ 5.035272e+03, -6.416970e+02,  2.930068e+03] [ 5.035272e+03, -6.416970e+02,  2.930068e+03]

Component in direction: [ 1.000000e+00,  0.000000e+00,  0.000000e+00] in Laboratory coordinate system
Part                          Pressure(N)   Net(N)
----------------------------- ------------ ------------
ah93w174_10d_flanged1.Face5    5.035272e+03  5.035272e+03
----------------------------- ------------ ------------
Total:                         5.035272e+03  5.035272e+03

Monitor value: 5035.2724609375
```

4.2.4 Outer shroud pressure report Y-direction

The pressure report of the outer shroud is shown in Report 4-4. The report was produced considering the flow of wind perpendicular to the axis of the shroud. The maximum value that is reported is 641.697Pa.

Report 4-4 Pressure on outer shroud Y-direction

```
Reference Pressure = 0.0 MPa
Direction: [0.0, 1.0, 0.0]
Coordinate System: Laboratory

Vectors

Part                          Pressure(N)                                  Net(N)
----------------------------- -------------------------------------------- --------------------------------------------
ah93w174_10d_flanged1.Face5   [ 5.035272e+03, -6.416971e+02,  2.930068e+03] [ 5.035272e+03, -6.416971e+02,  2.930068e+03]
----------------------------- -------------------------------------------- --------------------------------------------
Total:                        [ 5.035272e+03, -6.416970e+02,  2.930068e+03] [ 5.035272e+03, -6.416970e+02,  2.930068e+03]

Component in direction: [ 0.000000e+00,  1.000000e+00,  0.000000e+00] in Laboratory coordinate system
Part                          Pressure(N)   Net(N)
----------------------------- ------------- -------------
ah93w174_10d_flanged1.Face5   -6.416971e+02 -6.416971e+02
----------------------------- ------------- -------------
Total:                        -6.416970e+02 -6.416970e+02

Monitor value: -641.697021484375
```

4.2.5 Outer Shroud force report X-direction

The force report of the outer shroud is shown in Report 4-5. The report was produced considering the flow of wind parallel to the axis of the shroud. The maximum value that is reported is 132.310N.

Report 4-5 Force on outer shroud X-direction

```
Reference Pressure = 0.0 Pa
Direction: [1.0, 0.0, 0.0]
Coordinate System: Laboratory

Vectors

Part                          Shear(N)                                     Net(N)
----------------------------- -------------------------------------------- --------------------------------------------
ah93w174_10d_flanged1.Face5   [ 1.323103e+02,  8.706289e+00, -5.677967e+00] [ 1.323103e+02,  8.706289e+00, -5.677967e+00]
----------------------------- -------------------------------------------- --------------------------------------------
Total:                        [ 1.323103e+02,  8.706289e+00, -5.677967e+00] [ 1.323103e+02,  8.706289e+00, -5.677967e+00]

Component in direction: [ 1.000000e+00,  0.000000e+00,  0.000000e+00] in Laboratory coordinate system
Part                          Shear(N)      Net(N)
----------------------------- ------------- -------------
ah93w174_10d_flanged1.Face5    1.323103e+02  1.323103e+02
----------------------------- ------------- -------------
Total:                         1.323103e+02  1.323103e+02

Monitor value: 132.3103485107422
```

4.2.6 Outer shroud force report Y-direction

The pressure report of the outer shroud is shown in Report 4-6. The report was produced considering the flow of wind perpendicular to the axis of the shroud. The maximum value that is reported is -4.651N.

Report 4-6 Force on outer shroud Y-direction

```
Reference Pressure = 0.0 Pa
Direction: [0.0, 1.0, 0.0]
Coordinate System: Laboratory

Vectors

Part                          Shear(N)                                      Net(N)
----------------------------- --------------------------------------------- ---------------------------------------------
ah93w174_10d_flanged1.Face5   [ 1.330209e+02, -4.652124e+00, -3.195787e+00] [ 1.330209e+02, -4.652124e+00, -3.195787e+00]
----------------------------- --------------------------------------------- ---------------------------------------------
Total:                        [ 1.330209e+02, -4.652123e+00, -3.195787e+00] [ 1.330209e+02, -4.652123e+00, -3.195787e+00]

Component in direction: [ 0.000000e+00,  1.000000e+00,  0.000000e+00] in Laboratory coordinate system
Part                          Shear(N)      Net(N)
----------------------------- ------------- -------------
ah93w174_10d_flanged1.Face5   -4.652124e+00 -4.652124e+00
----------------------------- ------------- -------------
Total:                        -4.652123e+00 -4.652123e+00

Monitor value: -4.65212345123291
```

4.2.7 Inner shroud pressure report X-direction

The pressure report of the inner shroud is shown in Report 4-7. The report was produced considering the flow of wind parallel to the axis of the shroud. The maximum value that is reported is 412.085Pa.

Report 4-7 Pressure on inner shroud X-direction

```
Reference Pressure = 0.0 Pa
Direction: [1.0, 0.0, 0.0]
Coordinate System: Laboratory

Vectors

Part                          Pressure(N)                                    Net(N)
----------------------------- ---------------------------------------------- ----------------------------------------------
ah93w174_10d_flanged2.Faces6  [ 4.120854e+02,  3.570257e+01, -2.260960e+02] [ 4.120854e+02,  3.570257e+01, -2.260960e+02]
----------------------------- ---------------------------------------------- ----------------------------------------------
Total:                        [ 4.120854e+02,  3.570256e+01, -2.260959e+02] [ 4.120854e+02,  3.570256e+01, -2.260959e+02]

Component in direction: [ 1.000000e+00,  0.000000e+00,  0.000000e+00] in Laboratory coordinate system
Part                          Pressure(N)   Net(N)
----------------------------- ------------- -------------
ah93w174_10d_flanged2.Faces6   4.120854e+02  4.120854e+02
----------------------------- ------------- -------------
Total:                         4.120854e+02  4.120854e+02

Monitor value: 412.08538818359375
```

4.2.8 Inner shroud pressure report Y-direction

The pressure report of the inner shroud is shown in Report 4-8. The report was produced considering the flow of wind perpendicular to the axis of the shroud. The maximum value that is reported is 35.702Pa.

Report 4-8 Pressure on inner shroud Y-direction

```
Reference Pressure = 0.0 Pa
Direction: [0.0, 1.0, 0.0]
Coordinate System: Laboratory

Vectors

Part                          Pressure(N)                                    Net(N)
----------------------------- ---------------------------------------------- ----------------------------------------------
ah93w174_10d_flanged2.Faces6  [ 4.120854e+02,  3.570257e+01, -2.260960e+02] [ 4.120854e+02,  3.570257e+01, -2.260960e+02]
----------------------------- ---------------------------------------------- ----------------------------------------------
Total:                        [ 4.120854e+02,  3.570256e+01, -2.260959e+02] [ 4.120854e+02,  3.570256e+01, -2.260959e+02]

Component in direction: [ 0.000000e+00,  1.000000e+00,  0.000000e+00] in Laboratory coordinate system
Part                          Pressure(N)   Net(N)
----------------------------- ------------- -------------
ah93w174_10d_flanged2.Faces6   3.570257e+01  3.570257e+01
----------------------------- ------------- -------------
Total:                         3.570256e+01  3.570256e+01

Monitor value: 35.70256423950195
```

4.2.1 Inner shroud force report X-direction

The force report of the inner shroud is shown in Report 4-9. The report was produced considering the flow of wind parallel to the axis of the shroud. The maximum value that is reported is 38.570N.

Report 4-9 Force on inner shroud X-direction

```
Reference Pressure = 0.0 Pa
Direction: [1.0, 0.0, 0.0]
Coordinate System: Laboratory

Vectors

Part                          Shear(N)                                      Net(N)
----------------------------- --------------------------------------------- ---------------------------------------------
ah93w174_10d_flanged2.Faces6  [ 3.857085e+01,  9.956753e-02, -1.939487e+00] [ 3.857085e+01,  9.956753e-02, -1.939487e+00]
----------------------------- --------------------------------------------- ---------------------------------------------
Total:                        [ 3.857085e+01,  9.956753e-02, -1.939487e+00] [ 3.857085e+01,  9.956753e-02, -1.939487e+00]

Component in direction: [ 1.000000e+00,  0.000000e+00,  0.000000e+00] in Laboratory coordinate system
Part                          Shear(N)      Net(N)
----------------------------- ------------- -------------
ah93w174_10d_flanged2.Faces6   3.857085e+01  3.857085e+01
----------------------------- ------------- -------------
Total:                         3.857085e+01  3.857085e+01

Monitor value: 38.57085037231445
```

*Please refer to Appendix A for the CFD simulation at different speeds.

4.3 Presentation of the FEA results

The data accumulated from the CFD analysis was imported into the FEA environment and analyzed. The FEA simulation results for every single component are presented in this section. Results are summarized in tabular form and presented in Tables 4-1 to 4-6.

4.3.1 Outer shroud

The FEA of the outer shroud is summarized in tabular form as shown in Table 4-1. The safety factor and maximum displacement can be graphically obtained from Figure C-0-5 and B-0-6 in Appendix B.

Table 4-1 Result summary for outer shroud

Volume	**1314460000mm^3**	
Mass	**1403.85kg**	
Name	**Minimum**	**Maximum**
Von Mises Stress	0.00127267MPa	57.22MPa
1st Principal Stress	-54.2774MPa	27.1618MPa
3rd Principal Stress	-107.944MPa	21.3228MPa
Displacement	0mm	112.248mm
Safety Factor	1.26354ul	15ul
Stress XX	-99.5584MPa	25.8065MPa
Stress XY	-20.4002MPa	19.012MPa
Stress XZ	-18.1468MPa	19.3258MPa
Stress YY	-59.8186MPa	24.6831MPa
Stress YZ	-7.59881MPa	7.16146MPa
Stress ZZ	-59.4974MPa	24.0182MPa
X Displacement	-6.84885mm	112.213mm
Y Displacement	-19.9928mm	19.8038mm
Z Displacement	-19.5343mm	20.4134mm
Equivalent Strain	0.000000415849ul	0.0161988ul
1st Principal Strain	-0.000462923ul	0.00525421ul
3rd Principal Strain	-0.0192042ul	0.000350952ul
Strain XX	-0.0151872ul	0.00330281ul
Strain XY	-0.00788579ul	0.0073491ul
Strain XZ	-0.00701475ul	0.00747047ul
Strain YY	-0.0047388ul	0.00305082ul
Strain YZ	-0.00293736ul	0.00276829ul
Strain ZZ	-0.00482007ul	0.00292653ul

4.3.2 Lower shroud front hub

The FEA of the lower shroud front hub is summarized in tabular form as shown in Table 4-2. The safety factor and maximum displacement can be graphically obtained from Figures B-0-10 and B-0-11 in Appendix B.

Table 4-2 Result summary for lower shroud front hub

Volume	**37386300mm^3**	
Mass	**39.9286kg**	
Name	**Minimum**	**Maximum**
Von Mises Stress	0.00319746MPa	7.85728MPa
1st Principal Stress	-1.7222MPa	5.01305MPa
3rd Principal Stress	-8.89514MPa	1.79199MPa
Displacement	0mm	1.21851mm
Safety Factor	9.20166ul	15ul
Stress XX	-6.70391MPa	3.49323MPa
Stress XY	-2.72702MPa	2.19313MPa
Stress XZ	-2.44432MPa	2.50717MPa
Stress YY	-7.98522MPa	4.64575MPa
Stress YZ	-3.49345MPa	3.4295MPa
Stress ZZ	-6.74185MPa	4.06292MPa
X Displacement	-0.0210315mm	0.944183mm
Y Displacement	-0.944773mm	0.789142mm
Z Displacement	-0.921162mm	0.831808mm
Equivalent Strain	0.000000837351ul	0.00204402ul
1st Principal Strain	0.000000114276ul	0.00118799ul
3rd Principal Strain	-0.00222805ul	0.0000234889ul
Strain XX	-0.00173247ul	0.00076054ul
Strain XY	-0.00105414ul	0.000847766ul
Strain XZ	-0.000944864ul	0.00096915ul
Strain YY	-0.0019235ul	0.000883056ul
Strain YZ	-0.00135041ul	0.0013257ul
Strain ZZ	-0.00149607ul	0.00104377ul

4.3.3 Lower shroud rear part

The FEA of the lower shroud rear part is summarized in tabular form as shown in Table 4-3. The safety factor and maximum displacement can be graphically obtained from Figures B-0-15 and B-0-16 in Appendix B.

Table 4-3 Result summary for lower shroud rear part

Volume	**4396640mm^3**	
Mass	**4.69561kg**	
Name	**Minimum**	**Maximum**
Von Mises Stress	0.00412514MPa	6.79782MPa
1st Principal Stress	-1.4682MPa	6.78337MPa
3rd Principal Stress	-4.45721MPa	2.81955MPa
Displacement	0mm	4.40347mm
Safety Factor	10.6358ul	15ul
Stress XX	-2.31652MPa	6.75786MPa
Stress XY	-1.02013MPa	1.2176MPa
Stress XZ	-1.14295MPa	1.2904MPa
Stress YY	-2.536MPa	2.8927MPa
Stress YZ	-1.5278MPa	1.52726MPa
Stress ZZ	-4.41664MPa	5.6304MPa
X Displacement	-0.751439mm	1.96345mm
Y Displacement	-3.46527mm	3.66653mm
Z Displacement	-1.48053mm	1.49712mm
Equivalent Strain	0.00000106366ul	0.00176327ul
1st Principal Strain	0.00000067527ul	0.00188886ul
3rd Principal Strain	-0.00112193ul	0.00000140702ul
Strain XX	-0.00039644ul	0.00187323ul
Strain XY	-0.000394336ul	0.000470674ul
Strain XZ	-0.000441812ul	0.000498837ul
Strain YY	-0.000784061ul	0.00050512ul
Strain YZ	-0.000590605ul	0.000590369ul
Strain ZZ	-0.00110625	0.00117602ul

4.3.4 Hold-down arms

The FEA of the hold-down arms part is summarized in tabular form as shown in Table 4-4. The safety factor and maximum displacement can be graphically obtained from Figure C-0-20 in Appendix B.

Table 4-4 Result summary for hold-down arms

Volume	**74335900 mm^3**	
Mass	**201.45kg**	
Name	**Minimum**	**Maximum**
Von Mises Stress	0.00621683MPa	109.55MPa
1st Principal Stress	-19.1896MPa	128.19MPa
3rd Principal Stress	-110.115MPa	33.5477MPa
Displacement	0mm	37.5287mm
Safety Factor	2.5100ul	15ul
Stress XX	-67.1931MPa	117.31MPa
Stress XY	-57.7028MPa	48.2178MPa
Stress XZ	-25.1443MPa	24.7724MPa
Stress YY	-63.1476MPa	59.407MPa
Stress YZ	-33.0811MPa	29.3348MPa
Stress ZZ	-103.126MPa	51.1083MPa
X Displacement	-28.605mm	0.118508mm
Y Displacement	-24.437mm	1.3994mm
Z Displacement	-1.34116mm	1.3577mm
Equivalent Strain	0.0000000836791ul	0.00144764ul
1st Principal Strain	0.000000061332ul	0.0016253ul
3rd Principal Strain	-0.0014087ul	-0.0000000653955ul
Strain XX	-0.000915049ul	0.00129634ul
Strain XY	-0.0011138ul	0.000930765ul

Strain XZ	-0.000485369ul	0.00047819ul
Strain YY	-0.000765501ul	0.000665154ul
Strain YZ	-0.000638576ul	0.00056626ul
Strain ZZ	-0.00119886ul	0.000726628ul

4.3.5 Cross arm bracing

The FEA of the cross arm bracing is summarized in tabular form as shown in Table 4-5. The safety factor and maximum displacement can be graphically obtained from Figures B-0-25 and B-0-26 in Appendix B.

Table 4-5 Result summary for cross arm bracing

Volume	**9971550 mm^3**	
Mass	**27.0229kg**	
Name	**Minimum**	**Maximum**
Von Mises Stress	0.00683439MPa	86.281MPa
1st Principal Stress	-4.62237MPa	86.7161MPa
3rd Principal Stress	-78.797MPa	12.1671MPa
Displacement	0mm	29.4676mm
Safety Factor	3.18726ul	15ul
Stress XX	-10.7551MPa	16.9549MPa
Stress XY	-26.427MPa	28.4858MPa
Stress XZ	-2.45843MPa	3.15571MPa
Stress YY	-68.641MPa	80.0317MPa
Stress YZ	-2.36852MPa	10.360MPa
Stress ZZ	-10.4244MPa	12.8936MPa
X Displacement	-0.0276751mm	28.800mm
Y Displacement	-16.5953mm	0.0986955mm
Z Displacement	-0.241691mm	4.86298mm
Equivalent Strain	0.0000000953395ul	0.00112888ul
1st Principal Strain	-0.00000421756ul	0.00125439ul
3rd Principal Strain	-0.00113998ul	0.000000572454ul
Strain XX	-0.000352312ul	0.000179501ul
Strain XY	-0.000510129ul	0.00054987ul
Strain XZ	-0.0000474559ul	0.0000609158ul
Strain YY	-0.0009437ul	0.0011253ul

Strain YZ	-0.000045720ul	0.000199989ul
Strain ZZ	-0.00041196ul	0.000377118ul

4.3.6 Tower

The FEA of the tower is summarized in tabular form as shown in Table 4-6. The safety factor and maximum displacement can be graphically obtained from Figures B-0-30 and B-0-31 in Appendix B.

Table 4-6 Results summary for the pole

Volume	**383096000mm^3**	
Mass	**3011.13kg**	
Name	**Minimum**	**Maximum**
Von Mises Stress	0.000071531MPa	66.2733MPa
1st Principal Stress	-21.4177MPa	66.85MPa
3rd Principal Stress	-79.1054MPa	15.582MPa
Displacement	0mm	11.3992mm
Safety Factor	3.1234ul	15ul
Stress XX	-32.001MPa	30.4951MPa
Stress XY	-13.8798MPa	15.5921MPa
Stress XZ	-28.5515MPa	30.4912MPa
Stress YY	-50.6321MPa	40.8743MPa
Stress YZ	-12.990MPa	20.518MPa
Stress ZZ	-77.1434MPa	55.6385MPa
X Displacement	-0.00808315mm	10.949mm
Y Displacement	-0.00475609mm	2.93371mm
Z Displacement	-1.20892mm	0.890448mm
Equivalent Strain	0.000000000310104ul	0.000276826ul
1st Principal Strain	-0.0000190821ul	0.00027119ul
3rd Principal Strain	-0.000322069ul	0.0000155528ul
Strain XX	-0.000072012ul	0.000127444ul
Strain XY	-0.00008044ul	0.0000903636ul
Strain XZ	-0.000165469ul	0.00017671ul
Strain YY	-0.000115108ul	0.00011284 ul
Strain YZ	-0.0000752878ul	0.000118913ul
Strain ZZ	-0.000310697ul	0.000206221ul

4.4 Discussion of the results

The research study results which have been accumulated through various CFD simulations have been analyzed and data was plotted against ambient speed and simulated wind speed as shown in Figure 4-9. The output wind speed is spread over the whole blade and is divided into different segments or spans, namely: the tip, the middle span and the root of the blade. The wind speed distribution on a blade as shown in Figure 4-9 presents a challenge to design a blade which can withstand the different shear forces and pressure while at the same time be able to extract the maximum amount of wind energy. As shown in Figure 4-9 the blade is divided into 5 spans in which the 5th segment is the tip of the blade and shares 20% of the blade span. The 4th, 3rd and 2nd segments form the middle span of the blade and share 60% of the effective blade area. The 1st segment forms the root of the span and shares 20% of the blade span. Figure 4-9 shows that the tip of the blade or the 5th segment is going to experience the maximum projected wind speed which increases from 2.32m/s to 2.38m/s, the middle span is going to experience moderate wind speed increasing from 1.83m/s to 2.08m/s and the root will experience high wind speed which increased from 2.18m/s to 2.21m/s.

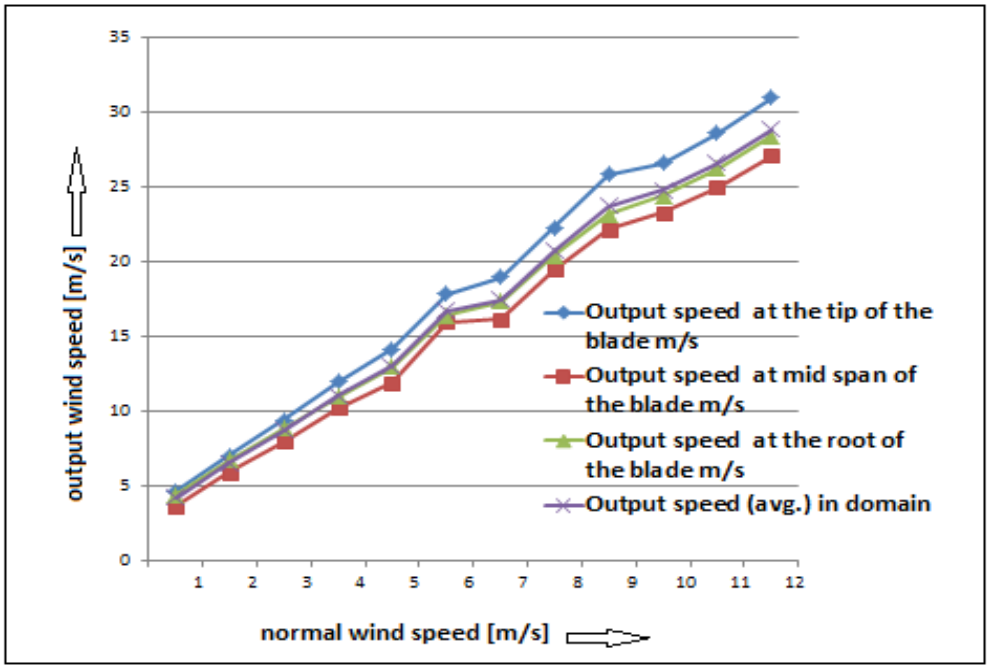

Figure 4-9 Simulated wind speed on the span of the blade

Figure 4-10 shows the graph of comparison between the single shroud and proposed double shroud output wind speed at a given speed of wind. The double shroud predominantly shows a remarkable effect on output wind speed. At the lower wind speed of 2m/s the shroud efficiently enhances the wind speed by

2.004 times and at the higher speed the of 13m/s the speed is increased by 2.16 times. While on the other hand the single shroud is only capable of increasing the wind speed by 1.73 times.

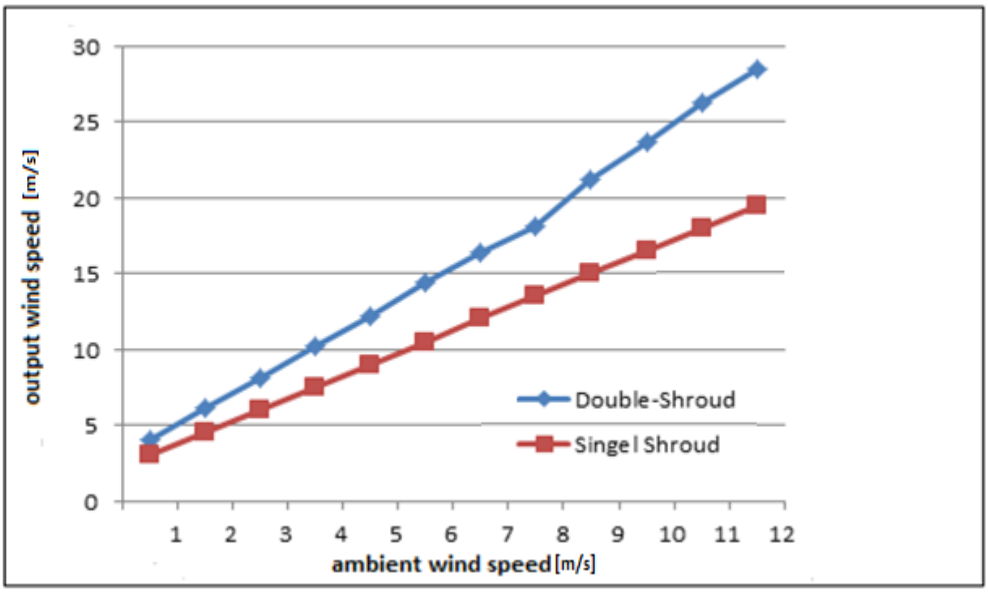

Figure 4-10 Comparison of single and double shroud wind turbine

Figure 4-11 shows the graph of Coefficient of performance (C_P) and wind speed of the double shrouded horizontal axis wind turbine and Figure 4-12 shows the comparisons of the C_P of the double shrouded horizontal axis wind turbine to the single shrouded wind turbine and the wind turbine without a shroud.

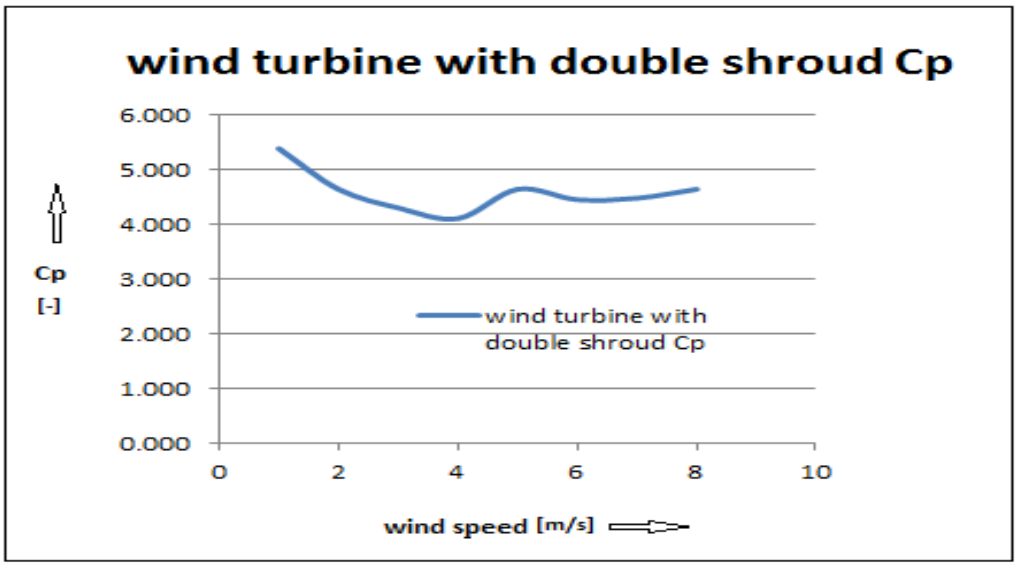

Figure 4-11 Coefficient of performance C_P of double shroud

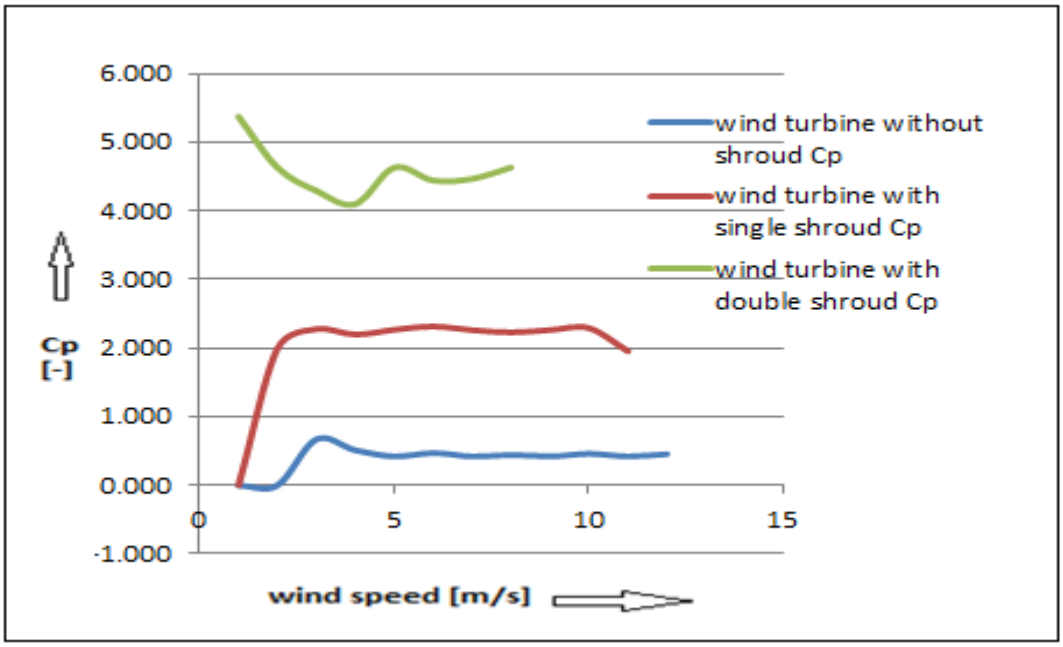

Figure 4-12 Coefficient of performance C_P. Comparison of double, single, and no shroud HAWT

4.5 Concluding highlights

The proportion of the power in the wind that the rotor can extract is termed the coefficient of the performance (or the power coefficient or the efficiency "C_p") (as shown in Appendix A from equations A.24 to A.26) and its variation as a function of tip speed ratio is commonly used to characterize different types of rotor. It's physically impossible to extract all the energy from the wind, without bringing the air behind the rotor to a standstill.

The upgrading of the HAWT to double shroud shows an excellent result in terms of the power output at low wind speed as is clear from the graphs shown in Figures 4-11 and 4-12. The construction possibilities have been proven from the part modeling and FEA.

5. CONCLUSIONS AND RECOMMENDATIONS

5.1 Conclusion

Experimental CFD simulation shows a markedly increased output in the wind speed at the entrance of the shroud. The different regions have a different wind speed which presents a challenge to design a blade that can withstand the different shear forces developed due to drag and lift forces throughout its segmented span and hence enhance the performance of the wind turbine.

The pressure distribution on the surface of the outer and inner shroud demand a reinforced design of the shroud to withstand the high contracting and expanding pressure on the outer and inner shroud. The parts of the shrouds were designed bearing in mind these problems and validation of the design was proven through the FEA.

All the parts of the shroud have been designed such that the fabrication process of every single part is feasible in respect to construction and is also economical. The material selection is made to keep the design as light as possible but can be changed with little change to the design and with no compromise regarding safety factors since all designs are made with parametric dimensioning which gives the flexibility to change dimensions quickly.

5.2 Predicted performance when a single shrouded HAWT is upgraded to a double shrouded HAWT

From the results of this research study, it is possible to predict performance when a single shrouded HAWT is upgraded to a double shrouded HAWT. The predicted performances of the double shrouded HAWT are as follows:

1. The improved aerodynamic design of the shroud helps to increase the wind speed in the domain where the wind turbine rotate and thus extract energy more efficiently;
2. The shroud provides primary protection acting as a casing in which the turbine blades rotate and can avoid accidents in case of turbine blade failure;
3. Wind turbines equipped with a double shroud have a great advantage of a very low cut-in wind speed of 1.5m/s at which the turbine starts producing electricity;

4. The efficiency of the shroud means the wind turbines can have comparatively smaller spanned blades while producing the same amount of energy as larger spanned blades; and
5. Due to the lower cut-in speed and low cut-out wind speed these turbine are best suited to city areas where there is very low wind speed due to urbanization.

5.3 Proposals for implementation

The double shroud HAWT has many advantages which can summarized as follows:

1. This design can be implemented in urban areas where the average wind speed is rarely high due to obstruction created by big buildings and turbulence due to moving traffic. This is because the aerodynamic design helps the air to concentrate on the turbine blades with increased velocity;
2. The double shroud can be implemented on existing wind turbine designs but with stronger blades because of the different velocity profile over the blade segments;
3. This design is applicable in areas such as remote telecommunication stations where it can serve as a standalone power supply for charging batteries which in turn act as power sources to electronics; and
4. Double shrouded HAWTS can easily be attached underneath bridges to catch the cross winds flowing under the bridges to supply electricity to bridges' lighting systems and monitoring equipment.

5.4 Recommendations for further studies

Recommendations for future work include:

1. Development of new types of blades because the wind profile over the blade segment varies from root to tip. Since the wind capturing capacity of the shroud is very high, building material should be tested and applied accordingly.
2. The variation of the chord length of airfoil used in the outer shroud can be optimized in order to make the design more economically viable.
3. More design variables are to be considered using different airfoils.

References

[1] Siegfried Heier, *Grid Integration of Wind Energy Coversion Systems*. West Sussex: John Wiley& Sons Ltd, The Atrium, Souther Gate , Chichester, 2006.

[2] Righter Robert W, *Wind Energy in America: A History*. Oklahoma, United States of America: University of Oklahoma Press, 1996.

[3] Kentfield John A.C., *The Fundamentals of Wind-Driven Water Pumps*. Amsterdam, Netherlands: Gordon and Breach Science Publishers, 1996.

[4] Rajput R.K., *Power System Engineering*, 1st ed. Delhi, India: Laxmi Publication (P) Ltd., 2006.

[5] König K.V., *Wind Energy in Practical Use*, Munichi Udo Pfriemer, 1976.

[6] Wizelius Tore, *Developing Wind Power Projects: Theory And Practice*, 1st ed. London, United Kingdom: Earthscan, 2007.

[7] Golding E.W., *The Generation of Electricity by Windpower*. London: E.&F.N. Spon Ltd., London, 1976.

[8] Twele R. and Gasch J., *Fundamentals, Design, Construction and operation*, XVII, p. 548, 2012.

[9] Leslie Hills R., *Power from Wind: A History of Windmill Technology*. New York, United States Of America: Cambridge University Press, 1996.

[10] Rosenørns Alle. (2012) Danish Wind Industry Association.

[Online]. http://wiki.windpower.org/index.php/Charles_F._Brush

[11] (2013, September) Wind Energy Full Guide.

[Online]. http://freewindenergy.blogspot.com/

[12] Yusuke Kamiyamane. (2012) Norges teknisk-naturvitenskapelige universitet.

[Online]. http://www.ivt.ntnu.no/offshore2/?page_id=394

[13] Johnson Gary L., *Wind Energy System*. Manhattan, Kansas State University , pp. 1-25., 2006.

[14] SAWEP Workshop Wind Atlas for South Africa (WASA), SAWEP Workshop Wind Atlas for South Africa (WASA), Cape Town, 2010.

[15] DICCPP/Energy. (2011, August) KZN energy KZN'S Sustainable Energy Forum. [Online]. http://www.kznenergy.org.za/projects.aspx?cat=92

[16] Net Resources International. (2012) power-technology.com.

[Online]. http://www.power-technology.com/projects/roscoe-wind-farm/

[17] Ohya Y. and Karasudani T., *A Shrouded Wind Turbine Generating High Output Power with Wind-lens Technology*, ISSN 1996-1073, 3, pp. 634–649, 2010.

[18] UIUC Applied Aerodynamics Group. (1995-2012) UIUC Airfoil Coordinates Database.

[Online]. http://www.ae.illinois.edu/m-selig/ads/coord_database.html#N

[19] Chen T.Y and Cheng C.C., *Development of small wind turbines for moving vehicles: Effects of flanged diffusers on rotor performance*, Department of Aerospace Engineering, Tamkang University, Taiwan, ROC, 42, pp. 136–142, 2012.

[20] Tanezaki S., Kuramoto M., and Yamanaka T., *Construction of stand-alone power system using photovoltaic*, NTT Power Build Facil, 37(220), pp. 18-21, 2000.

[21] Karasudani T., Sakura A., Abe K., Inoue M., and Ohya Y., *Development of a shrouded wind turbine with a flanged diffuser*, Journal of Wind Engineering and Industrial Aerodynamics, 96, pp. 524-540, 2008.

[22] Bet F. and Grassmann H., *Upgrading conventional wind turbines*, Renewable Energy, 28, pp. 71-78, 2003.

[23] Matsushima T., Takagi S., and Muroyama S., *Characteristics of a highly efficient propeller type small wind turbine with a diffuser*, Renewable Energy, Research and Development Headquarters, NTT FACILITIES, INC. 2-13-1, Kita-otsuka,Toshima-ku, Tokyo 170-0004, Japan, 31, pp. 1343–1354, 2005.

[24] Ozer I., *Research and development for shrouded wind turbine*, Energy Conversion and Management, 21, pp. 13-48, 1981.

[25] Ozer I., *Compact shrouds for wind turbines*, Energy Conversion, 16, pp. 149-157, 1977.

[26] Foreman K.M, Gilbert B, and Oman R.A., *Diffuser augmentation of wind turbines*, Solar Energy, 20, pp. 305-311, 1978.

[27] Alaydi J. Y., *Modeling and Dynamic Analysis of the Performance of Diffuser Augmented Wind Turbine*, The Islamic University Journal (Series of Natural Studies and Engineering), 18, pp. 85-110, 2010.

[28] Bussel G.J.W, Holten Th. and Kuik G.A.M, *Aerodynamic Research On Tipvane Windturbines*, Delft University of Technology, Netherlands, Research Report LR-355, 1982.

[29] Anantha Subramanian V., Atmanand M., Murali K., Sharuk A., and Sharmila N., *A Diffuser Augmented, Hubless Wind Energy Turbine*, World Renewable Energy Congress (WREC), 8, pp. 1-5, 2004.

[30] Abe K., Nishida M., Sakurai A., Ohya Y., Kihara H., Wada E. and Sato K., *Experimental and numerical investigations of flow fields behind a small wind turbine with a flanged diffuser*, Journal of Wind Engineering and Industrial Aerodynamics, 93, pp. 951-970, 2005.

[31] Kosasih B. and Tondelli A., *Experimental Study of Shrouded Micro-Wind Turbine*, Procedia Engineering, 49, pp. 92-98, 2012.

[32] Kishore R.A., Coudron T., and Priya S., *Small-scale wind energy portable turbine (SWEPT)*, Journal of Wind Engineering and Industrial Aerodynamics, 116, pp. 21-31, 2013.

[33] Aranake A.C., Lakshminarayan V.K. and Duraisamy K., *Computational Analysis of Shrouded Wind Turbine*, Aerospace Sciences Meeting including the New Horizons Forum and Aerospace Exposition, Dallas/Ft. Worth Region, pp. 1-17, 2013.

[34] Angus Tocher J., *Habitat Friendly, Pressure Conversion, Wind Energy Extraction*, Machine US 6887031 B1, 2005.

[35] Howey D.A., Bansal A., and Holmes A.S., *CM-scale air turbine and generator for energy harvesting from low-speed flows*, Solid-State Sensors, Actuators and Microsystems Conference, Transducer International, Denver, pp. 529-532, 2011.

[36] Walter Presz M. and Michale Werle J., *Wind Turbine With Mixer and Ejector*, Mechanical US008021100B2, September 20, 2011.

[37] Foreman K.M., *Preliminary Design and Economic Investigations of Diffuser Augmented Wind Turbines (DAWT)*, Springfield, 1980.

[38] Wang F., Bai L., Fletcher J., Whiteford J., and Cullen D., *The methodology for aerodynamic study on a small domestic wind turbine with scoop*, Journal of Wind Engineering and Industrial Aerodynamics, 96, pp. 1-24, 2007.

[39] Hasegawa M., Ohya Y., and Kume H., *Numerical studies of flows around a wind turbine*

equipped with a flanged diffuser shroud by using an actuator-disc model, The Fourth International Symposium on Computational Wind Energy (CWE2006), Yokohama, 2006.

[40] Ohya Y.,Karasudani T. and Zang X., *A Shrouded Wind Turbine Generating High Output Power with Wind-lens Technology*, Energies, 3, pp. 634-649, 2010.

[41] Takahashi S., Hata Y., Ohya Y., Karasudani T. and Uchida T., *Behavior of the Blade Tip Vortices of a Wind Turbine Equipped with a Brimmed-Diffuser Shroud,* Research Institute for Applied Mechanics, 5, pp. 5229-5242, 2012.

[42] Flay R.G.J, Mallinson G.D, Richards P.J, and Phillips D.G, *Computational Modelling Of Diiuser Design For A Diffuser Augmented Wind Turbine*, 13th Australasian Fluid Mechanics Confrence, Melbourne, Australia, 1998.

[43] Chen S. H. W. and Hsiung S., *The Studfy of Interference Effect for Cascaded Diffuser Augmented Wind Turbines,* The Seventh Asia-Pacific Conference on Wind Engineering, Taipei, Taiwan, 2009.

[44] Jamieson P., *A Shrouded Rotor, Innovation in Wind Turbine Design*. West Susex: John Wiley & Sons Ltd, pp. 256-258, 2011.

[45] Paul G., *Wind Power: Renewable Energy for Home, Farm, and Business*, 2nd ed. White River Junction, U.S.A: Chelsea Green Publishing Company, 2004.

[46] Magdi Ragheb, *Theory of Wind Machine*., Department of Nuclear, Plasma and Radiology Engineering, Department of Aerospace Engineering in University of Illinois at Urban-Champaign, 216 TalbotLaboratory, 2010.

[Online]. http://cdn.intechweb.org/pdfs/16242.pdf

[47] James Manwell F, Jon McGowan G., and Anthony Rogers L., *Wind Energy Explained: Theory, Design and Application*. West Sussex: John Wiley & Sons Ltd, 2009.

[48] Jon McGowan G, Anthony Rogers L James Manwell F, *Wind Energy Explained: Theory, Design and Application*. West Sussex: John Wiley & Sons Ltd, 2009.

[49] Answers. (2012) Answers.

[Online]. http://www.answers.com/topic/airfoil

[50] Cervera R.A., Arroyo R.L., and Castro R.R., *Interface for the Modeling and Simulation of a Airfoil of Turbine of Wind*, 2006.

[51] Jacobs N.E., Ward E.K, and Pinkerton M.R., *The charactristics of 78 related airfoil section*

from test in the variable- density wind tunnel, Washington D.C, 1935.

[52] Sproles W.D., Hill S.A., Brooks W.C., and Ladson C., *Computer Program To Obtain Ordinates for NACA Airfoil*, Hampton, Verginia, 1996.

[53] Kundu P.K., Cohen I.M., and Dowling D.R., *Fluid Mechanics*. Waltham: Elsevier Inc Academic Press, 2012.

[54] Tu J., Yeoh G.H., and Liu C., *Computational Fluid Dynamics: A Practical Approach*. Waltham: Butterworht-Heinemann, 225 Wayman Street, Waltham, MA 02451, USA, 2008.

[55] Johnson Richard W., *The Hand Book Of Fluid Dynamics*. Boca Raton, Florida: CRC Press LLC, 1998.

[56] Daniel Valentine T. T., Carpenter P. W., Steven Collicott H., and Houghton E. L., *Aerodynamics for Engineering Students*. Waltham: Butterworth-Heinemann An imprint of Elsevier Science, 2003.

[57] Ira Cohen M. and Pijush Kundu, *Fluid Mechanics*. San Diego: Elsevier Academic Press, 2004.

[58] Taura L.S., Ishiyaku I.B., and Kawo A.H, *The use of a continuity equation of fluid mechanics to reduce the abnormality of the cardiovascular system: A control mechanics of the human heart,* Journal of Biophysics and Structural Biology, 4, 1, pp. 1-12, 2012.

[59] Bernard Stanford Massey and John Ward Smith, *Mechanics of Fluids*. Cheltenham: Nelson Thornes Ltd., 2001.

[60] Nelson Vaughn, *Storage*, Introduction to Renewable Energy. Boca Raton: CRC Press, Taylor and Francis Group, LLC, p. 275, 2011.

[61] David Anderson J., *Governing Equation of Fluid Dynamics*. Heidelberg: Springer-Verlag, 2009.

[62] Hansen M.O.L, Sorensen J.N., Voutsinas S., Sørensen N., and Madsen H.Aa. , *State of the art in wind turbine aerodynamics and aeroelasticity,* Progress in Aerospace Sciences , pp. 285-330, December 2006.

[Online]. www.flodesign.org/pdf/AIAADWTTechNote,052407.pdf

[63] ESI-CFD Support Team. (2012, December) esi CFD FAQ.

[Online]. http://www.esi-cfd.com/faq/index.php?action=artikel&cat=4&id=156&artlang=en&highlight=Turbulence+Guidelines

[64] Ping W.Z. and Gu Y. T., *Prediction of Structural Integrity, Robustness And Service Life Using Advanced Finite Element Methods:,* International Journal of Computational Methods, 4, 8, pp. 787-800, September 2010.

[65] Nate E O, Idelsohn S R., Del Pin F., and Aubry R., *The Partical Finite Element Method :An Overview,* International Journal of Computational Methods, 1, 2, pp. 267-307, February 2004.

[66] Korunovic N., Trajanovic M., Stojkovic M., Misic D., and Milovanovic J., *Finite Element Analysis of a Tire Steady Rolling on the Drum and Comparison with Experiment,* Journal of Mechanical Engineering, 57, pp. 888-897, Septemeber 2011.

[67] Sivarasu S. and Mathew L., *Biophysical Reviews and Letters*, Structural Response Of A Novel High Flexion knee (SS316-UHMWPE)Used In Total Knee Arthroplasty Using Finite Element Analysis, 4, 3, pp. 289-298, March 2009.

[68] Lombargo F.S. and Lang P.R., *Atmospheric turbulence,Metrological Modeling and Aerodynamics,* Nova Publisher, Inc. 400 Oser Ave Suite 1600 Hauppauge NY 11788-3619 USA , 2011.

[69] Foreman K M, *Preliminary Design and Economic Investigations of Diffuser Augmented Wind Turbines (DAWT),* Midwest Research Institute, Colorado, Final Report SERI/TR-98073-1B, 1981.

Appendix A: Betz Derivation

To calculate the limit of wind energy or energy contained in wind E is given by:

$$E = \frac{1}{2} m v_{\infty}^2 \tag{A.1}$$

$$E = \frac{1}{2} \rho A v_{\infty}^3 \quad (\because m = A \times v_{\infty}) \tag{A.2}$$

where:

ρ	Density	[kg/m^3]
A	Area of the rotor	[m^2]
v_{∞}	Normal wind velocity	[m/s]
m	Mass	[kg]

The wind energy is directly proportional to cube of velocity. From equation A.2 it is observed that:

$E \propto v_{\infty}^3$

The relationships above suggest that a slight change in speed will greatly or substantially change energy.

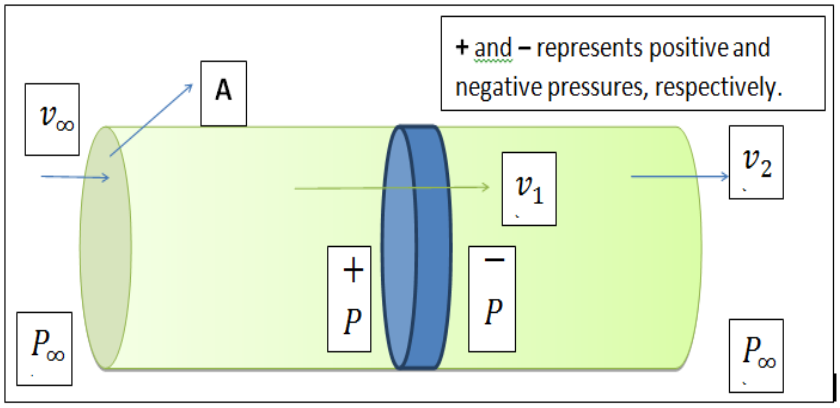

Figure A-0-1 Model of an actuator disk with zero leakage around its edge

Bernoulli's equation is expressed as follows:

$$\frac{1}{2}\rho v^2 + \rho g z + p = constant \tag{A.3}$$

$$\frac{1}{2}\rho A v_\infty^2 + P_\infty = \frac{1}{2}\rho v_1^2 + {}^{+}_{P} \tag{A.4}$$

$$\frac{1}{2}\rho A v_2^2 + P_\infty = \frac{1}{2}\rho v_1^2 + {}^{-}_{P} \tag{A.5}$$

where:

P_∞	Atmospheric pressure	[kg/m s^2]
${}^{+}_{P}$	Pressure in front of disk	[kg/m s^2]
${}^{-}_{P}$	Pressure behind disk	[kg/m s^2]
v_1	Velocity before disk	[m/s]
v_2	Velocity after disk	[m/s]

Solving equations (A.4) and (A.5) gives:

$$\langle({}^{+}_{P} - {}^{-}_{P}) = \frac{1}{2}\rho\,(v_\infty^2 - v_2^2)\rangle \tag{A.6}$$

Equation (A.6) represents the pressure difference.

Thrust F is given by:

$$F = P \times A \tag{A.7}$$

Or

$$F = \frac{1}{2}\rho A\,(v_\infty^2 - v_2^2) \tag{A.8}$$

Thrust is also given by change in momentum as:

$$F = m(v_\infty - v_2) = \rho A v (v_\infty - v_2) \tag{A.9}$$

Equating equations (A.8) and (A.9) we obtain:

$$v_{avg} = \frac{1}{2}\,(v_\infty + v_2) \tag{A.10}$$

From equation (A.10) it is clear that the velocity of air which passes through the wind turbine is the average velocity of the infinite distance before and after.

Betz Derivation

The ideal rotor is taken as stationary and is placed in a moving wind atmosphere as shown in Figure A-0-1. Some points to keep in mind before calculating the maximum power that can be extracted from the wind are as follows:

- If the rotor disk provides no hindrance or obstacles in the flow of wind than $v_\infty = v_1 = v_2$. In this case no power will be extracted; and
- If the rotor disk provides full obstruction like a wall in the flow of the wind than $v_1 = 0$. In this case power extracted will also be zero.

To find the value in between ($v_\infty > a > 0$) for maximum power output we define an axial interference factor "a". Differentiating the power output with respect to a and maximizing the value will give the maximum power that can be extracted from the wind.

$$v = v_\infty(1 - a) \tag{A.11}$$

From equation (A.10) we know that the velocity that should pass the rotor disk should be the average of the before and after the disk velocity so therefore$v = v_{avg}$. Equating this we get:

$$v_\infty(1-a) = \frac{1}{2}\,(v_\infty + v_2) \tag{A.12}$$

or

$$v_2 = v_\infty(1-2a) \tag{A.13}$$

where:

v_∞	Normal wind velocity	[m/s]
v_∞	Wind velocity at entrance	[m/s]
v_∞	Wind velocity at outlet	[m/s]
a	Interference factor	[-]

Power extracted is the drop in the kinetic energy of the wind:

$$E = \frac{1}{2}\dot{m}(v_1^2 - v_2^2) \tag{A.14}$$

Also

$$P = \frac{1}{2}\rho A v(v_1^2 - v_2^2) \tag{A.15}$$

where:

E	Kinetic energy of the wind	[kg m^2/s^2]
P	Power	[kg m^2/s^3]
ρ	Density of air	[kg/m^3]

Substituting the value of equation (A.11) and (A.13) into equation (A.15) we get:

$$P = \frac{1}{2}\rho A v_\infty (1-a)[v_\infty^2 - v_\infty^2(1-2a)^2] \quad \text{(A.16)}$$

$$= \frac{1}{2}\rho A v_\infty^3 [4a - 8a^2 + 4a^3] \quad \text{(A.17)}$$

By differentiating P with respect to a we get:

$$\frac{dP}{da} = 3a^2 - 4a + 1 = 0 \quad \text{(A.18)}$$

Solving the polynomial equation (2.19) for the value of a we get $a = 1, \frac{1}{3}$ since 1 is not acceptable as per above mentioned condition for a so maximum value for P ,$(a = \frac{1}{3})$. Substituting this value of a in the results of equation (2.18) we get:

$$P_{max} = \frac{1}{2}\rho A v_\infty^3 \times \frac{16}{27} \quad \text{(A.19)}$$

$$P_{max} = P_{wind} \times \frac{16}{27} \qquad \because P_{wind} = \frac{1}{2}\rho A v_\infty^3 \quad \text{(A.20)}$$

where:

P_{max}	Maximum power extracted	[kg m^2/s^3]
P_{wind}	Power contained in wind	[kg m^2/s^3]

$$F = C_F \rho A (v_\infty - u)^2 \quad \text{(A.21)}$$

where:

F	Force applied by the wind on the disk	[kg m/s^2]
C_F	Force coefficient	[-]

Power extracted is given by:

$$P = C_F \rho A (v_\infty - u)^2 u \quad \text{(A.22)}$$

To find the value of u at which the maximum power output is obtained differentiate the equation (A.22) with respect to u.

$$\frac{dP}{du} = C_F \rho A[v_\infty^2 - 4v_\infty u + v^2] \quad \text{(A.23)}$$

Differentiating the above equation (A.22) we get two possible values of $u = 1, \frac{1}{3}$. as above mentioned 1 is not acceptable because power output will become zero so $\frac{1}{3}$ is taken into consideration.

Substituting the value of $u = \frac{1}{3}$ in equation (A.22) we get:

$$P_{max} = \frac{1}{2}\rho v_\infty^3 \times \frac{8}{27} \quad \text{(A.24)}$$

$$P_{thrust} P_{wind} \times \frac{8}{27} \qquad \because P_{wind} = \frac{1}{2}\rho A v_\infty^3 \quad \text{(A.25)}$$

The reference power for the Betz efficiency calculation is the power in a moving fluid in a cylinder with cross sectional area and velocity and can be expressed as follows:

The power coefficient $C_p = \frac{P}{P_{wind}}$ has a maximum value of:

$$C_p = \frac{16}{27} = 0.593 \quad \text{(A.26)}$$

Appendix B: CFD Results

1. Collection of Velocity filed Profiles for multiple case studies.
2. Corresponding velocity graphs.

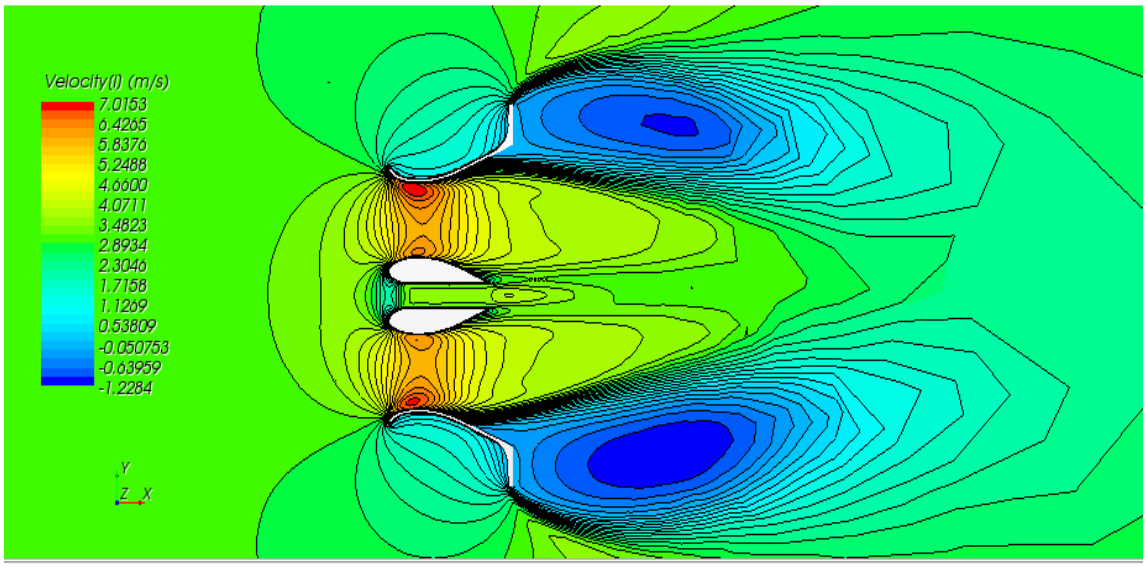

Figure B-0-1 Velocity field profile for 3m/s

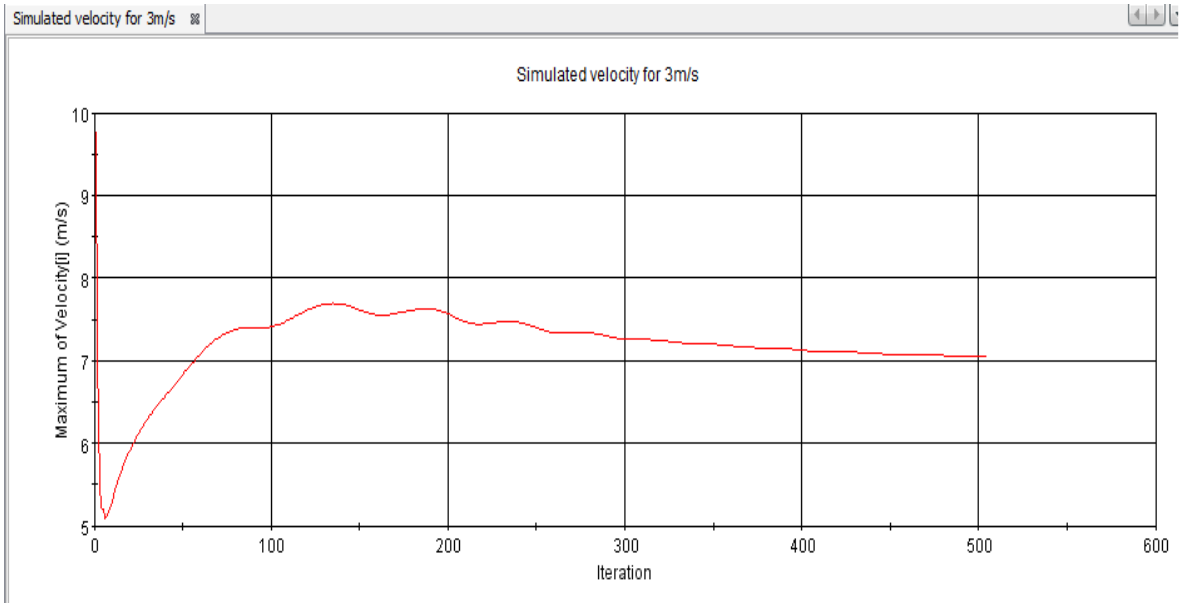

Figure B-0-2 Simulated velocity graph at 3m/s

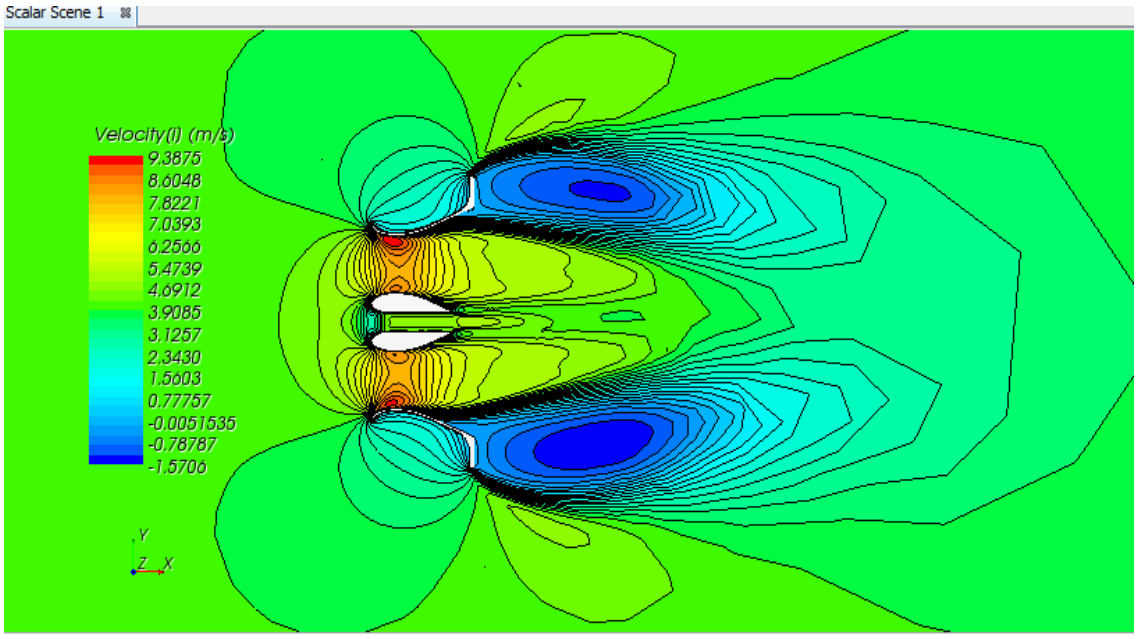

Figure B-0-3 Velocity field profile for 4m/s

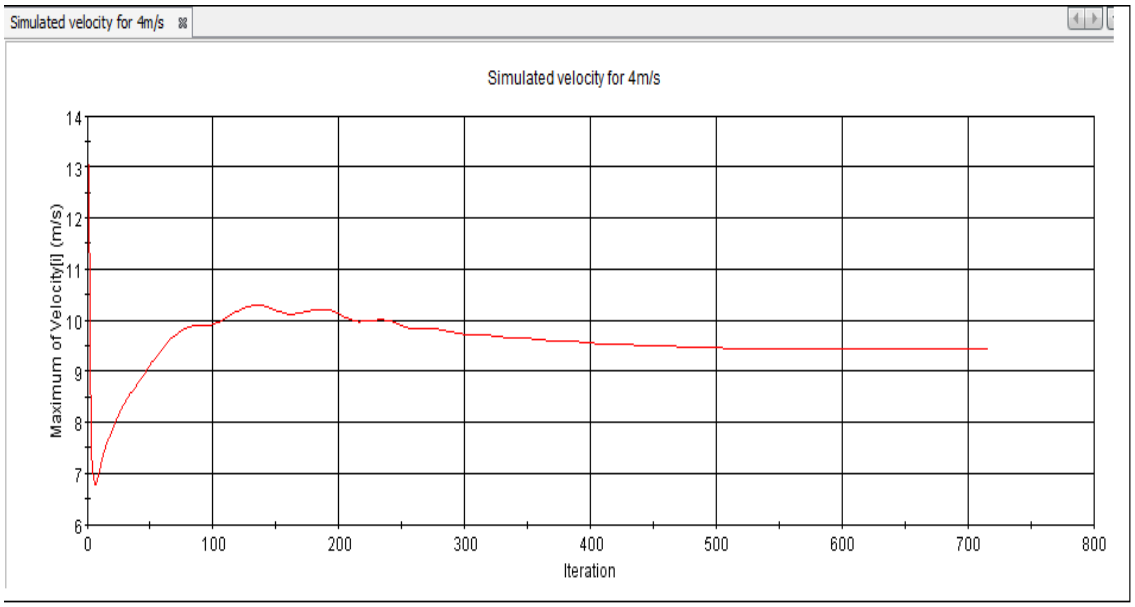

Figure B-0-4 Simulated velocity graph at 4m/s

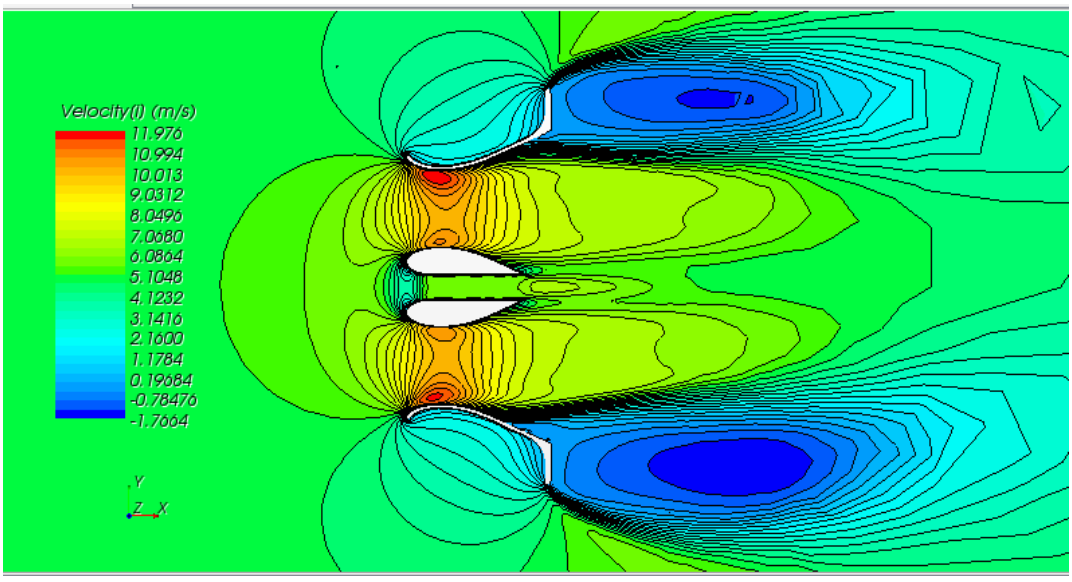

Figure B-0-5 Velocity field profile for 5m/s

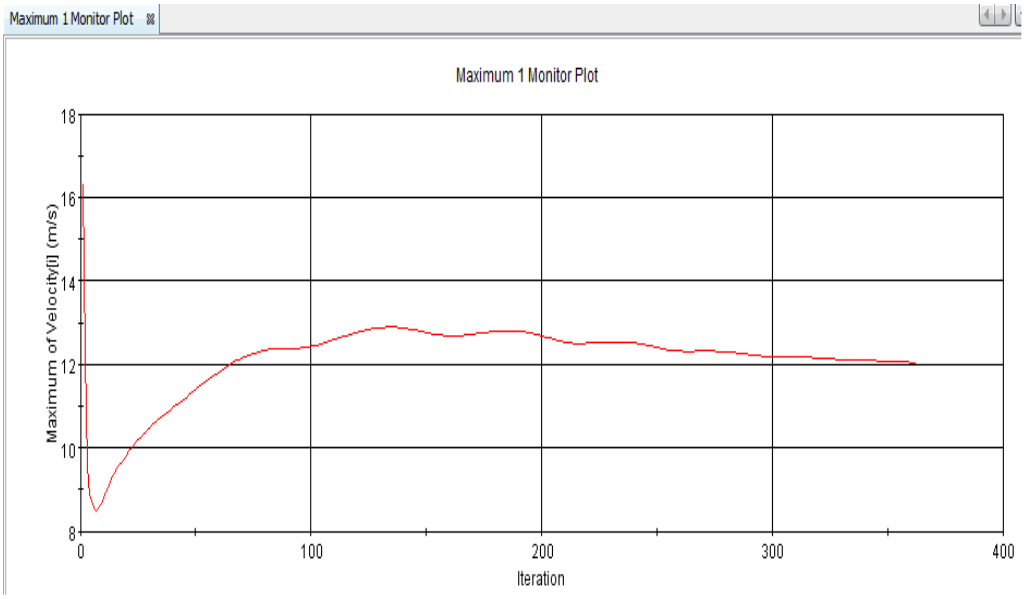

Figure B-0-6 Simulated velocity graph at 5m/s

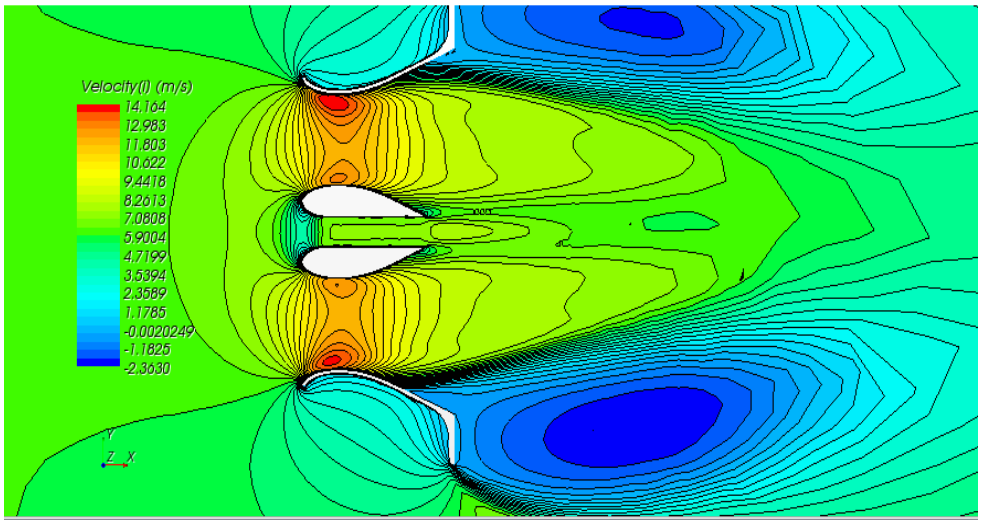

Figure B-0-7 Velocity field profile for 6m/s

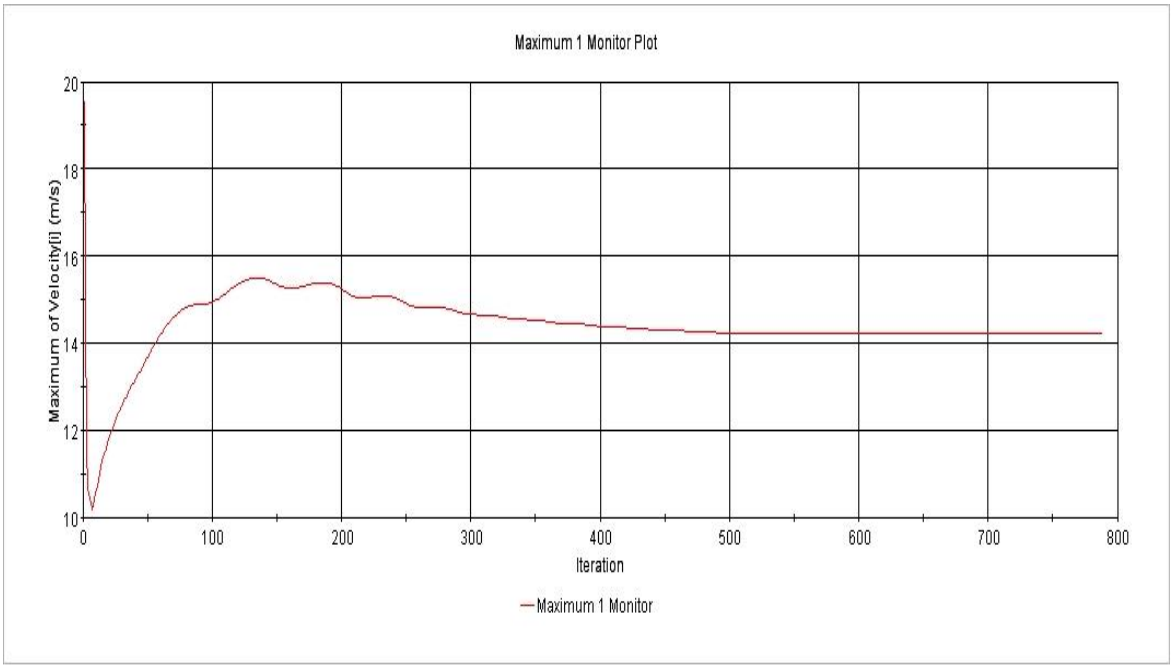

Figure B-0-8 Simulated velocity graph at 6m/s

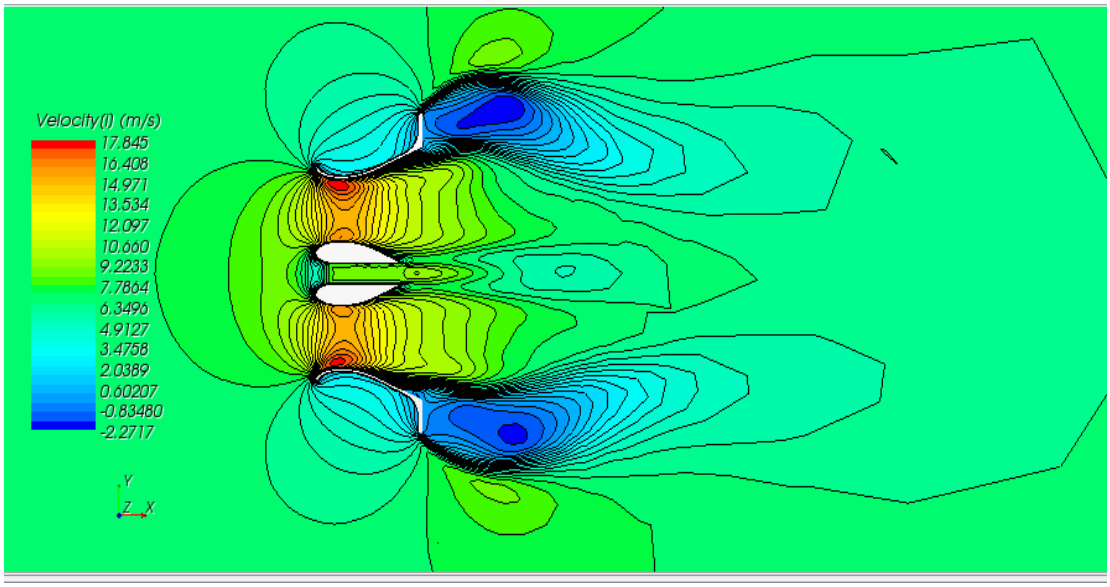

Figure B-0-9 Velocity field profile for 7m/s

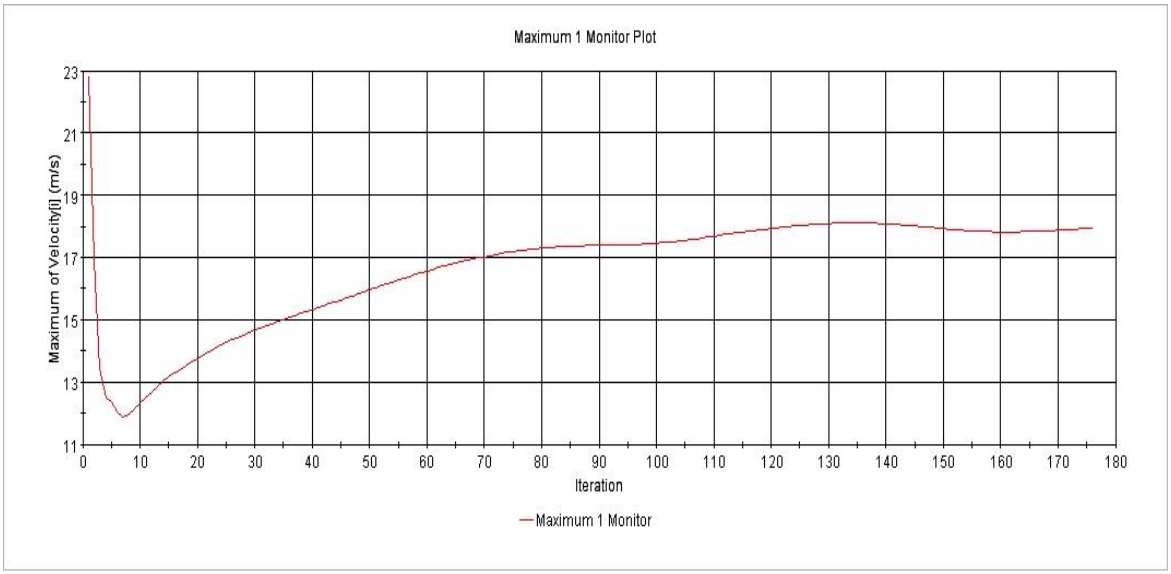

Figure B-0-10 Simulated velocity graph at 7m/s

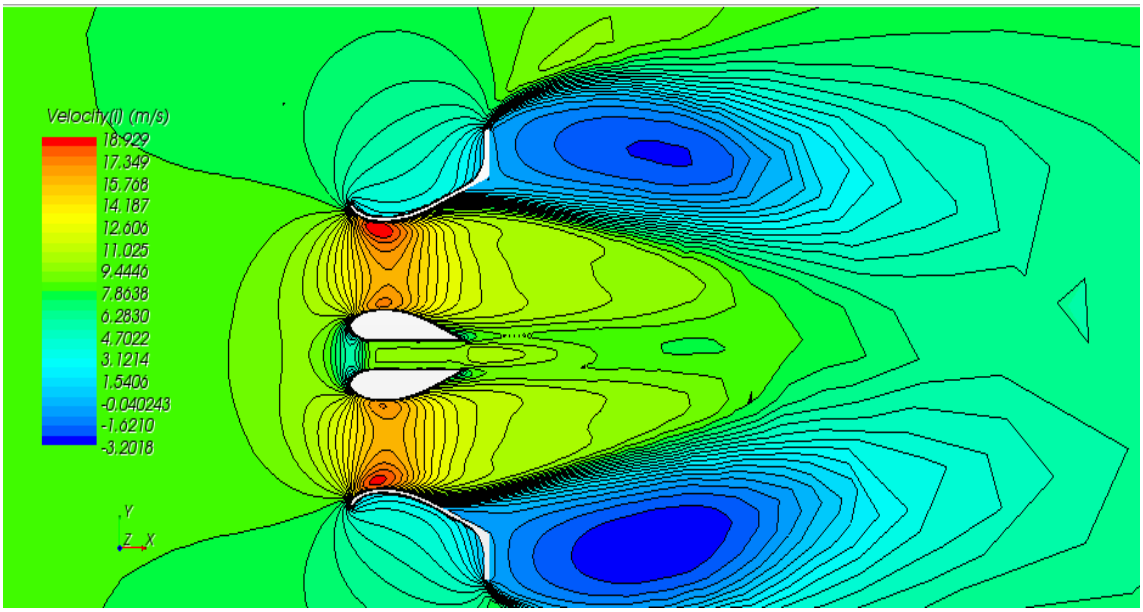

Figure B-0-11 Velocity field profile for 8m/s

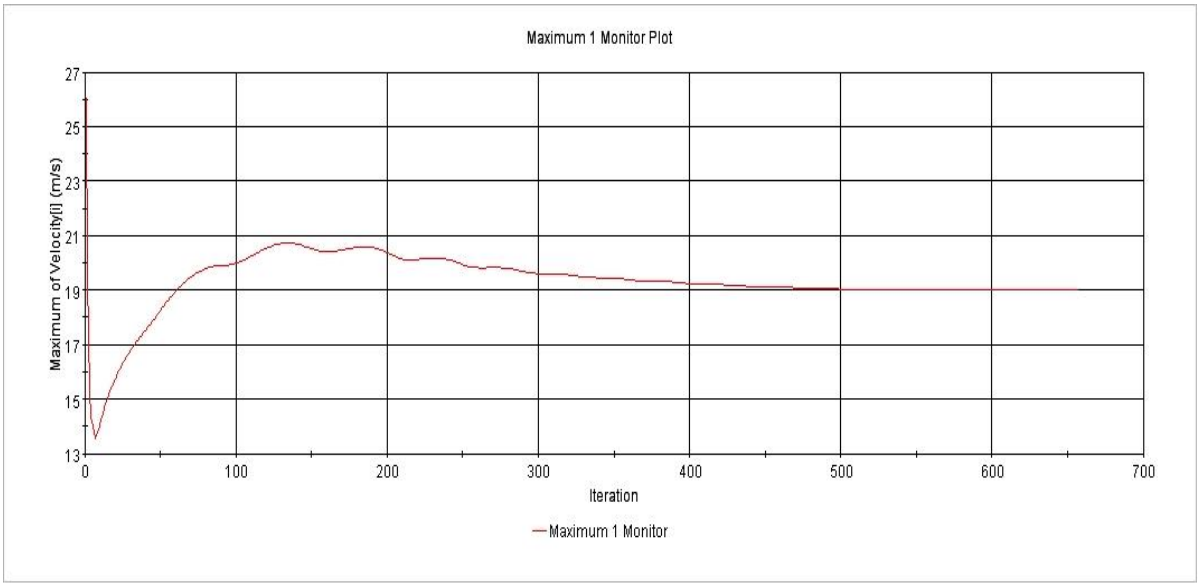

Figure B-0-12 Simulated velocity graph at 8m/s

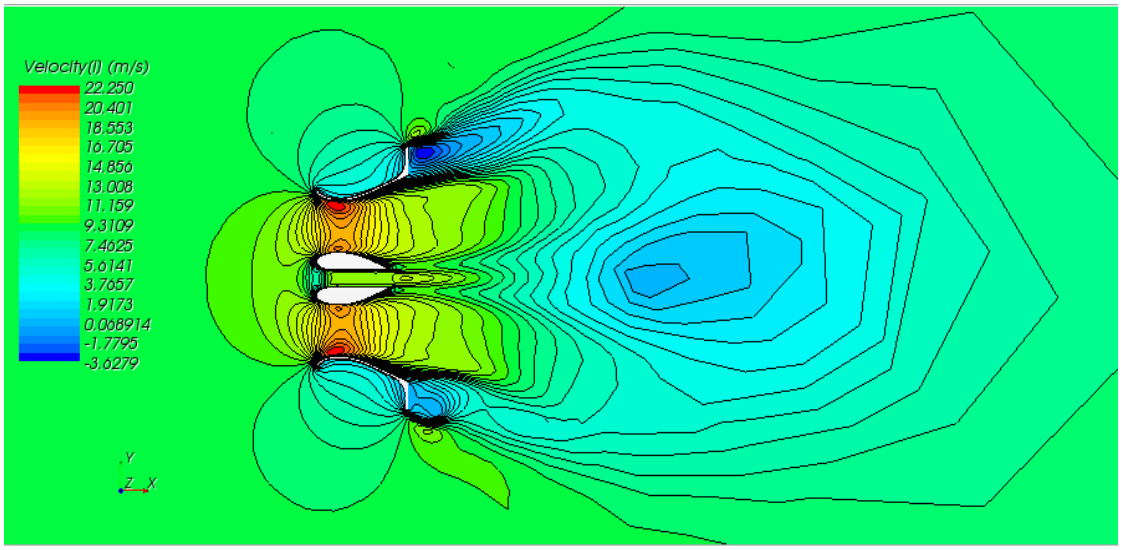

Figure B-0-13 Velocity field profile for 9m/s

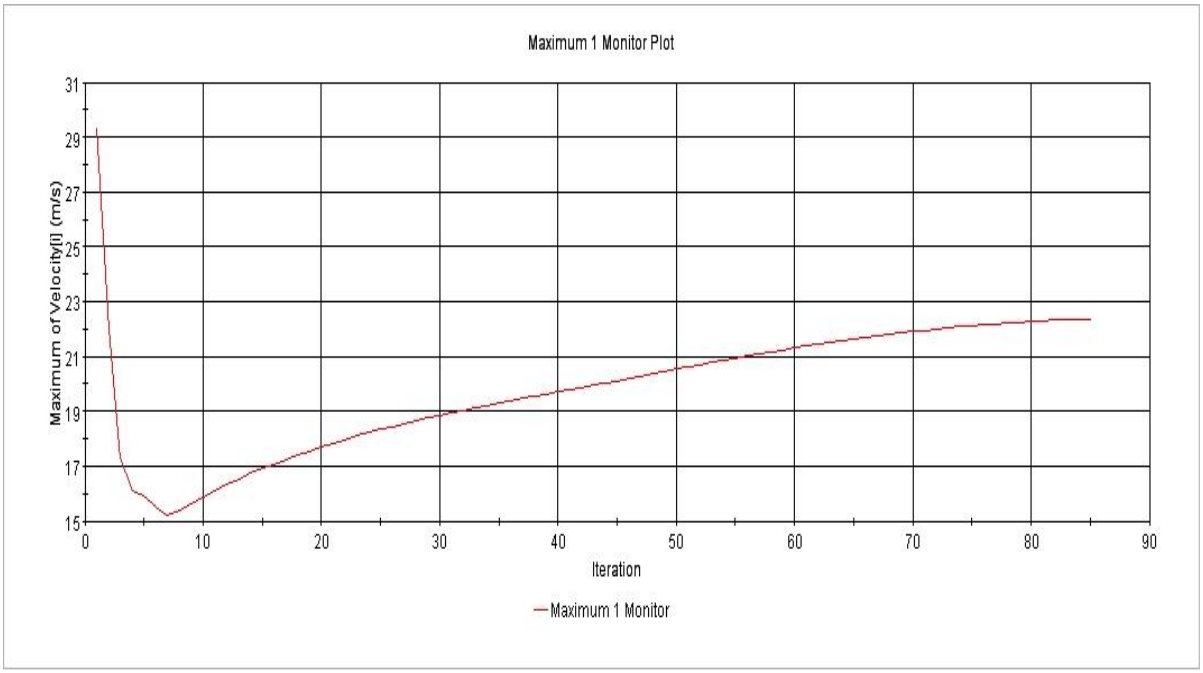

Figure B-0-14 Simulated velocity graph at 9m/s

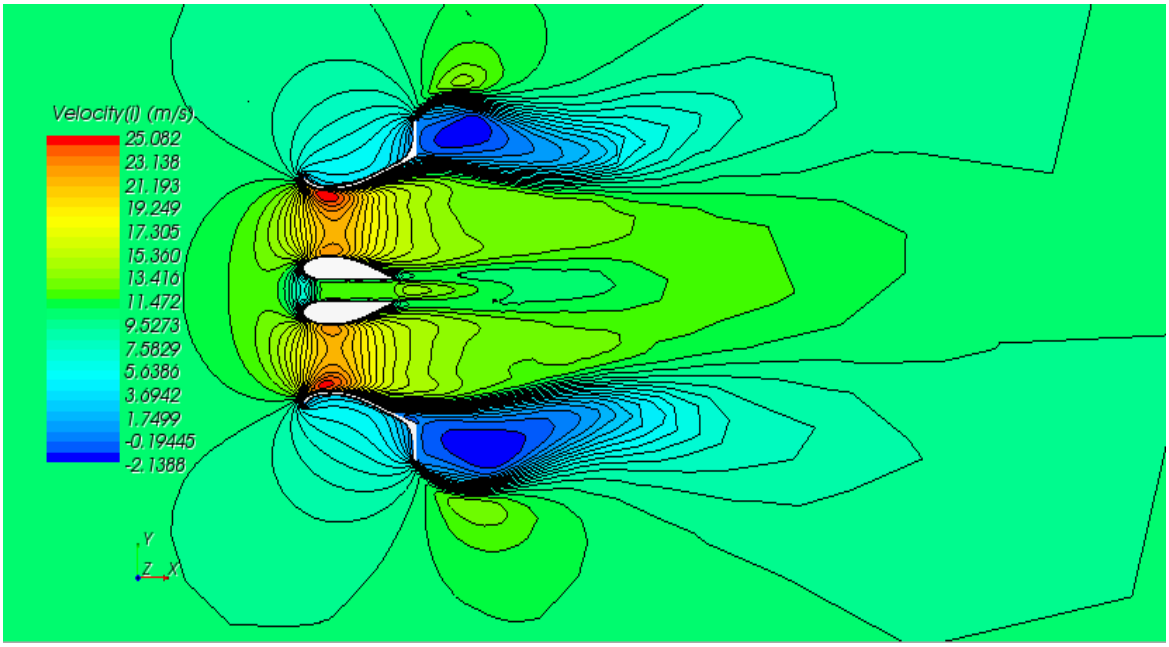

Figure B-0-15 Velocity field profile for 10m/s

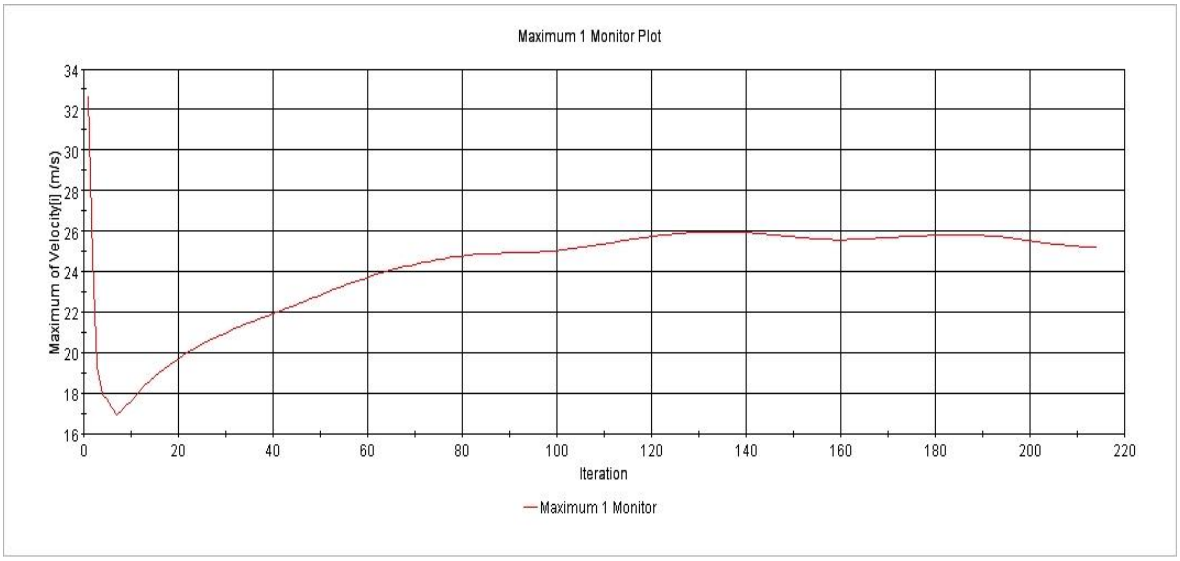

Figure B-0-16 Simulated velocity graph at 10m/s

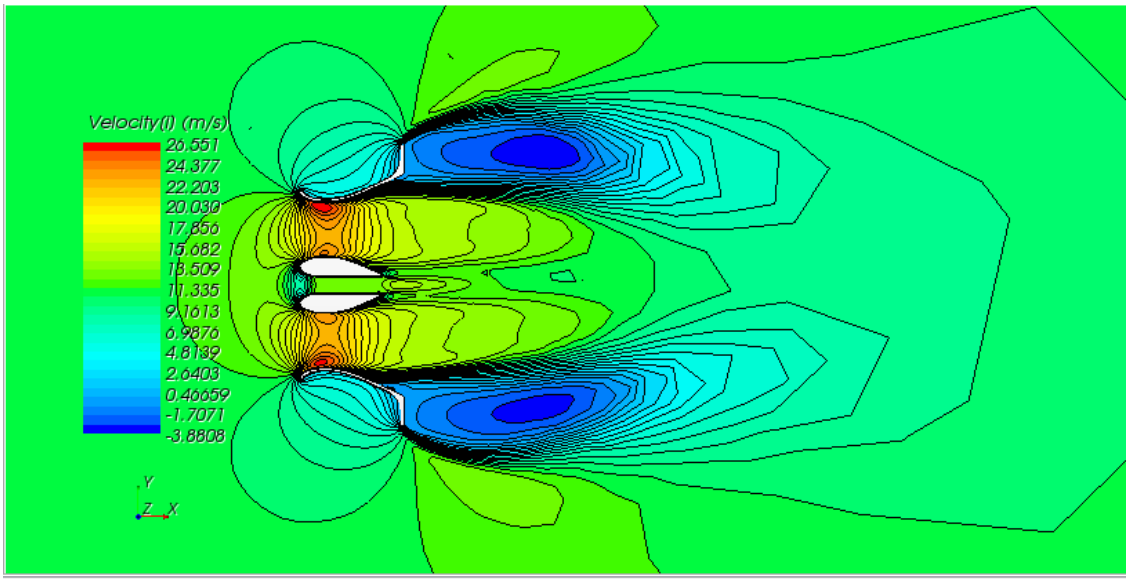

Figure B-0-17 Velocity field profile for 11m/s

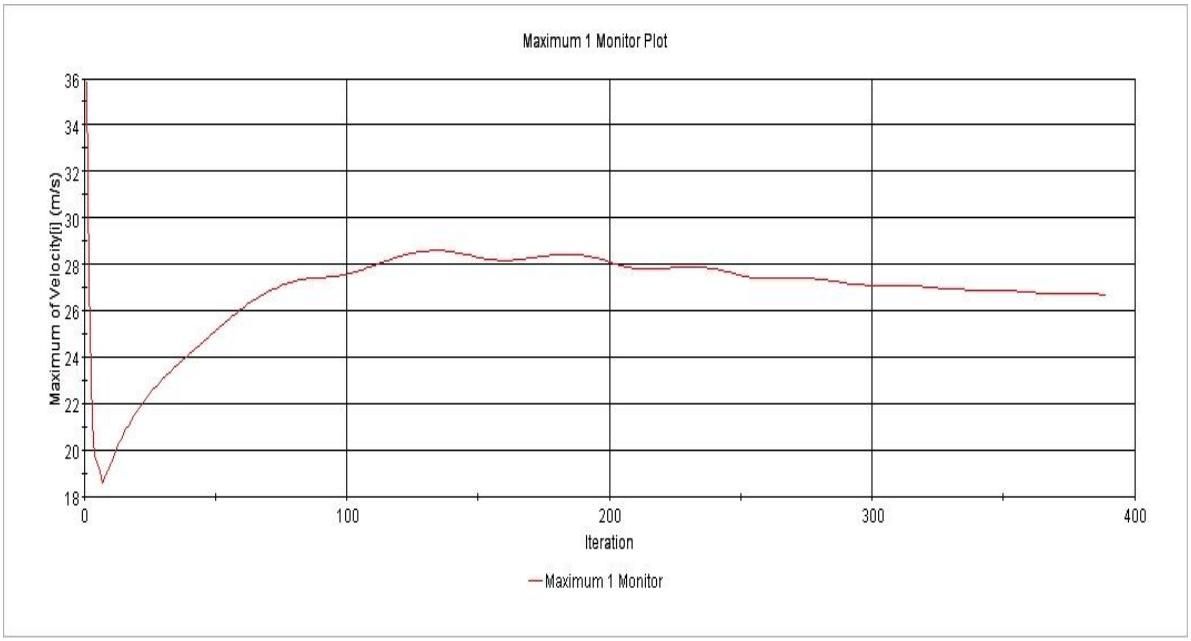

Figure B-0-18 Simulated velocity graph at 11m/s

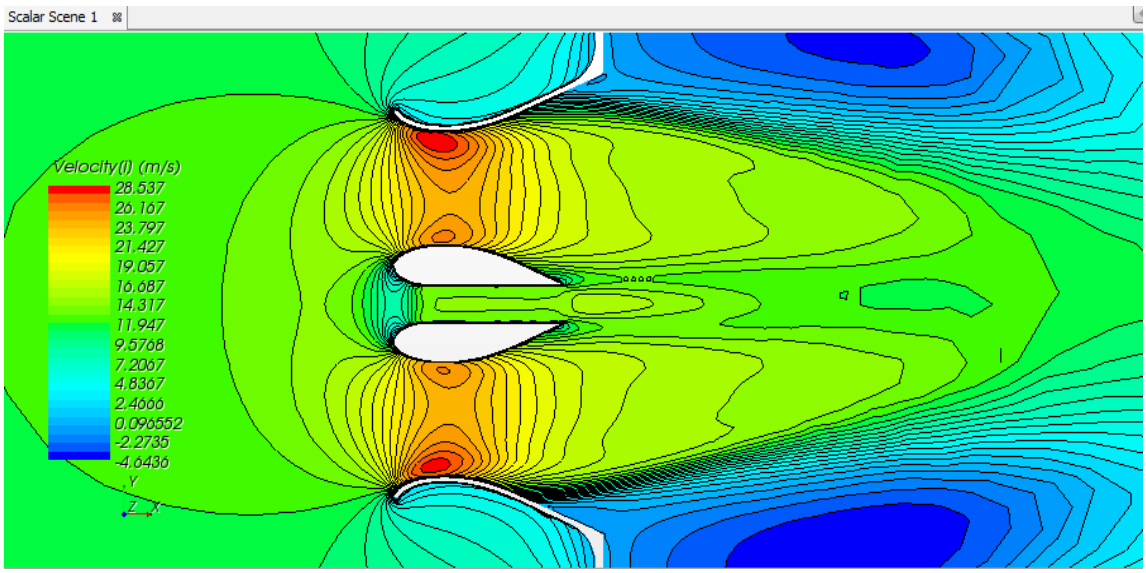

Figure B-0-19 Velocity field profile for 12m/s

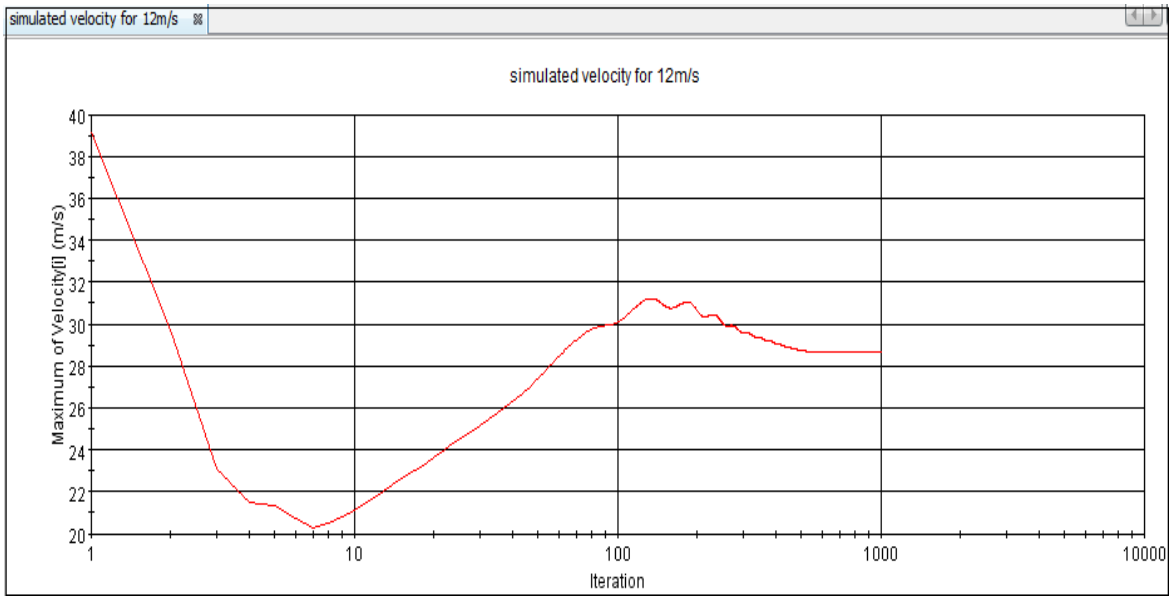

Figure B-0-20 Simulated velocity graph at 12m/s

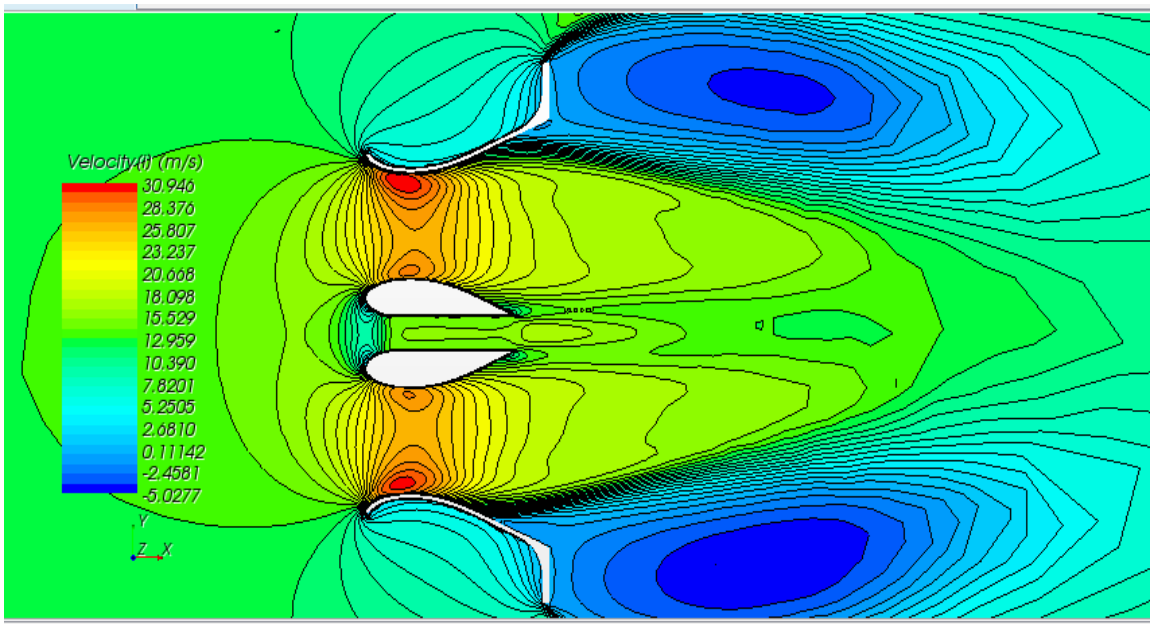

Figure B-0-21 Velocity field profile for 13m/s

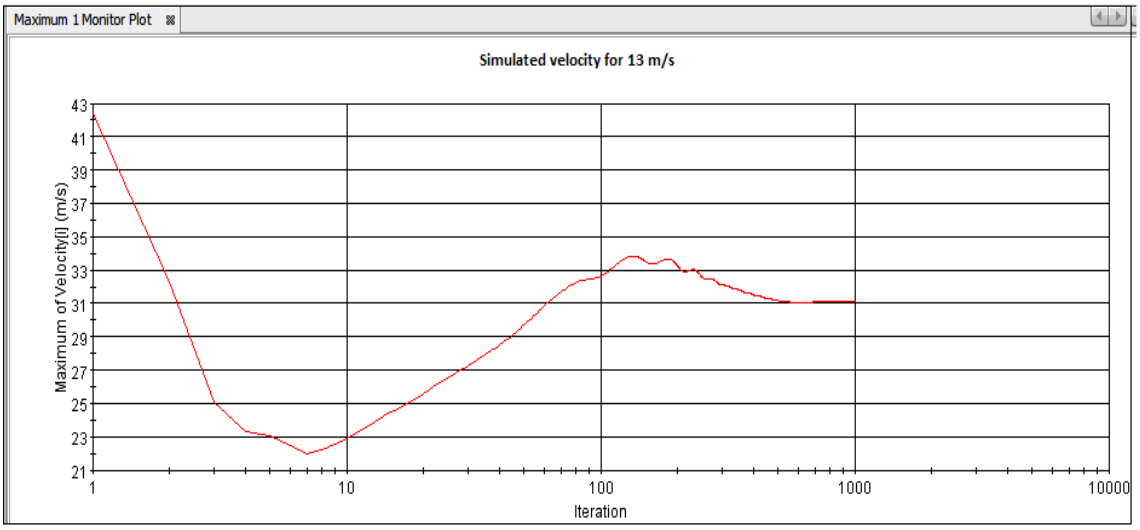

Figure B-0-22 Simulated velocity graph at 13m/s

Appendix C: FEA Results

FEA results

- Von Mises Stress
- 1st Principal stress
- 3rd Principal Stress
- Safety Factor
- Displacement

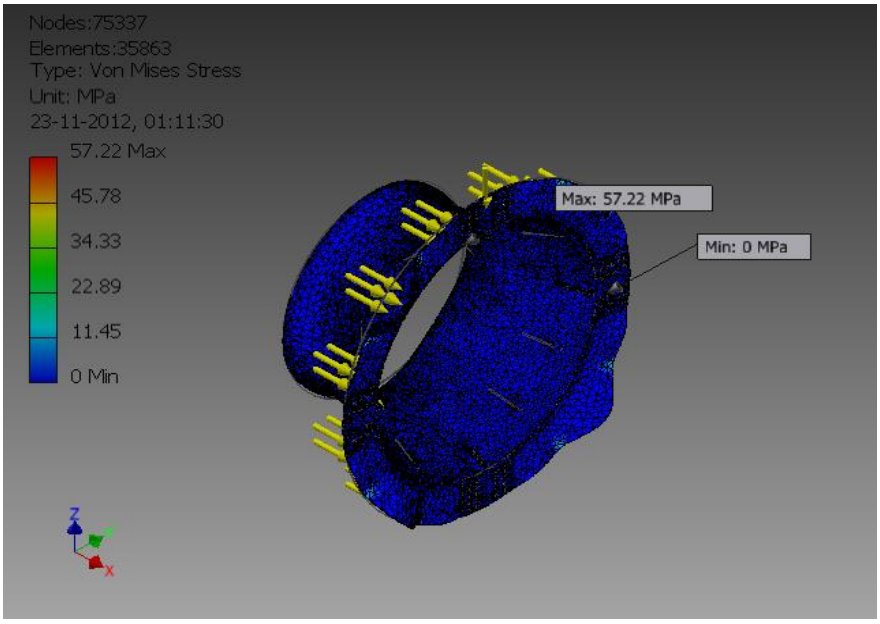

Figure C-0-1 Von Mises Stress of outer shroud

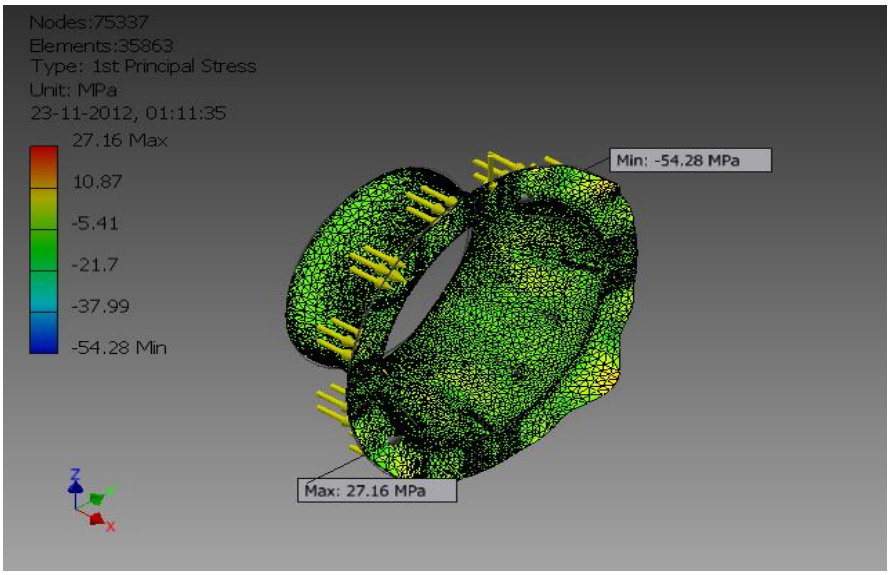

Figure C-0-2 1st Principal stress

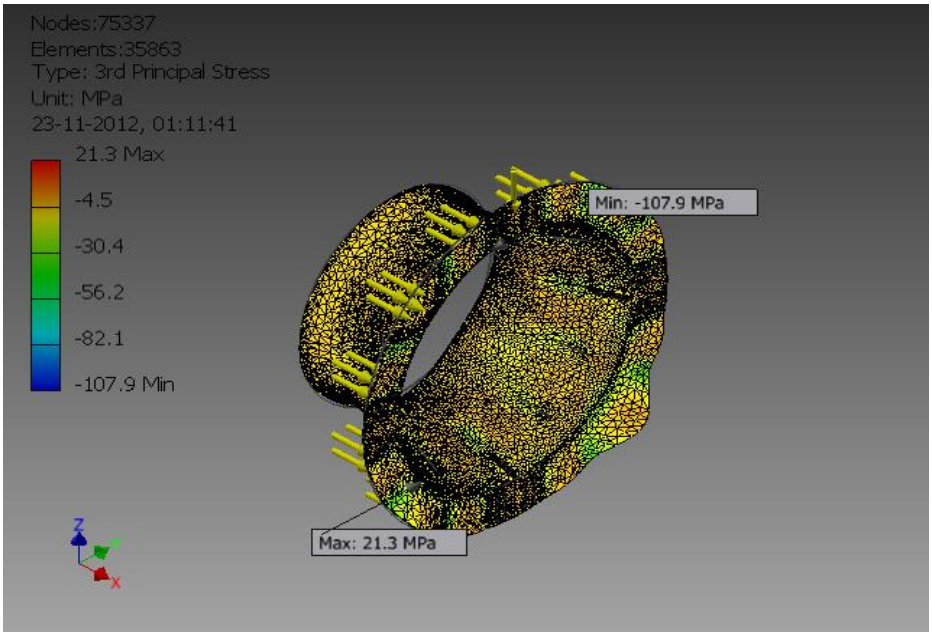

Figure C-0-3 3rd Principal Stress

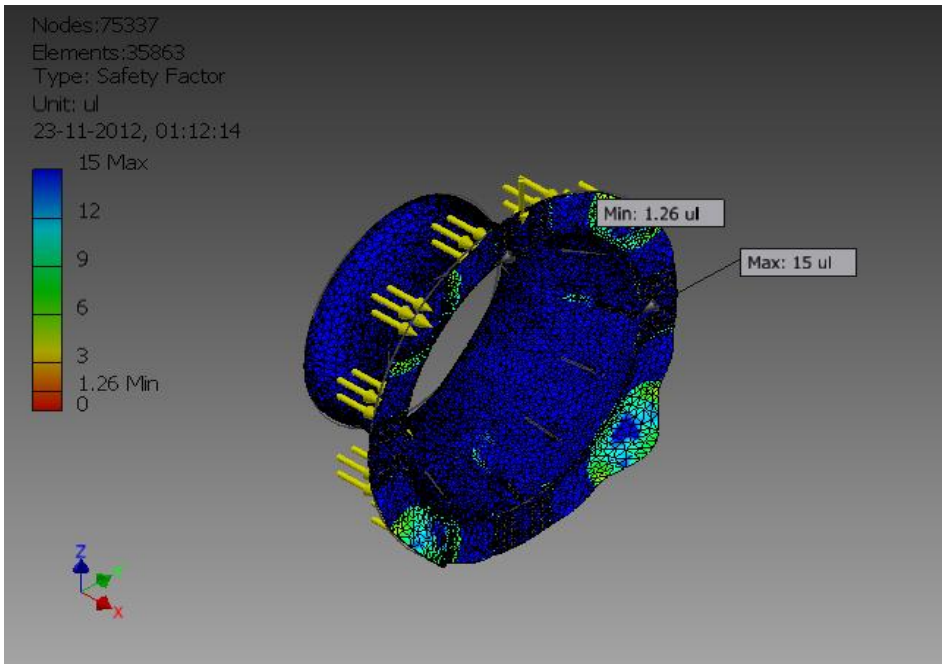

Figure C-0-4 Safety factor

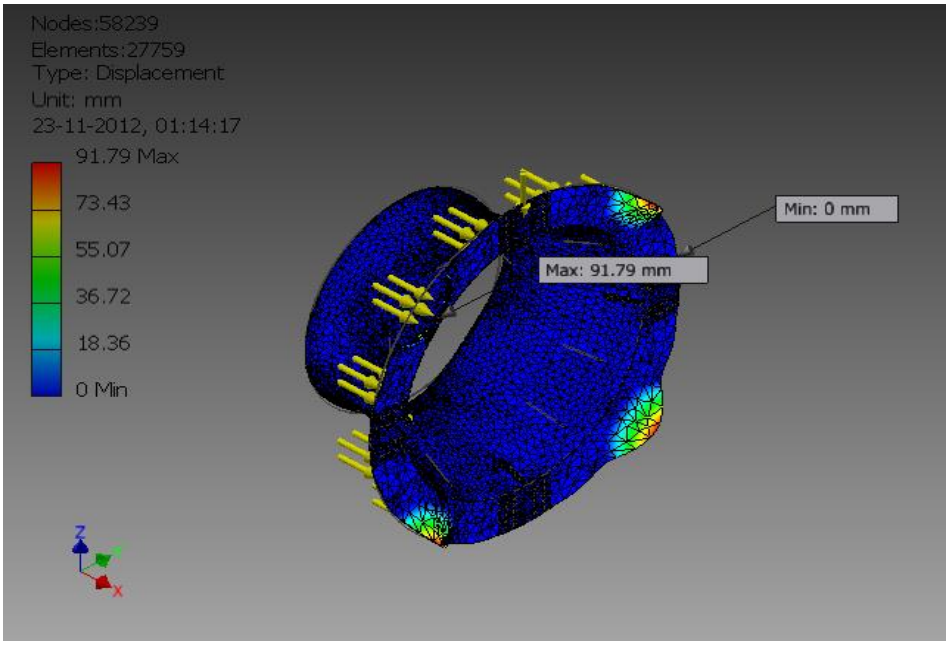

Figure C-0-5 Displacement

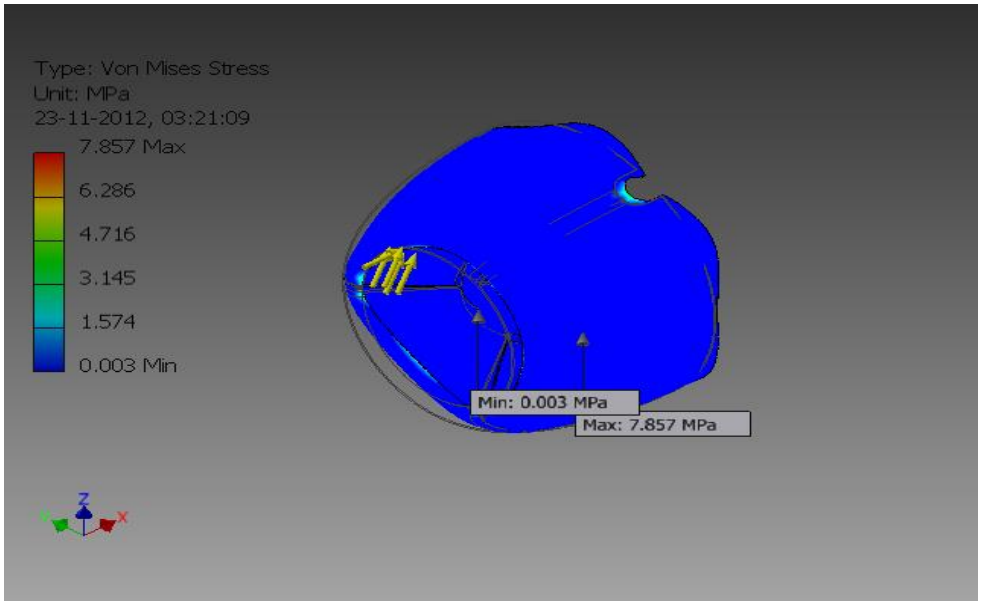

Figure C-0-6 Von Mises Stress lower shroud

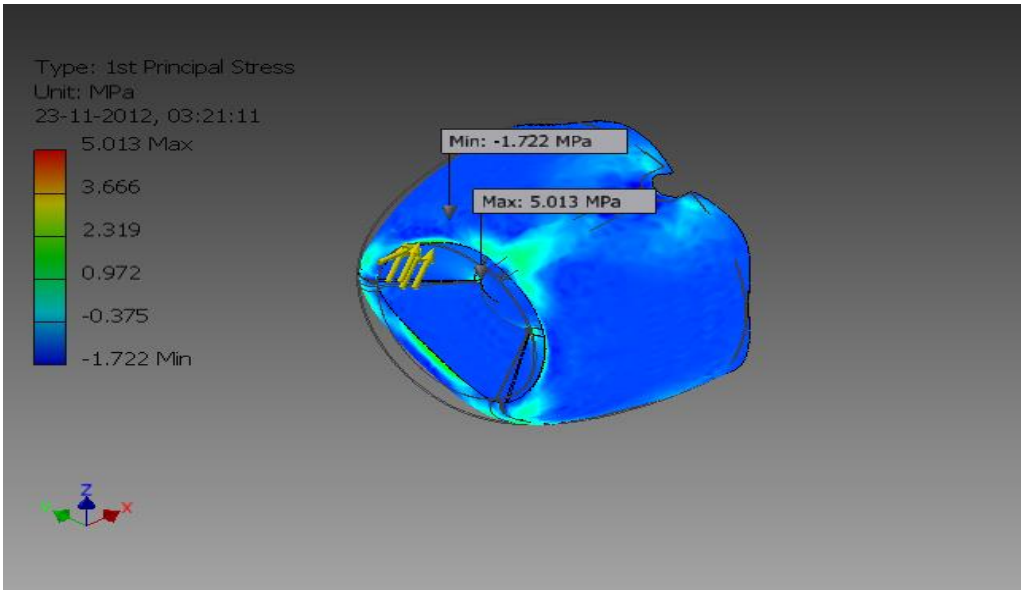

Figure C-0-7 1st Principal stress

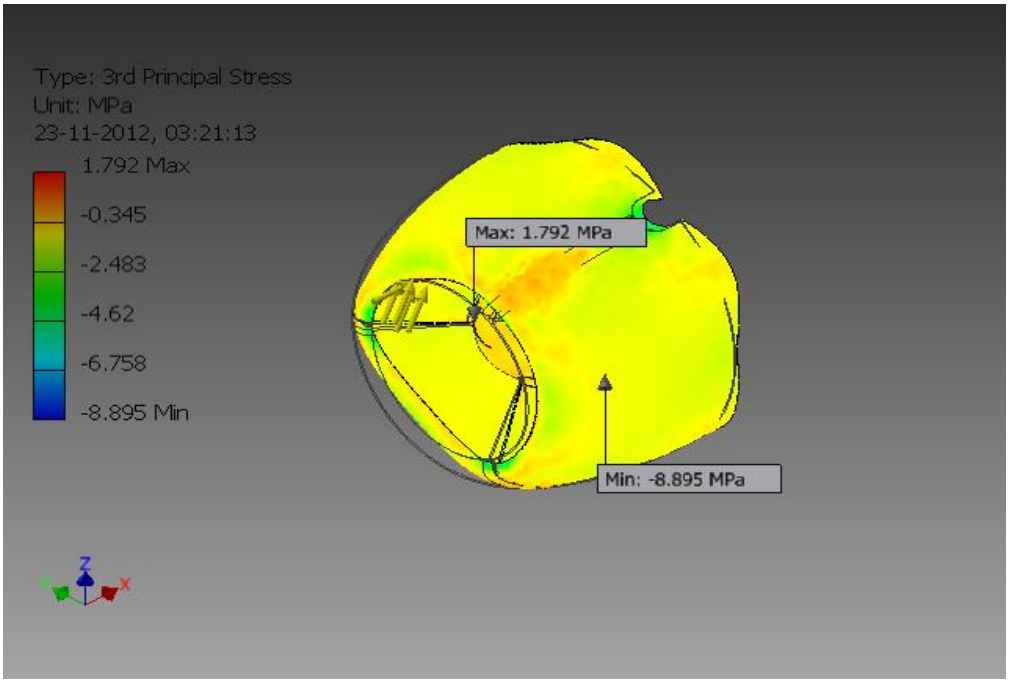

Figure C-0-8 3rd Principal Stress

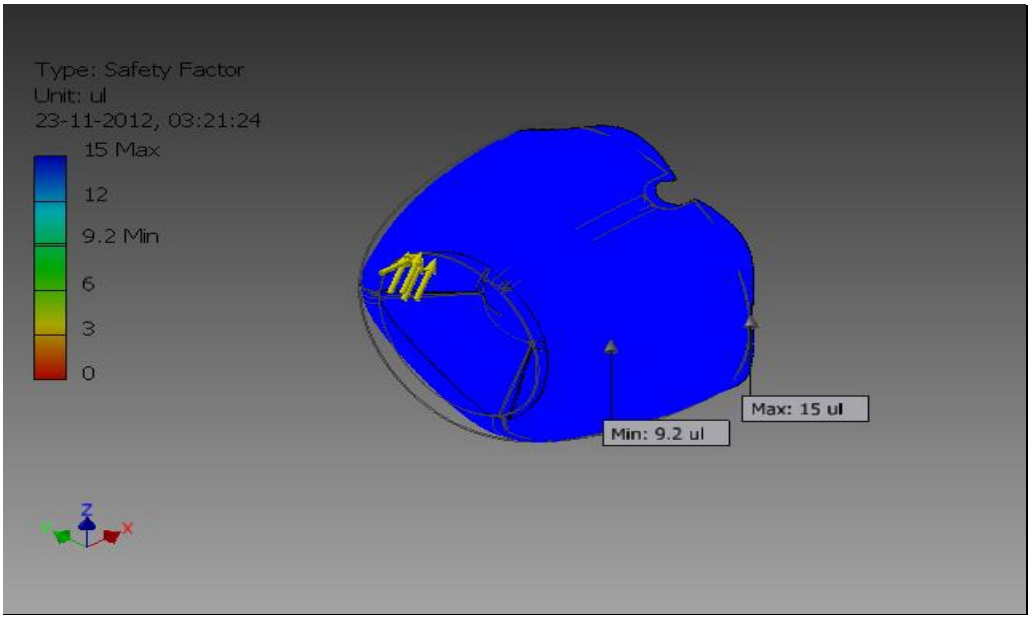

Figure C-0-9 Safety factor

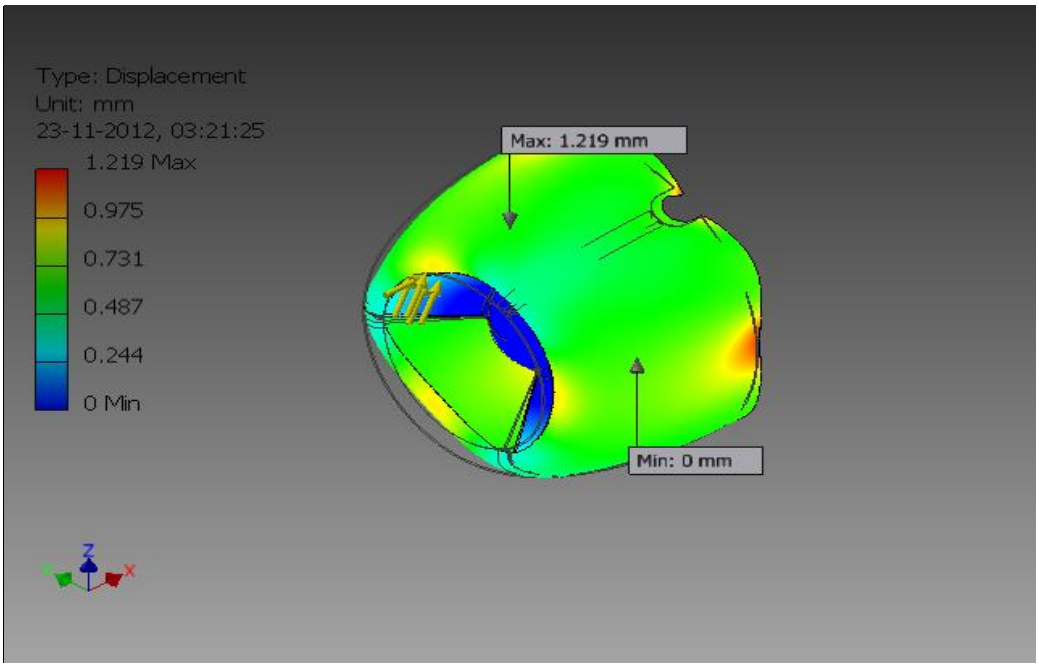

Figure C-0-10 Displacement

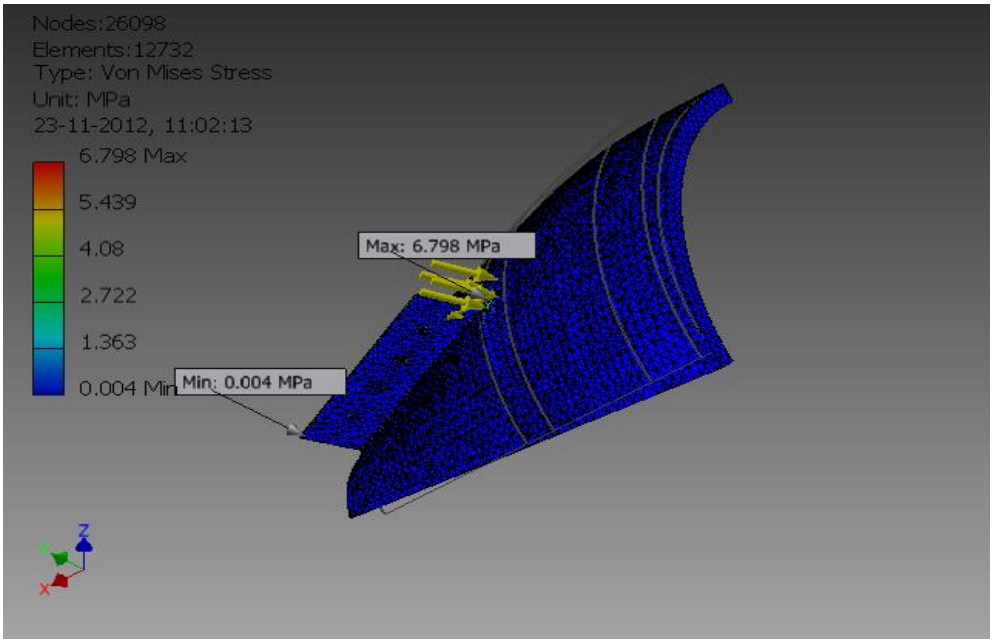

Figure C-0-11 Von Mises Stress lower shroud rear part

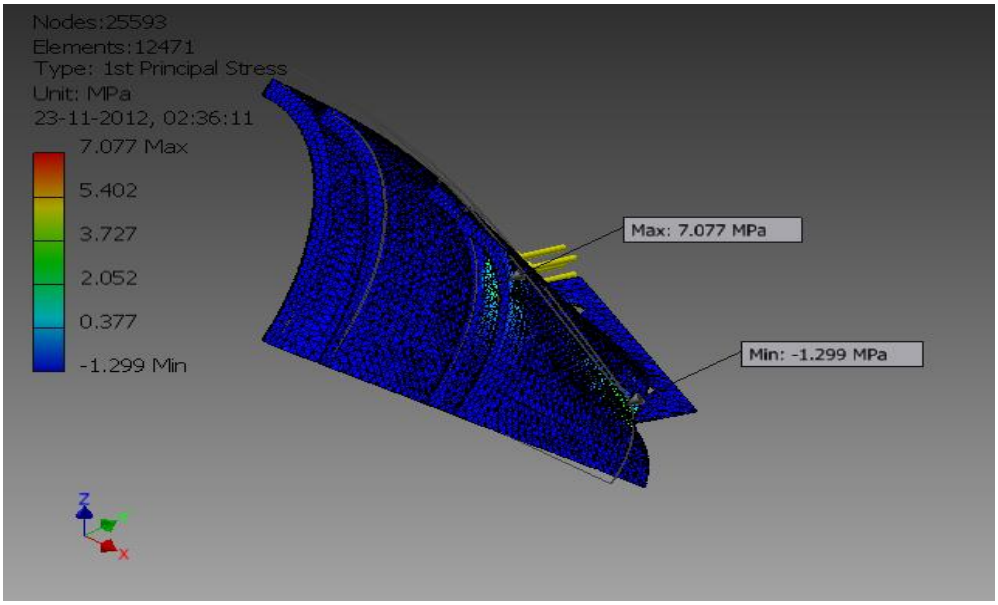

Figure C-0-12 1st Principal stress

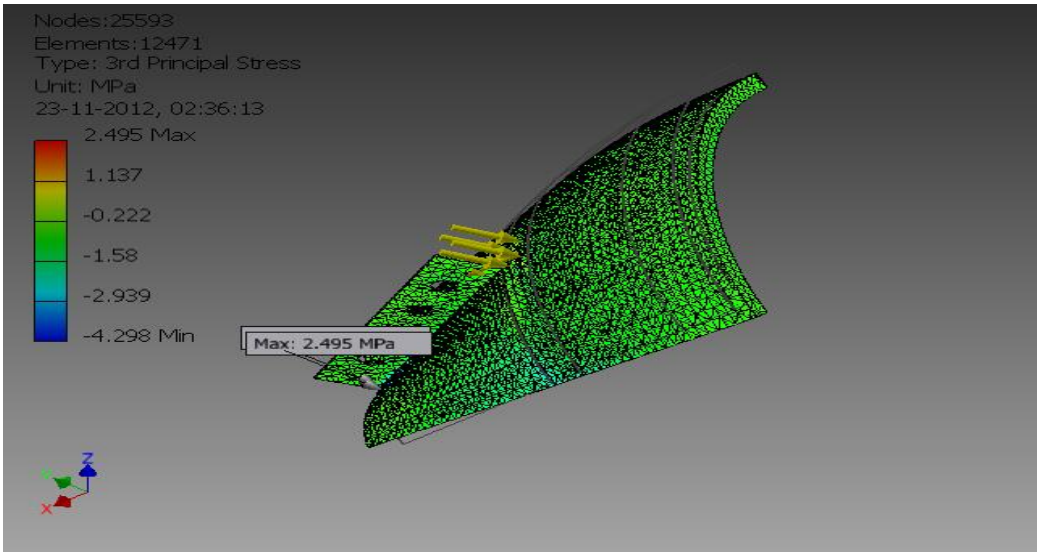

Figure C-0-13 3rd Principal Stress

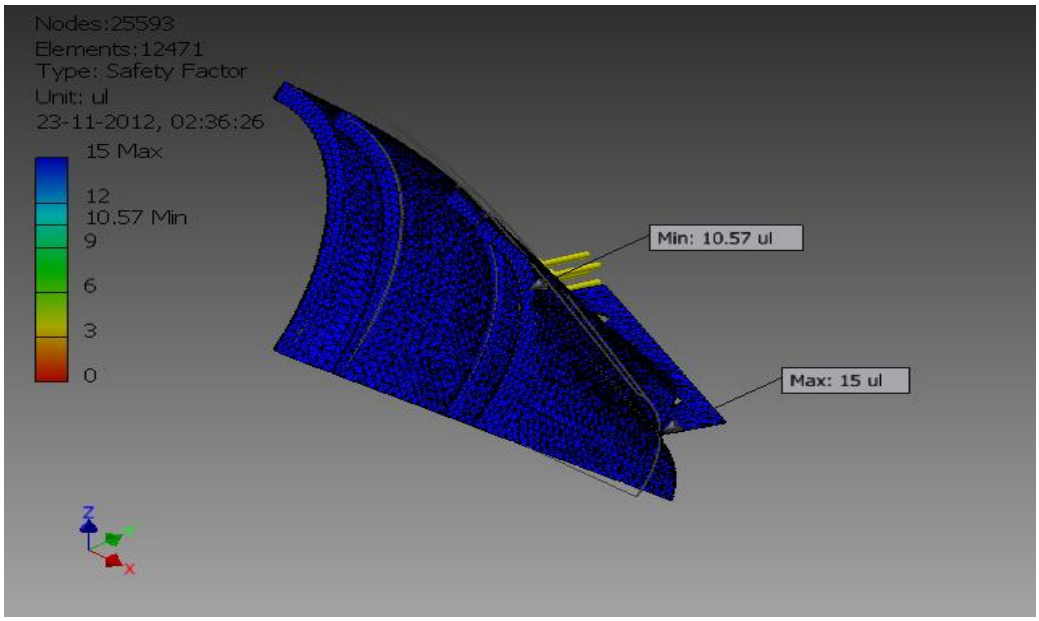

Figure C-0-14 Safety factor

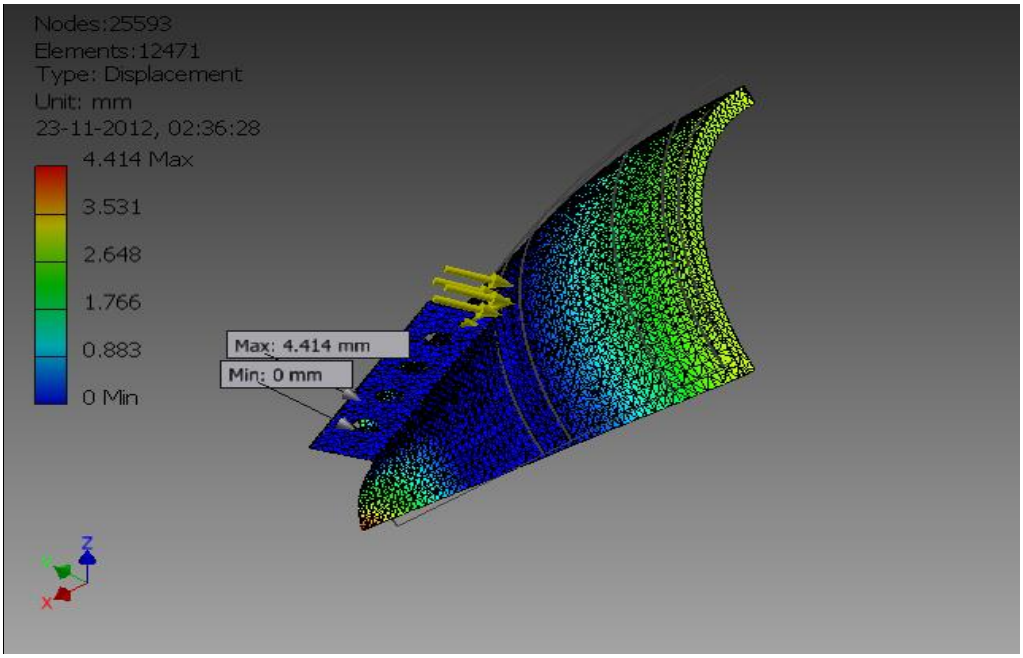

Figure C-0-15 Displacement

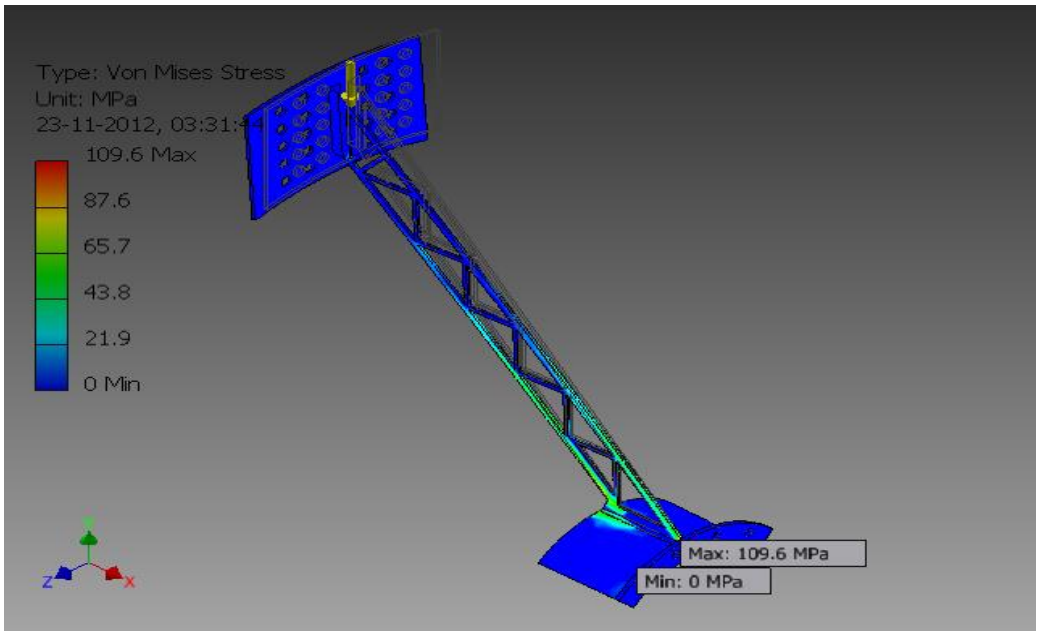

Figure C-0-16 Von Mises Stress

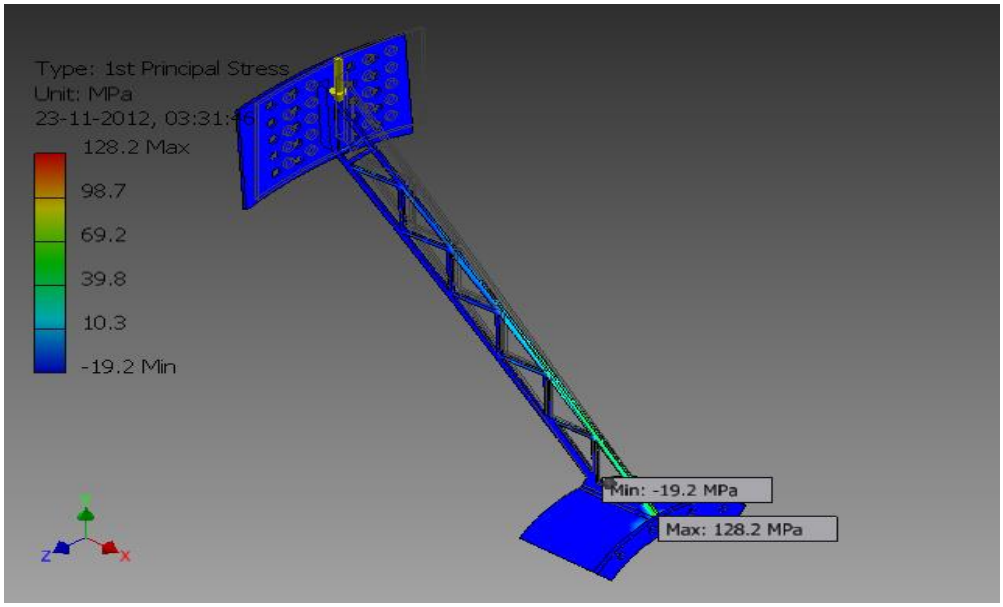

Figure C-0-17 1st Principal stress

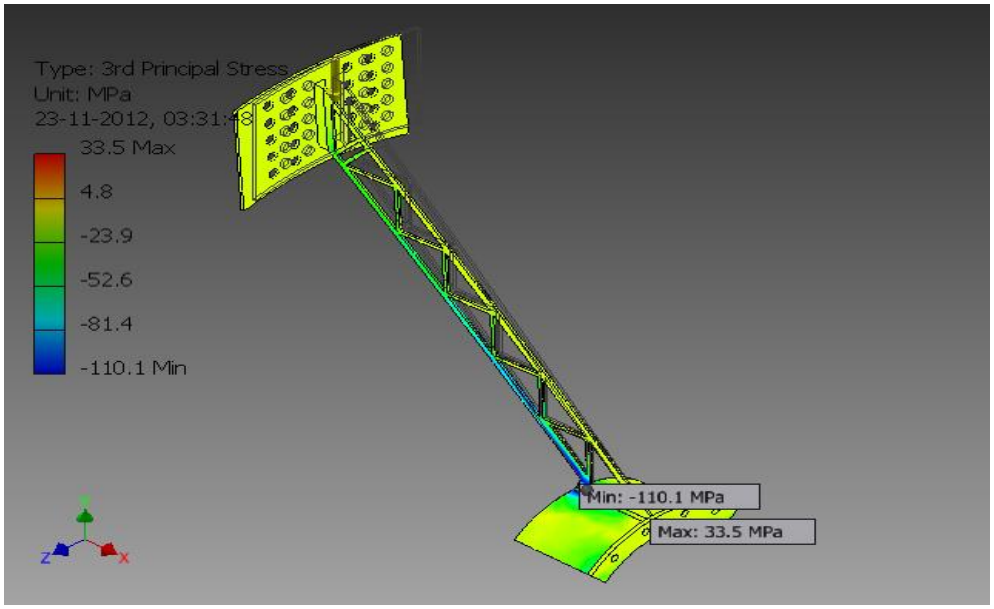

Figure C-0-18 3rd Principal Stress

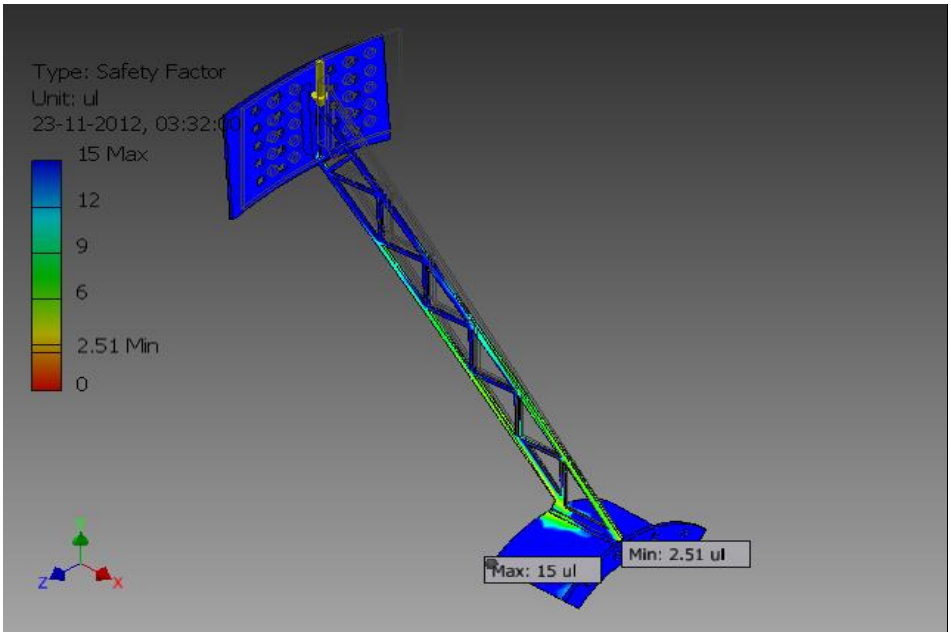

Figure C-0-19 Safety factor

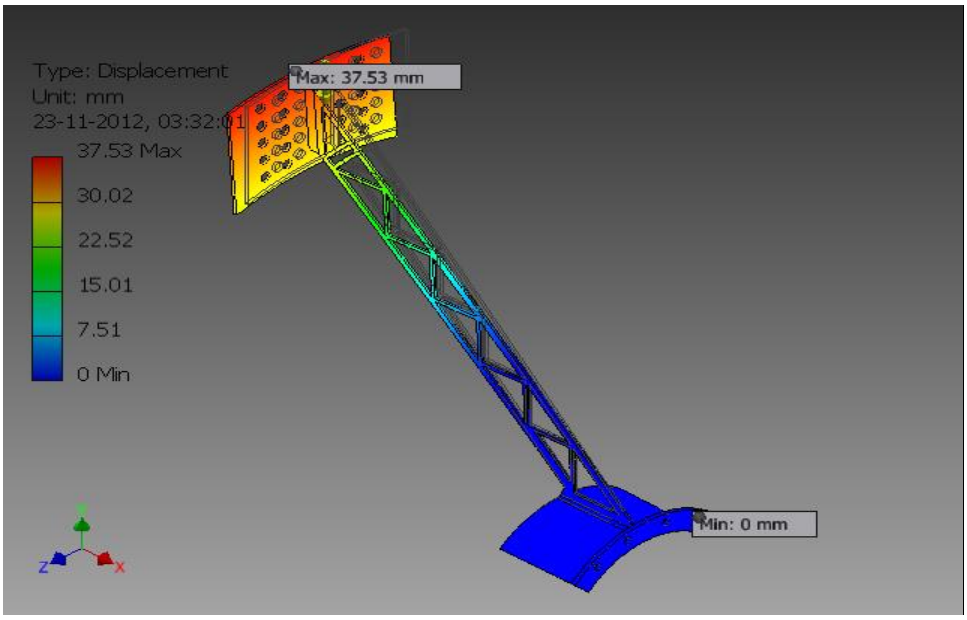

Figure C-0-20 Displacement

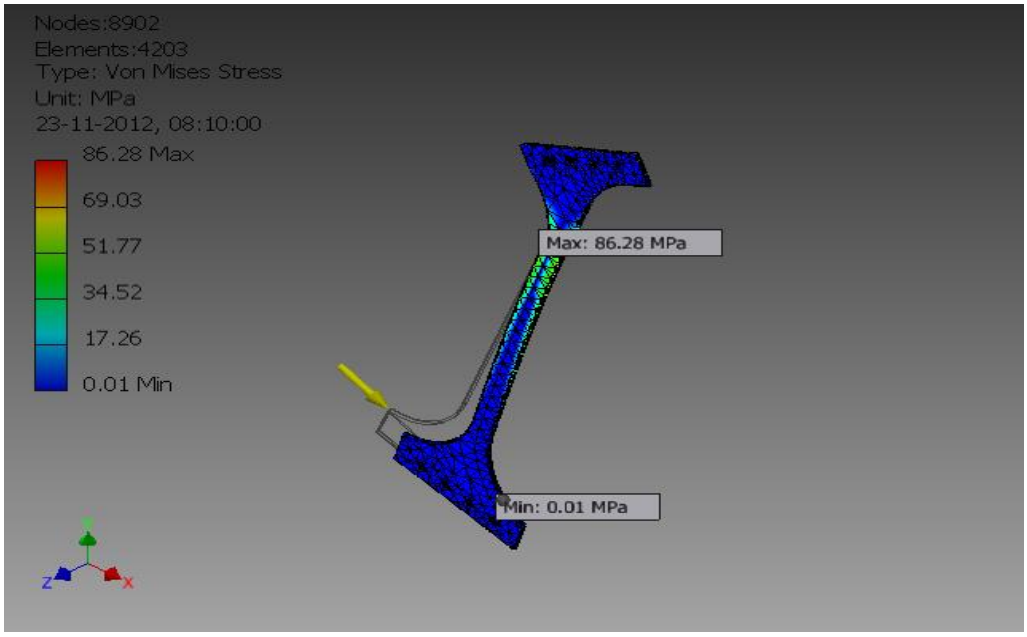

Figure C-0-21 Von Mises Stress inner cross bracing

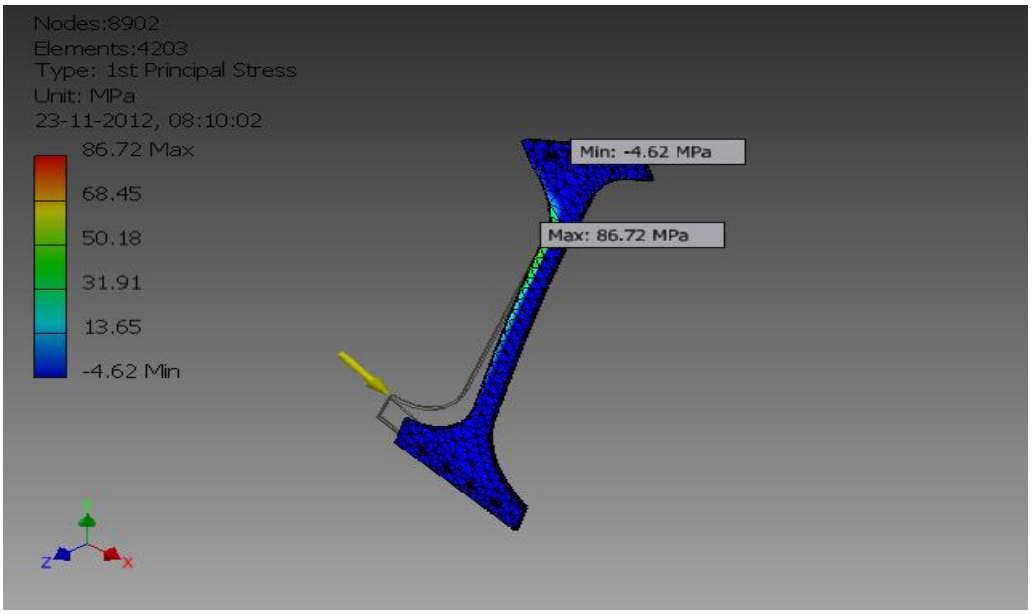

Figure C-0-22 1st Principal stress

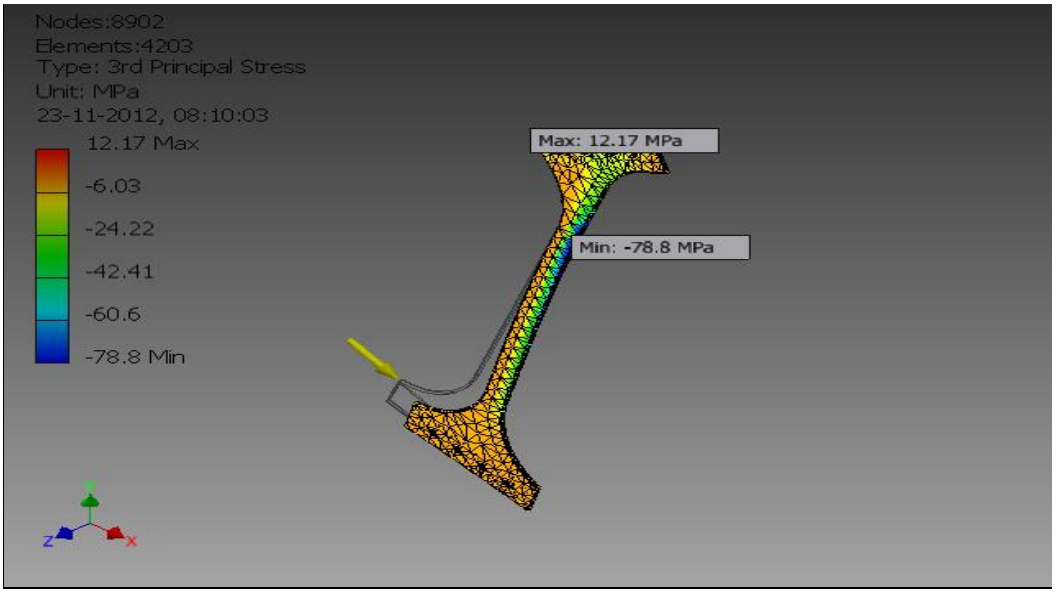

Figure C-0-23 3rd Principal stress

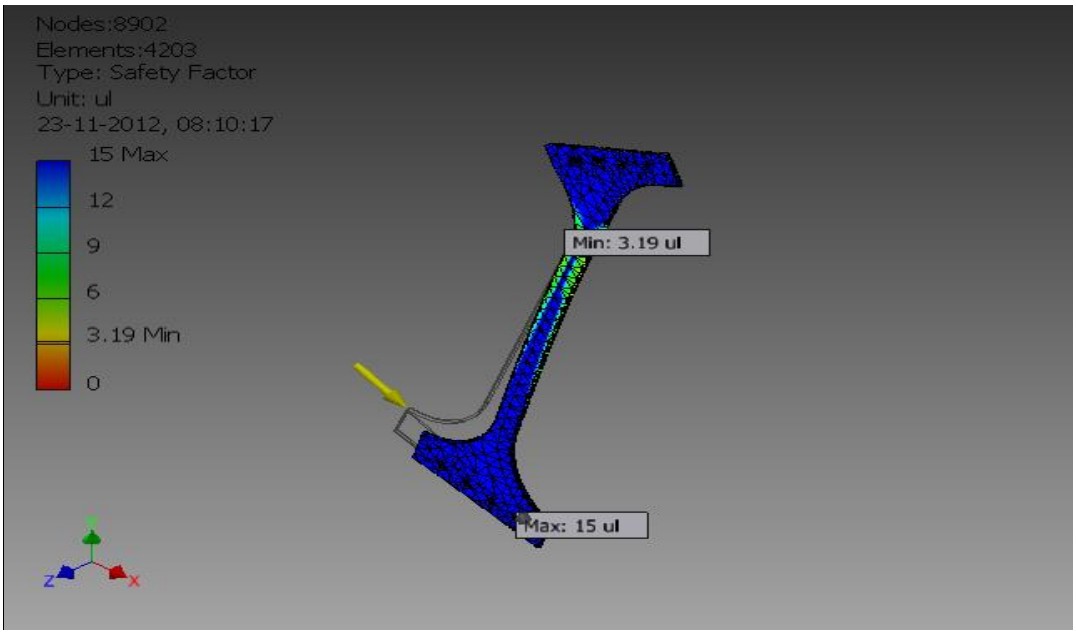

Figure C-0-24 Safety factor

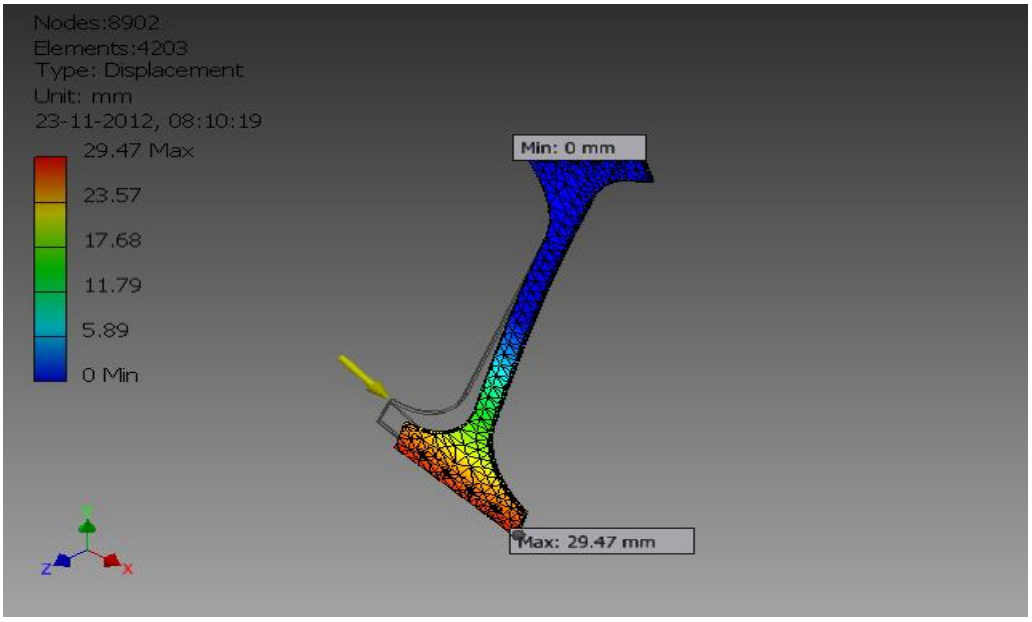

Figure C-0-25 Displacement

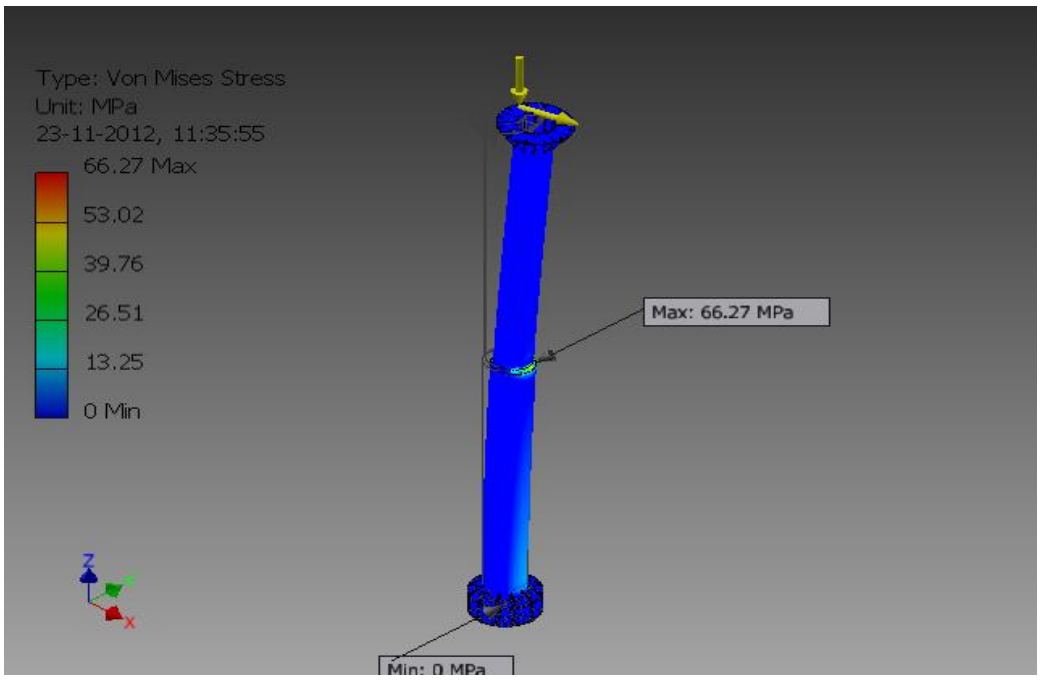

Figure C-0-26 Von Mises Stress for pole

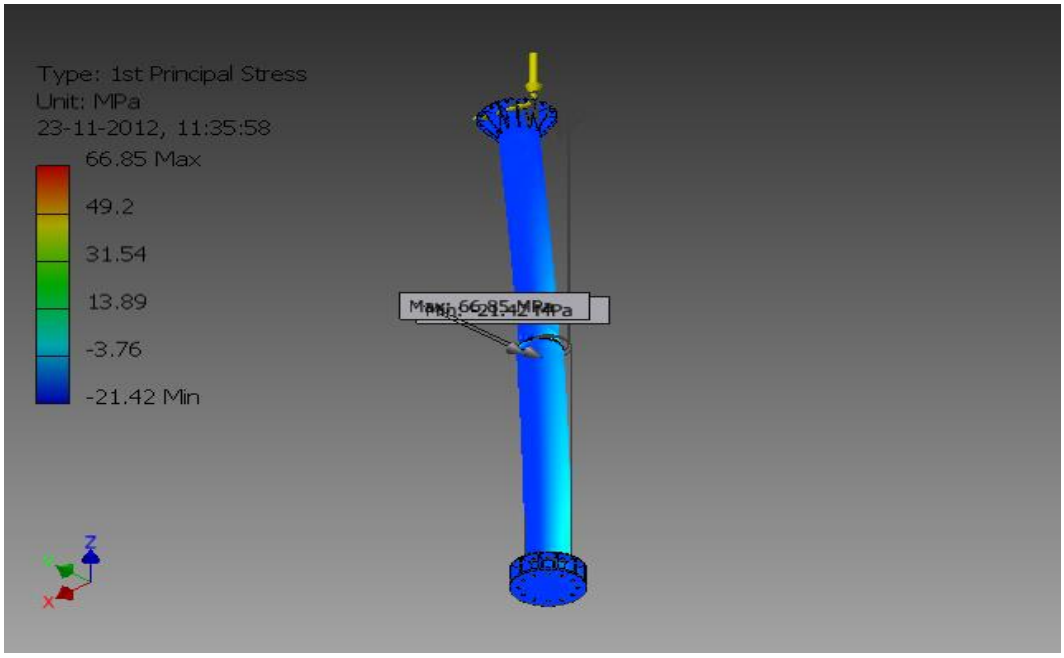

Figure C-0-27 1st Principal stress

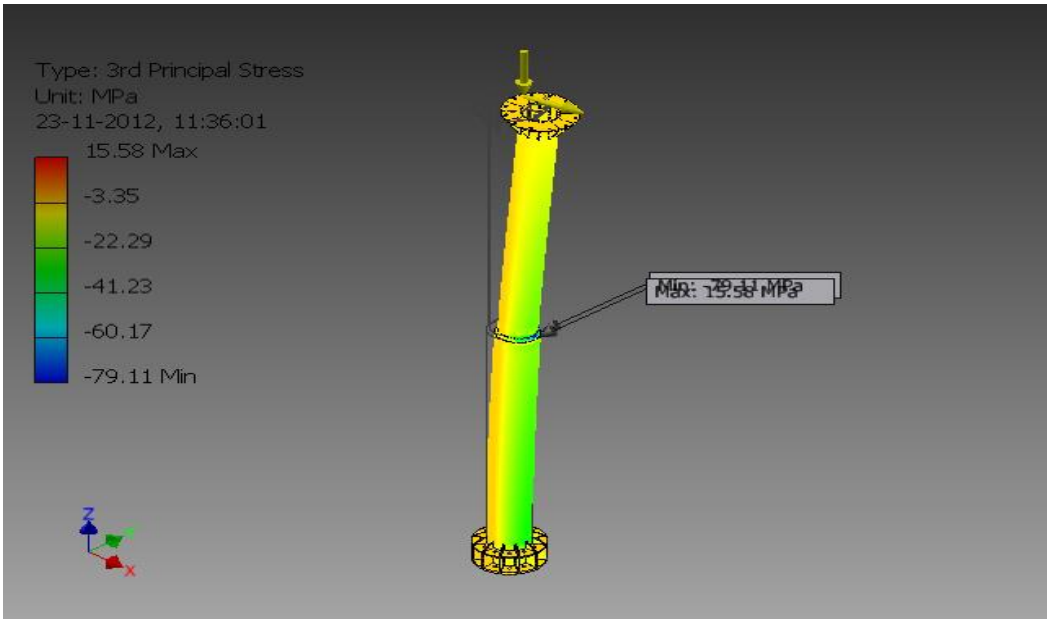

Figure C-0-28 3rd Principal stress

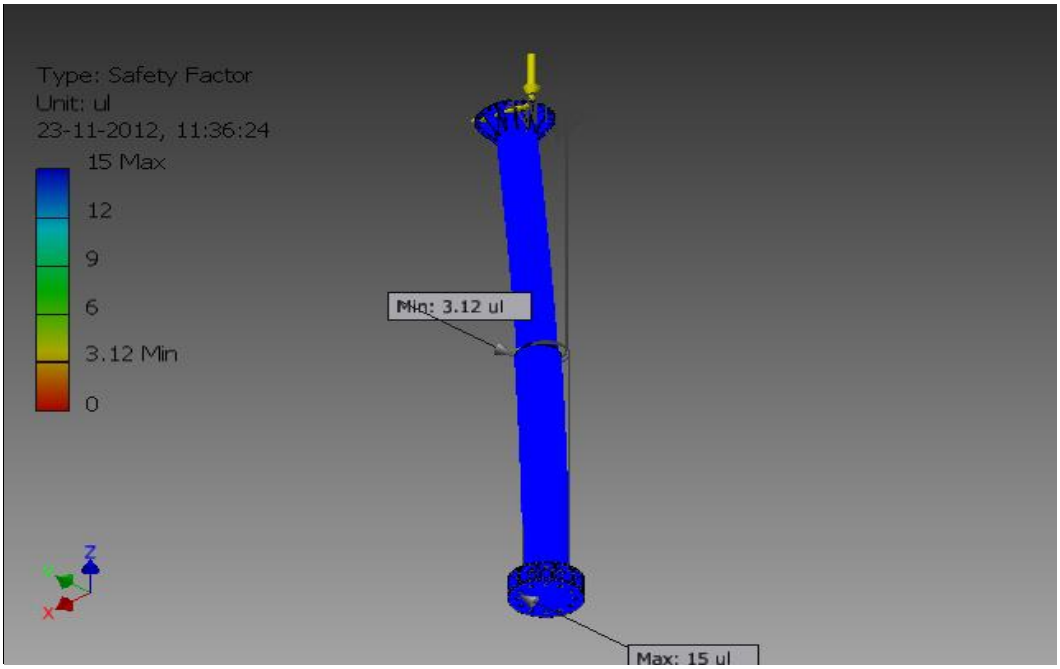

Figure C-0-29 Safety factor

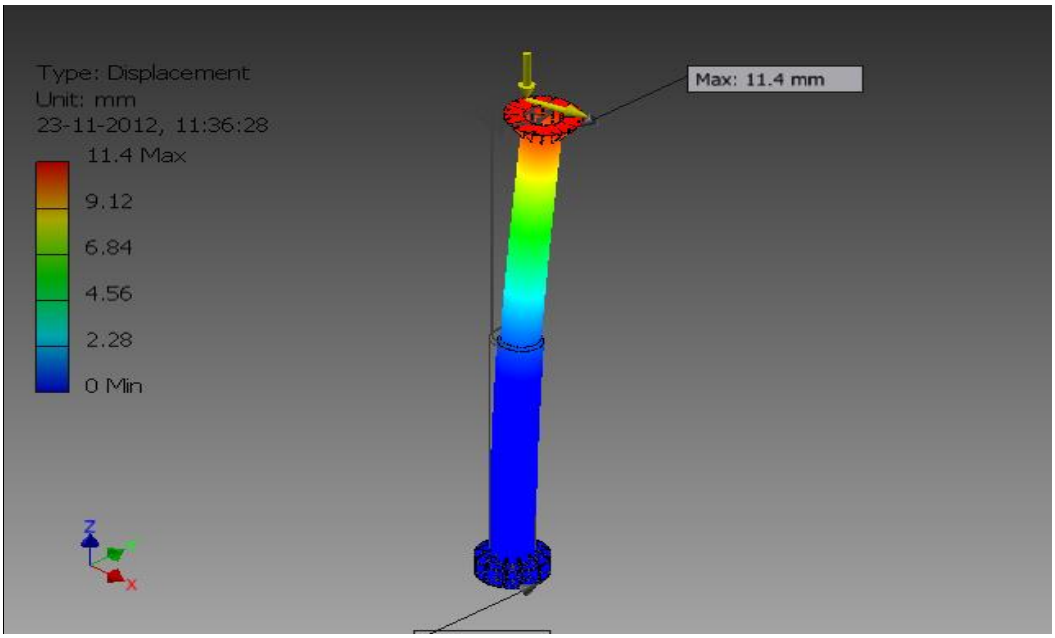

Figure C-0-30 Displacement